

# 3D FE analysis of four legged jack-up vessels during preloading in cohesive soil

Master of Science Thesis

W. Sonnema

Delft University of Technology





# 3D FE analysis of four legged jack-up vessels during preloading in cohesive soil

## Master of Science Thesis

by

W. Sonnema

to obtain the degree of Master of Science  
in Geo-Engineering and Structural Engineering  
at the Delft University of Technology.

Student number: 4239695  
Project duration: September 17, 2018 – July 2, 2019  
Thesis committee: Dr. ir. R. B. J. Brinkgreve, TU Delft (chair)  
Dr. ir. F. Pisanò, TU Delft  
Dr. ir. M. A. N. Hendriks, TU Delft  
Ir. S. Brinkman, Van Oord  
Ir. G. Dantuma, Van Oord



# Abstract

Since the exploitation of wind as a renewable energy resource, jack-up vessels equipped with more than three independent legs are increasingly employed to transport and install the components of offshore wind turbines. By lowering the movable legs the vessel is able to elevate the hull from sea water level. In elevated position the vessel provides a stable platform to perform installation activities. The legs are equipped with spudcans which serve as foundation of the vessel. The elevating process consists of a preload phase to ensure sufficient capacity to withstand operational and possible storm conditions. The preloading of four-legged jack-ups is performed by alternately applying vertical loads on diagonally opposite leg pairs, up to achieving a stable condition in which nearly constant load levels can be held by each leg. The aim of this research is to develop a 3D model to assess the preload duration of the jack-up vessel *Aeolus* in cohesive soil.

The viscous behaviour of cohesive soil, like clay, influence the acting leg load during preload of the jack-up vessel. The shear strength of clay is a function of strain rate meaning that resistance increases due to viscous effects with increasing penetration rate. During spudcan penetration the shearing resistance is high but will reduce significantly when penetration is stopped as the viscoplastic resistance diminishes. Together with the onset of isotach soil behaviour this causes the loads to redistribute between the legs occurs. In this study it is assumed that sufficient preloading is achieved when the leg load reduction is limited to 400 ton / 15 min. To satisfy this criterion multiple load cycles of each leg pair are performed.

Site specific geotechnical data and information on the structural stiffness of the *Aeolus* have been available for this research and allowed for an accurate analysis of the processes during the preload procedure. The Soft Soil Creep (SSC) model is used as constitutive model and accounts for viscous effects by formulating irreversible strains by means of viscoplasticity. The soil at the project site is classified and the constitutive model is calibrated based upon the available soil test results.

The structural behaviour of the vessel is captured via a simplified beam configuration representing the deck structure and legs, the stiffness of the beams is verified using the results from a so-called predrive analysis. The extension of the legs is established by means of negatively pre-stressed node-to-node anchors.

Simulations of a single spudcan penetrating at various depths and penetration rates are performed to identify the extent of viscous strain rate effects from the results. With the developed 3D model Small Deformation Finite Element analyses of the preload procedure are performed. The leg loads and penetrations are monitored and compared to jacking data from the actual project site. The processes in the soil and structure are analysed and the influence on the preload procedure and preload duration is identified. For both type of simulations six different case-calculations are performed addressing variation in the initial spudcan depth, the OCR, the penetration rate, the permeability and the type of preload procedure.

The simulations indicated that the penetration of a spudcan influences the penetration of an adjacent spudcan, this reciprocal influence of the spudcans emphasizes the importance of one model comprising all spudcans in the same 3D soil domain. The developed model slightly overestimates the spudcan penetration and underestimates the total preload duration.

Simulations of the overshooting preload procedure and an alternative preload procedure are performed with the FE model. For the soil conditions used in this research, both the overshooting and the alternative procedure are effective in reducing the number of preload cycles to satisfy the preload criterion. Compared to the normal preload procedure, it is expected the overshooting procedure improves the preload duration. For the alternative procedure however, the duration of a preload cycle increases significantly and consequently the procedure does not improve the preload duration. Using a lower spudcan penetration rate during the normal preload procedure is also effective in reducing the number of preload cycles but significantly increases the elapsed time to complete the preload procedure. The above conclusions have been made on the basis of the model results, which is calibrated for the soil conditions at the specific project site.



# Acknowledgement

This thesis is written as the final work to complete the Master's programme Structural Engineering with the specialisation Structural Mechanics and the Master's programme Geo-Engineering of the faculty of Civil Engineering at Delft University of Technology. The subject for this research was formulated in cooperation with Van Oord.

I was not able to perform and complete the research without the help of others. I would like to thank my graduation committee for their guidance and supervision throughout the research. First, I would like to thank my university daily supervisor Federico Pisanò. After introducing me to the interesting topic regarding soil foundation interaction in jack-up platforms during my Bachelor's thesis, Federico also created the opportunity for this research. His support, feedback and enthusiasm have contributed a great deal to the final work. Second, I want to thank Ronald Brinkgreve and Max Hendriks for their willingness to take a seat in the committee. Their involvement, critical thinking and suggestions throughout the project have been very helpful. Being supervised by numerical-modelling-experts within the disciplines of geo- and structural-engineering, has been a privilege.

I am particularly grateful to Sanne Brinkman and Gerrit Dantuma from Van Oord. To perform this research with and at Van Oord was only possible with their help. They provided me with all necessary means and introduced me to the geo-technical and structural challenges associated with the offshore wind industry. The original and valuable suggestions from Gerrit and the critical and very helpful feedback from Sanne motivated me to work hard.

Finally, I would like to thank my parents and brother for their continuous support and report reviews. Also special thanks to my room-mates, friends, family, sailing team, football team and fellow Van Oord graduates for taking time to discuss about my project and to relax from time to time.

*W. Sonnema  
Delft, July 2019*



# Contents

<b>Abstract</b>	<b>i</b>
<b>Acknowledgement</b>	<b>ii</b>
<b>1 Introduction</b>	<b>1</b>
1.1 Problem definition . . . . .	1
1.2 Research objective . . . . .	4
<b>2 Preload procedure</b>	<b>5</b>
2.1 Spudcan preloading. . . . .	5
2.2 FE model setup . . . . .	8
2.3 Soil classification . . . . .	12
<b>3 Model development</b>	<b>20</b>
3.1 Soil model. . . . .	20
3.2 Structural model . . . . .	26
3.3 FE discretization . . . . .	31
3.4 Total model . . . . .	33
<b>4 Simulations</b>	<b>34</b>
4.1 Method . . . . .	34
4.2 Results . . . . .	36
4.3 Discussion . . . . .	47
<b>5 Conclusion and recommendations</b>	<b>50</b>
5.1 Conclusion . . . . .	50
5.2 Limitations . . . . .	51
5.3 Recommendations . . . . .	52
<b>Bibliography</b>	<b>54</b>
<b>Appendices</b>	<b>58</b>
A Appendix Soil parameters	58
B Appendix FE spudcan shape	62
C Appendix Extension mechanism	63
D Appendix Results predrive analysis - Confidential	64
E Appendix 2D mesh discretization	65
F Appendix Calibration soil model	66
G Appendix Change of permeability	73
H Appendix Alternative FE model	74
I Appendix Jacking data - Confidential	75
J Appendix FE results	76
K Appendix Normalization rules - Confidential	81

# Introduction

## 1.1 Problem definition

Mobile jack-up platforms have been used in the offshore industry for a long time. A jack-up platform used for offshore oil and gas drilling activities is typically equipped with three independent legs (Bienen and Cassidy (2006), Dean (2010), Randolph and Gourvenec (2011)). Since the exploitation of wind as a renewable energy resource, jack-up vessels equipped with more than three independent legs are increasingly employed to transport and install the components of offshore wind turbines. By lowering the movable legs the vessel is able to elevate the hull from sea water level. In elevated position the vessel provides a stable platform to perform installation activities. The legs are equipped with spudcans, which serve as foundation of the vessel. Globaldata (2012) reports the fast growth and the huge growth potential of the offshore wind industry and specialised offshore vessels. The self-installing and elevating capacity of jack-up platforms make them explicitly useful for the installation of offshore wind turbines.

An offshore wind farm consists of many separate wind turbines, which makes the jack-up vessel to conduct elevating and retrieving processes frequently. The elevating process consists of a preload phase to ensure sufficient capacity to withstand operational and possible storm conditions. The preloading of four-legged jack-ups is performed by alternately applying vertical loads on diagonally opposite leg pairs, up to achieving a stable condition in which nearly constant load levels can be held by each leg.

A site-specific assessment of the vessel is performed for each location where the vessel will jack up. The assessment addresses the site specific conditions, including geotechnical and environmental characteristics. In an attempt to standardize the site-specific assessment for a jack-up platform the industry guideline and standards SNAME (2008) and ISO (2016) have been published. The documents provide an assessment of the installation, operation and extraction of the jack-up at a specific location. The study InSafeJIP (2011) indicates the ongoing process of procedural improvements on geotechnical site assessment, ground treatment and foundation performance prediction.

Potential problems during elevation, operation and extraction of the spudcan foundations are identified based on the geotechnical conditions. The soil conditions can be roughly divided in cohesive and non-cohesive. Non-cohesive soil conditions generally form a firm seabed with high bearing capacity where penetration will be minimal. Cohesive soil shows lower bearing capacities leading to larger penetrations of the spudcan and leg. In combination with several other processes this leads to long jacking times. Examples of such processes are the viscous behaviour of the soil and the redistribution of loads between the different legs. The combination of geotechnical and structural aspects affects the total response and preload procedure. This proves the statement of Houlsby (2016), describing the importance of an effective means of communication between the geotechnical and structural engineer in problems of soil structure interaction.



(a)



(b)

Figure 1.1: Van Oord's offshore installation vessel Aeolus in operation (a) and in elevated position (b).

In this research the preload procedure of the offshore installation vessel of Van Oord, *Aeolus*, in cohesive soil is investigated. *Aeolus* is purpose built to transport and install offshore wind turbines and their foundations. The vessel is equipped with four legs with a length of 85 m and a diameter of 4.5 m. The spudcans have an effective diameter of 13 m and should provide a foundation for a total elevated weight up to 28 000 ton.

### Preload procedure

The preload procedure as generally adopted used for the installation of four legged jack-up vessels is based on the principle of load distribution between diagonally opposite leg pairs. The two diagonally opposite leg pairs are loaded alternately. The procedure is the so-called active preload procedure since the legs are preloaded by consecutively extending the legs. As the legs are extended additional penetration is observed.

In figure 1.2 the preload procedure is schematically represented. Before actual preloading starts the four legs are penetrated into the soil under the self weight of the vessel. The blue leg pair in figure 1.2 represents the so-called active leg pair for the first part of the data shown, while in the second part it represents the passive leg pair. The blue leg pair is preloaded first by extending both legs. To ensure stability and safe preload sufficient load on the passive leg pair is maintained by extending the active leg pair in small increments. When the extension of all four legs is kept constant, a decrease in leg load for the active leg pair is observed. This load transfer is partly caused by the viscous behaviour of cohesive soil as described by Cathie et al. (2017) and Fila (2018). The load redistribution between the four legs is occurring simultaneously. As the leg load for the active leg pair decreases, the leg load for the passive leg pair increases. This complex mechanism is not yet considered in the guideline (SNAME, 2008) and standard (ISO, 2016) for the industry. After preloading one leg pair the other leg pair, red pair in figure 1.2, is preloaded according to the same procedure.

Actively increasing the load on the spudcan is required to suffice the preload value on each spudcan. In cohesive soil this process is expected to lead to further settlements and multiple cycles are required. The accumulated effect of these extension (or load) cycles results in a significant increase in total time for wind farm installation.

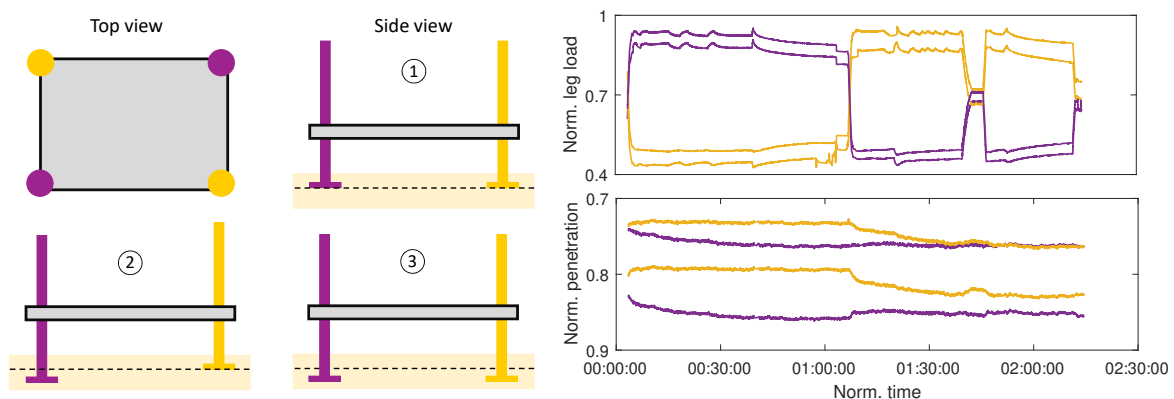


Figure 1.2: Schematic representation of the active preload procedure.

The viscous behaviour of cohesive soil, like clay, influence the acting leg load during preload of the jack-up vessel. The shear strength of clay is a function of strain rate meaning that resistance increases due to viscous effects with increasing penetration rate. The viscous effect is most evident for undrained conditions because of the high strain rates in the soil (Lee and Randolph, 2011). During spudcan penetration the shearing resistance is high but will reduce significantly when penetration is stopped, the viscoplastic resistance diminishes and a load redistribution between the legs occurs. This reduction will result in a leg load well below the preload value as determined in the site specific assessment. To suffice this preload value multiple load cycles of the active leg pair are required.

A preload criterion to ensure safe leg load reduction is used in practice. In this study a maximum leg load reduction of 400 ton / 15 min is used as criterion. Papers only present indistinct guidelines rather than practical criteria to account for the additional penetrations in which preload holding times to account for consolidation are advised, based upon the permeability factor and stiffness modulus. However, only consolidation and no viscous effect seems to be incorporated.

The load redistribution from the active leg pair to the passive leg pair during preload of the jack-up vessel is a complex mechanism occurring simultaneous to the viscous effects. The load working on the active leg pair fully mobilises the shear strength of clay since the spudcan proceeds to penetrate. Since relaxation and creep

rate are dependent on the distance from the failure surface, a higher load results in a higher creep strain rate (isotach behaviour). This phenomenon results in rapid relaxation for the active leg pair. On the contrary, the passive leg pair is exposed to significant lower loads resulting in a lower relaxation rate. This establishes the process of load redistribution and a load transfer from the active to the passive leg pair is observed.

Both mechanisms, viscous effects and load redistribution, substantially influence the final penetration and total jacking time. A three-dimensional numerical model capable of capturing relevant soil processes and soil-structure interaction allows to analyse the influence of both mechanisms on the preload procedure.

A comprehensive 3D model of the soil, the structure and the interaction of both is essential for an accurate analysis. The constitutive model enables the inclusion of essential soil processes taking place during and directly after preload. At the offshore wind site mainly soft clay material is found and is expected to govern the soil behaviour. The numerical models on spudcan penetration and preloading as presented by Fila (2018) showed to be capable of capturing viscous effects rather well, taking into account the influence of stress relaxation on the observed leg load. Fila (2018) used the 2D FE software PLAXIS (Brinkgreve et al., 2018c) in combination with the Soft Soil Creep (SSC) model, this model accounts for viscous effects by formulating irreversible strains by means of viscoplasticity. In the same spirit a 3D finite element vessel model is intended to be developed in this research. Inclusion of the structural configuration of the vessel enables to accurately capture the complex load redistribution mechanism. The 3D FE model is created using the software package PLAXIS 3D (Brinkgreve et al., 2018a).

With this type of software Small Deformation Finite Element (SDFE) analyses are performed. In the SDFE analysis changes in geometry are assumed small after displacement or loading, consequently the geometry is not updated. The penetration of the spudcan up till the moment preloading starts, is chosen to be an input value.

### Project site

The project site considered for this research is located in the Belgian sector of the North Sea. At this location shallow clay of the Ursel formation, being a member of the Maldegem Formation, is found. The marine clay, present up to a depth of 22.7 m, leads to relatively large penetrations and long preload time. Below the clay layer a deep sand layer is found.

Data of the preload procedure of Aeolus is available, the data includes the effective leg loads and spudcan penetrations for a time period of three hours. In figure 1.3 respectively the loads and leg penetrations into the soil over time are illustrated. The total water depth at the site is 40 m on average and the leg loads represent the force at the spudcan tip level.

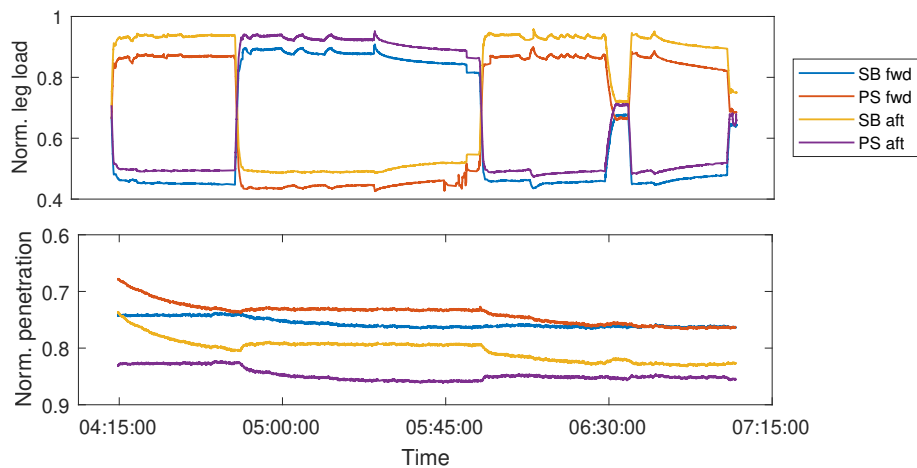


Figure 1.3: Part of the preload procedure of Aeolus at the project site indicating the leg loads and spudcan penetrations.

During the time interval 04:15:00 - 04:45:00 the PS fwd (port side forward) leg and the SB aft (starboard side aft) leg are loaded by extending both legs. During extension of the active leg pair, the load on these two legs increases and is considerably higher than the load on the two other legs. The active legs penetrate approximately 0.5 m further into the soil while the penetration of the passive legs remains constant. During the next time interval (04:45:00 - 06:00:00) the SB fwd and PS aft leg are preloaded.

During the preload time intervals the legs are extended several times, indicated by the small and steep peaks in the graphs in figure 1.3. After these peaks the leg extension is kept constant for all four legs, the legs however

continue to penetrate and the loads of the active legs reduce. The decrease in load for the active legs is caused by the viscous behaviour of the cohesive soil and the load redistribution between the two leg pairs.

## 1.2 Research objective

The offshore installation vessel of Van Oord is purpose-built to construct offshore wind parks. The vessel is equipped with four movable legs including spudcan which allow the hull to be jacked up. When operating in cohesive soil large penetration depths of the legs and spudcans are expected, caused by low bearing capacity and viscous effects. The time to reach sufficient penetration depth is long and difficult to predict in cohesive soil.

The spudcans are preloaded to ensure sufficient bearing capacity during operation. During the preload procedure leg load redistribution between the four legs occurs and is influenced by characteristics of the cohesive soil and the structure connecting the legs. To accurately predict the time required for the preload procedure a better understanding of the load redistribution between the four legs is of importance. An accurate prediction of the preload duration of Aeolus enables Van Oord to identify the total project time and costs already at the tender phase.

The main objective of this research is formulated as:

### **Develop a 3D model to assess the preload duration of the jack-up vessel Aeolus in cohesive soil.**

This main objective is broken down in several sub-objectives:

- Represent the soil conditions and behaviour in a 3D FE model using the software PLAXIS 3D:
  - Thorough classification of the (cohesive) soil at the project site;
  - Selection of a soil constitutive model capable of representing the cohesive soil;
  - Calibration of the constitutive soil model and its parameters to accurately represent the soil conditions at site.
- Capture the structural behaviour of Aeolus in a 3D FE model:
  - Implementation of the structural components of the jack-up vessel structure and verification of the structural behaviour;
  - Implementation of the constitutive soil model and investigation on the use of interfaces for accurate representation of the soil-structure interaction.
- Simulate the preload procedure by combining the structural and soil components:
  - Verification of the 3D FE model;
  - Definition of the simulations to be performed;
  - Execution of the simulations and comparison of the results to the measured jacking data.
- Analyse the leg load redistribution during the preload procedure:
  - Analysis of the processes in the soil and the structure;
  - Investigation on the influence of the structural and soil behaviour on the preload procedure and total duration;
  - Identification and simulation of different preload procedures and comparison of the results.

## Preload procedure

A vital part of the 3D finite element model is the constitutive soil model. In the following section the processes in the soil and the structure during preloading are elaborated and based on this analysis the type of constitutive model is chosen. The choice of the type of soil model determines how soil-structure interaction and load redistribution between the legs are incorporated in the model.

In the final section the soil is classified and its characteristics are identified. The soil parameters are determined from the available soil tests to identify to which extent this soil type is sensitive to consolidation and viscous effects. As described by Cathie et al. (2017) and Hossain and Randolph (2009b) viscous effects are considered to influence the preload procedure to a large extent in, undrained, cohesive soils. Both processes are not enclosed in the industry's guidelines SNAME (2008) and Veritas (2015). The ISO standard (ISO, 2016) recognises the viscous effects and potential soil consolidation, however none of the effects are taken into account.

### 2.1 Spudcan preloading

During spudcan preloading in clay three processes are to be considered: the viscous drag of the leg and spudcan, consolidation and the viscous behaviour. These processes affect the preload criterion, which defines the requirements to ensure safe leg load during operation. This criterion determines the final spudcan depth and preload duration, depending on the soil parameters.

#### Soil processes

Currently the spudcan penetration depth is generally assessed by determining the soil bearing capacity profile. This profile is obtained from a series of 'wished in place' spudcans at increasing depths. The industry's guideline (SNAME, 2008) and standard (ISO, 2016) advice on the type of bearing capacity calculations. The required bearing capacity equals the desired preload reaction force. For penetration in clays the formula proposed in ISO (2016) is used to calculate the gross ultimate vertical bearing capacity:

$$Q_V = (s_u N_c s_c d_c + p'_o) \pi B^2 / 4 \quad (2.1)$$

The factor  $p'_o$  is the effective overburden pressure at depth  $D$  and  $d_c$  is the bearing capacity depth factor ( $d_c = 1 + 0.2(D/B) \leq 1.5$ ). The undrained shear strength,  $s_u$ , should be based on the sampling method, laboratory test type and field experience (ISO, 2016).  $B$  is the effective spudcan diameter and  $s_c$  is the shape factor.  $N_c$  is the bearing capacity factor and is determined by methods described by Skempton (1951), Houlsby and Martin (2003) and Hossain et al. (2006). The method proposed by Skempton (1951) provides a reasonable prediction of average penetrations. The methods proposed by Houlsby and Martin (2003) and Hossain et al. (2006) provide a lower bound and upper bound load-penetration prediction respectively. The viscous effects of clay are not taken into account.

Cohesive soil exhibits viscous strain rate dependency, which means that the shear strength of these soils is affected by the magnitude of the shear strain rate. These viscous strain rate effects affect the leg settlements during the preload holding. The viscous behaviour results in higher penetration resistance for larger spudcan penetration rates.

Richardson and Whitman (1963) investigated the effect of strain-rate on the undrained shear resistance in normally consolidated clay. At small strains the ratio  $\sigma'_1/\sigma'_3$  increases and an increase in resistance to soil distortion is observed. At large strains a different phenomenon is observed as the adjacent soil particles find it more difficult to move and will tend to ride up over one another. It can be considered as an increased resistance to compression or an increased tendency to dilate. Increasing the strain rate results in a decrease in pore pressures and consequently larger effective stresses.

During spudcan penetration in cohesive soil the resistance increases due to the viscous drag of the leg and spudcan. As penetration proceeds the soil is extensively disturbed around the spudcan and embedded leg part. Zeevaart (1948) divides the disturbed soil in three zones, varying in level of disturbance in the soil. Zone

I represents soil subjected to excessive remoulding, the soil reaches a critical state leading to continuous deformation. Zone II is surrounding Zone I and represents the soil only disturbed as the shaft tip of the shaft is positioned adjacent to it. The soil in zone III is unaffected and remains undisturbed. Depending on the soil characteristics, zone III starts approximately three times the shaft radius from the structure surface in case of a straight shaft.

The viscous resistance component depends on the size of zone I, the viscosity of the soil and the velocity of the shaft (Mahajan and Budhu, 2006). As the shaft proceeds to penetrate into the soil, soil is moving downwards in the near field of the shaft and moving upwards in the far field. The velocity gradient at the interface of the soil fields is defined by the size of zone 1 and the penetration rate. The rate of change of velocity gradient at the interface decreases for an increasing size of zone I and a decreasing penetration rate. Figure 2.1 depicts the experimentally derived backbone curve for of the normalized velocity and the normalized vertical soil capacity. The normalized velocity is defined as the ratio of the time for a certain fraction of diameter penetration to occur to the time for a certain fraction of consolidation to occur.

In (partially) drained conditions consolidation dominates over the viscous effects (Lehane et al., 2009). Loading the spudcan results in a significant increase in vertical stress for the soil. Consolidation of the soil around and below the spudcan occurs as the excess pore pressures continue to dissipate. The effective stresses start to increase and an increment in the strength and stiffness of the soil is observed.

At fully undrained conditions, the right side in figure 2.1, the bearing capacity increases by the introduction of viscous effects. Depending on the value for the coefficient of consolidation for the soil the extent of both consolidation and viscous effects can be evaluated using this graph. As the project site for this specific research comprises of a thick cohesive soil layer it is expected the normalized velocity is higher than 10. The soil is allocated to the right side of this graph representing the domain where viscous effects dominate.

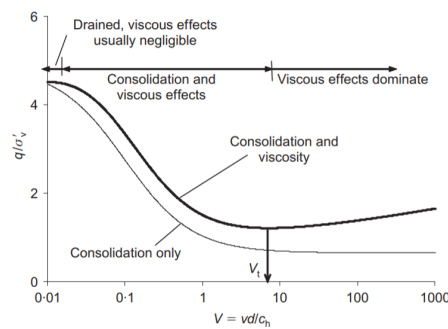


Figure 2.1: Change in vertical soil capacity as function of normalized velocity (Randolph and Gourvenec, 2011) .

Two other processes induced by the viscous behaviour of cohesive soils are creep and stress relaxation. Creep is associated with the deformations occurring over time when the soil is subjected to a constant load. Stress relaxation corresponds to a decrease in stress in response to a constant strain level. Together with the strain rate the three processes lead to the isotach behaviour of cohesive soil. The isotach behaviour holds a relation between  $\epsilon$ ,  $\dot{\epsilon}$  and  $\dot{\sigma}_z$  as depicted in figure 2.2a.

Since relaxation and creep rate are dependent on the distance from the failure surface, a higher load results in a higher creep strain rate (isotach behaviour). The soil shear strength at the active leg pair is fully mobilized as the spudcans proceed to penetrate and rapid stress relaxation is observed. On the contrary, the passive leg pair is exposed to significant lower loads resulting in a lower relaxation rate. This establishes the process of load redistribution and a load transfer from the active to the passive leg pair is occurring.

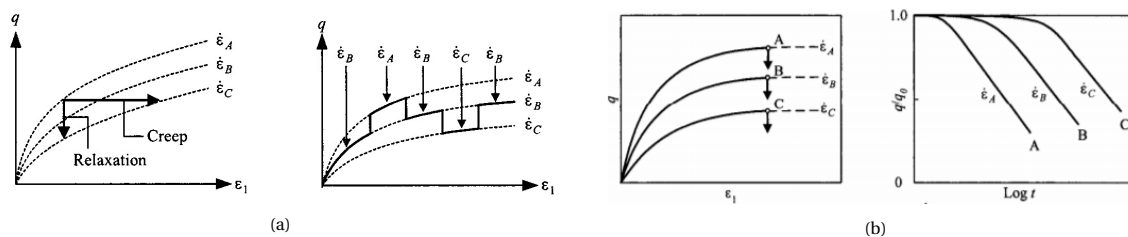


Figure 2.2: (a) Isotach behaviour for clay for creep and relaxation and (b) Stress relaxation for various strain rates (Augustesen et al., 2004).

During the preload procedure one-way cyclic loading is applied on the spudcans. As described by Cathie et al. (2017) this cyclic loading may play a role in the soil behaviour by potentially degrading the soil strength. Cyclic loading of clay, assuming undrained conditions, causes pore pressure build-up. The pore pressure build-up obviously results in a decrease of the effective stress. The cyclic loading potentially causes stiffness and strength degradation of the soil, resulting in hysteretic behaviour. It is expected that this process contributes to the cyclic ratcheting behaviour (accumulating plastic deformations), however its effects may be outweighed by the regain in soil strength due to remoulding of the soil (Cathie et al., 2017).

### Preload criterion

The procedure for jack-up preloading is correlated to (1) a minimum capacity load, (2) a maximum leg penetration per time period and (3) a minimum required height during operation. Point (2) is related to the preload criterion which is used in practice to ensure safe leg load. In this study a maximum leg load reduction of 400 ton / 15 min is used as criterion. This criterion is based upon practical experiences and not substantiated in any guideline, standard or document. Only indistinct guidelines are provided in several documents, as itemized below.

- le Tirant (1993) mainly associates the preload holding time with the degree of consolidation. A correlation between the degree of consolidation and coefficient of permeability allowed to establish an approach for the holding time. A distinction is made between sand and clay layers and a table is presented showing preload holding times for different values for the permeability factor and stiffness modulus. It is noted this is just a first approximation and the times presented in this study could be significant shorter and longer.
- Hedrick and Verret (2007) advice on the jacking procedure in the Gulf of Mexico based upon experiences in the hurricane season. Stating that the consolidation should be fulfilled and the spudcan penetration is ceased.
- Menzies and Roper (2008) compare measured spudcan penetration records. Recommendation resulting from the study is that spudcan penetration should be continuously monitored while holding the maximum preload until additional penetrations become negligible.
- In the introduction paper of InSafeJIP (InSafeJIP, 2011) Osborne et al. (2009) advice on the following items for jack-up preloading: (1) Length of preload holding time and (2) acceptable settlement rate under full preload.
  - (1) In order to provide guidance on this aspect of the installation procedure, the purpose of holding the preload has to be formulated. It is currently unclear whether the foundation is preloaded (a) to prove the soil's bearing capacity is sufficient to withstand the maximum loads anticipated in a storm event, (b) to wait for additional settlement under this load magnitude to decrease to an acceptable level or (c) to induce a degree of consolidation in the underlying soil. The required length of preload holding time will vary significantly depending on its purpose as well as the soil strength.
  - (2) This item is closely linked to the previous as the acceptable rate will depend on the purpose of preload holding. The cause for continued settlement under preload (consolidation, creep) will need to be established before acceptable rates can be recommended.
- In InSafeJIP (2011) recommendations, which apply to all preloading strategies, are described. These recommendations are that the preload should be held until leg settlements have ceased or have decreased to an acceptable rate and no further backflow is expected. No further specification is provided for this 'acceptable rate'.
- Bienen and Cassidy (2013), Luking et al. (2014) and Stanier et al. (2014) state that an important factor during preloading is the consolidation and investigate the effect on soil capacity by varying consolidation time and penetration depth.
- Cathie et al. (2017) analyse the standard preloading procedure for a four legged jack-up structure. The iterative preloading procedure leads to further penetration and long jacking times. As causes for this phenomenon are mentioned the viscous and rate-dependent properties of the clay. A new jacking procedure, the overshooting jacking procedure, is proposed in the paper.
- Fila (2018) states that the pore water pressure generation is crucial for determining the required preload time, since the rate of pore pressure dissipation during consolidation is related to the preload requirement over time. Due to the short jack-up duration of maximum 1 day, in the offshore wind industry, the effect of water dissipation and effective strength increase is negligible.

## 2.2 FE model setup

The Finite Element Method (FEM) is used to analyse the preload procedure. The application, the benefits and the limitations of the type of analysis are elaborated in the following section. The choice for the type of constitutive soil model is made and mathematical information on the model is provided.

### 2.2.1 FE analysis

The interaction between soil and spudcan highly affects the response of the jack-up vessel during preloading. Multiple researches have been conducted for soil-structure interaction of spudcans at final position after installation and preloading (Cassidy et al. (2004a), Bienen and Cassidy (2006), Cassidy et al. (2004b), Cassidy et al. (2002), Bienen and Cassidy (2006), Bienen and Cassidy (2009), Vlahos et al. (2011), Zhang et al. (2014), Cassidy et al. (2010), Dean et al. (1997), Dean and Metters (2009), Cassidy (2011)). Modelling the interaction during the preloading however is not considered accurately as in most of these researches the force-resultant model is adopted. A macroelement of the spudcan and adjacent soil (Martin (1994), Thompson (1996)) is incorporated into jack-up structural analyses and the soil body is not represented by continuum elements.

The jack-up is a flexible structure and spudcan penetrations are large. The soil behaviour during installation and preloading is best captured using large deformation finite element (LDFE) analyses in which the changing geometry is updated. By the use of this type of analyses the large strains and displacements, associated with continuous penetration of the spudcan from the soil surface to final position, are captured. This is shown by Pisanò et al. (2019) where a symmetrical lateral pushover analysis is performed. The LDFE is found to be more accurate than the Small Deformation Finite Element (SDFE) prediction.

Two examples of large deformation FE methods are the Remeshing and Interpolation Technique by Small Strain (RITSS) developed by the University of Western Australia (Hu and Randolph, 1998) and the Coupled Eulerian-Lagrangian (CEL) available in some commercial software. Investigation of the penetration of spudcan foundations is performed with the RITSS approach (Hossain et al. (2005), Hossain and Randolph (2010), Yu et al. (2012)) and the CEL method (Qiu and Grabe (2012), Tho et al. (2012b), Tho et al. (2012a), Pucker et al. (2013)).

Another example of a large deformation method is the Material Point Method (MPM) which is a mesh-less method. The material is discretized into material points which are assigned with properties. A background computational grid solves the equations of motions for gradient terms (for example displacement). The information for each material point is updated using the solutions of the background grid. Since the information on the state of calculation in the MPM is stored in particles, no re-meshing and re-mapping is required. This prevents the introduction of additional errors during transformation of the distorted mesh to the updated mesh. According Brinkgreve et al. (2017) the use of MPM analyses is particularly adequate for spudcan penetration.

The large deformation numerical methods as LDFE and MPM are relatively complicated and computationally expensive. A SDFE analysis is performed in this research to simulate the penetration and preloading process. The Wished-In-Place (WIP) and the Press-Replace (PR) method are two methods to be considered to simulate spudcan penetration.

The WIP method disregards any installation effects. In Hossain et al. (2006) a WIP method is used for the small strain analyses where a vertical-walled cylindrical cavity was assumed from soil surface down to spudcan depth. In Hossain and Randolph (2009a) a new approach for assessing spudcan penetration in clay is proposed. Results from small strain (using WIP method) and large deformation analyses in homogeneous clay are compared and show similar results up to deep penetrations. Hossain and Randolph (2009b) further describe the rate dependency of clay using a LDFE approach.

The PR method stepwise updates the geometry. As presented by Andersen et al. (2004) the method consists of a straining phase (Press) and a geometry update phase (Replace). Only the global stiffness matrix is updated without updating the mesh, resulting in a relative fast process compared to LDFE analyses. The PR method simulates the installation procedure and incorporates the installation effects. The method however is complex and a WIP method is adopted for this research.

Interface elements can be applied in the FE model to properly describe the interaction between the soil and the structure. The application of interface elements allows for potential slip planes and strength reduction in the soil body. These potential slip planes solve plasticity problems of singular points with peak values for stresses and displacements. Especially in the use of suction anchors the application of interface elements plays a crucial role in the accurate prediction of the bearing capacity (Andresen et al., 2008). However, inclusion of the interface elements requires accurate implementation as it affects the results and could lead to unreliable results. Evaluation of the need and complexity of including interface elements is further described

in section 3.2.1.

### 2.2.2 Constitutive model

PLAXIS is a finite element program in which different soil models are defined to simulate soil behaviour. Compressible soft soils like clay can be modelled using the Hardening Soil model (HS), Modified Cam Clay (MCC) model, Soft Soil (SS) model and the Soft Soil Creep (SSC) model (Brinkgreve et al., 2018b). As the first three models do not allow for time dependent behaviour like creep the SSC model is used in this research. Vermeer and Neher (1999) succeeded in formulating the soft soil model capable to capture creep by incorporating concepts of viscoplasticity and the MCC model, a critical state model describing stiffness stress dependency. The predominantly undrained conditions of clay result in viscous effects which play an important role during spudcan penetration while preloading. The model is not capable to account for hysteretic damping and accumulation of pore pressure due to cyclic loading. Only elastic strains will be generated when stress cycles are within the creep contour and plastic strains will be generated when the preconsolidation stress is further increased.

As the SSC model is not capable to model stress paths beyond the critical state line, no softening behaviour is captured by the model.

#### Soft Soil Creep model

In the SSC model the elastoplastic behaviour of soils is captured by elastic, creep and potential plastic failure strains. The creep strains are related to the change in pre-consolidation stress and only occur when a non-zero time interval is considered, the strains are obtained using a creep function. Figure 2.3a illustrates the logarithmic stress versus the strain for one-dimensional compression during the straining process. The stress is increased from the initial stress state up till the, arbitrary,  $\sigma'$  stress state. The increase in stress is applied for sufficient time which results in an increase of the pre-consolidation stress due to the creep effect.

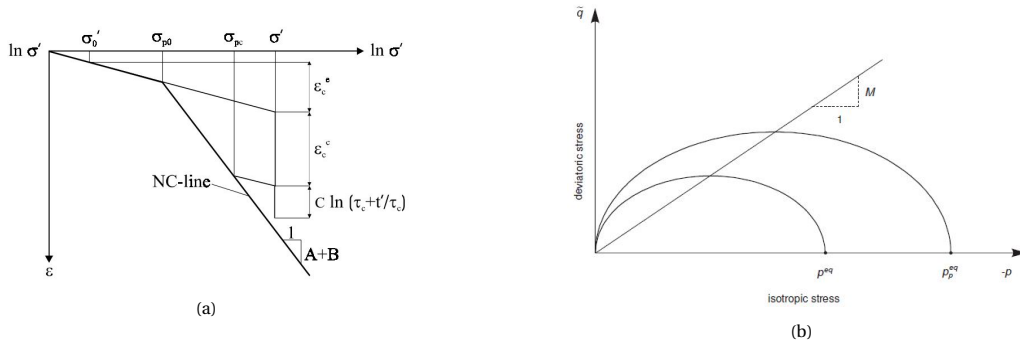


Figure 2.3: (a) 1D compression with elastic and creep strain increment components (Vermeer and Neher, 1999). (b)  $p^{eq}$  ellipse in p-q plane (Brinkgreve et al., 2018b).

This 1D situation serves as basis of the SSC model and the creep volumetric strain is determined using the equation:

$$-\dot{\epsilon}_v^c = \frac{\mu^*}{\tau} \left( \frac{p^{eq}}{p_p^{eq}} \right)^{\frac{\lambda^* - \kappa^*}{\mu^*}} \quad (2.2)$$

$\mu^*$ ,  $\kappa^*$  and  $\lambda^*$  are the modified creep, swelling and compression index respectively.  $\tau$  has a value of 1 and is the intrinsic time related to secular (creep) strain rate via  $\dot{\epsilon}_S = c/\tau$ , with c as the coefficient of rate of secular compression. The isotropic over-consolidation ratio (OCR) is defined as the inverse of the stress ratio  $p^{eq}/p_p^{eq}$ .  $p^{eq}$  is the equivalent pressure based on the current stress state and is formulated as:

$$p^{eq} = p' + \frac{q^2}{M^2 p'} \quad (2.3)$$

The equivalent pressure is constant along the path of the ellipse in the p-q plane. The equivalent pre-consolidation pressure is defined as:

$$p_p^{eq} = p_{p0}^{eq} * \exp\left(\frac{\epsilon_v^c}{\lambda^* - \kappa^*}\right) \quad (2.4)$$

The subscript 0 denotes the initial condition, at which the creep strains are zero. With  $p^{eq}$  being less than  $p_p^{eq}$  the magnitude of the creep strain is negligible. Parameter  $M$  represents the slope of the critical state line as illustrated in figure 2.3b. The critical state line represents the stress states at post peak failure.

To formulate the creep strain tensor, equation 2.2 is combined with the formulation of the plastic potential function which is assumed to be the same as equation 2.3. The creep strain direction is perpendicular to the ellipse for a certain stress state and is formulated as:

$$\dot{\epsilon}^c = \left( \frac{\partial p^{eq}}{\partial p} \right) \frac{\mu^*}{\tau} \left( \frac{p^{eq}}{p_p^{eq}} \right)^{\frac{\lambda^* - \kappa^*}{\mu^*}} \left( \frac{\partial p^{eq}}{\partial \sigma'} \right) \quad (2.5)$$

The elastic strains are related to the change in effective stress and are obtained using Hooke's law. The magnitude of the change (rate) in elastic volumetric strains is:

$$\dot{\epsilon}_v^e = \kappa^* * \frac{dp'}{p'} \quad (2.6)$$

Evaluation of equation 2.2 shows that a value of approximately 1.0 for OCR results in significant creep strain. The pre-consolidation stress increases as the creep strains increase, however only for the condition of a non-zero time domain. In the case of an OCR value larger than 1.0, the creep strain rate diminishes knowing that the expression  $(\lambda^* - \kappa^*)/\mu^*$  is in the order of 20. The SSC model requires input on parameters as listed in table 2.1.

Table 2.1: Input parameters for the SSC model.

Description	Symbol	Unit
Effective cohesion	$c$	Pa
Friction angle	$\phi$	deg
Dilatancy angle	$\psi$	deg
Modified swelling index	$\kappa^*$	-
Modified compression index	$\lambda^*$	-
Modified creep index	$\mu^*$	-
Poisson's ratio for unloading/reloading	$\nu_{ur}$	-
$\sigma'_{xx}/\sigma'_{yy}$ stress ratio in NC state	$K_0^{NC}$	-
$K_0^{NC}$ -related parameter	$M$	-

### Modified swelling, compression and creep indices ( $\kappa^*$ , $\lambda^*$ , $\mu^*$ )

The modified swelling and compression indices can be obtained from the relation between volumetric strain and mean stress during a loading/reloading test. In figure 2.4 the logarithm of the mean stress as function of the volumetric strain for an isotropic compression and unloading test is shown. The modified compression index  $\lambda^*$  corresponds to the primary loading path (compression) and the modified swelling index  $\kappa^*$  corresponds to the unloading/reloading path. The modified creep index  $\mu^*$  is obtained from the inclination of the volumetric strain as function of the logarithm of time, for a constant isotropic stress.

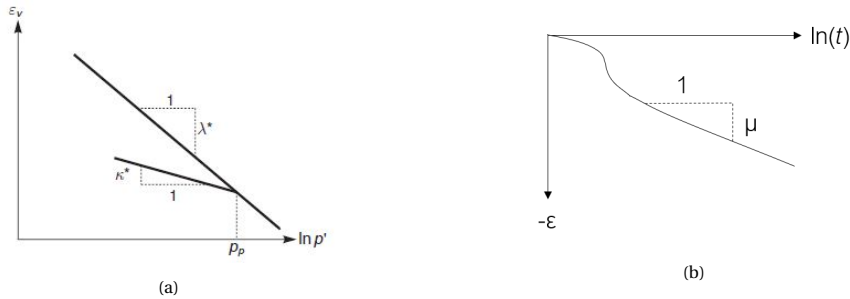


Figure 2.4: (a) Stress-strain behaviour for loading and unloading/reloading (Brinkgreve et al., 2018b). (b) Creep strain as function of time to determine the modified creep index.

### M parameter

The  $M$  parameter is a  $K_0^{NC}$ -related parameter. In the PLAXIS interface the value for  $K_0^{NC}$ , the lateral stress

coefficient in normal consolidation, can be specified from which automatically the value for  $M$  is determined. The relation between the two parameters is described as (Brinkgreve, 1994):

$$M = 3 \sqrt{\frac{(1 - K_0^{nc})^2}{(1 + 2K_0^{nc})^2} + \frac{(1 - K_0^{nc})(1 - 2\nu_{ur})(\lambda^*/\kappa^* - 1)}{(1 + 2K_0^{nc})(1 - 2\nu_{ur})\lambda^*/\kappa^* - (1 - K_0^{nc})(1 + \nu_{ur})}} \quad (2.7)$$

A higher value for  $M$  corresponds to a lower  $K_0^{NC}$  according to equation 2.7. A lower value for  $K_0^{NC}$  (or a higher value for  $M$ ) leads to less vertical settlements because the lateral deformations are increasingly constrained. Less lateral deformations automatically leads to a decrease in vertical settlement of the soil.

### Failure condition of SSC model

The Mohr-Coulomb type is adopted as the failure criterion in the SSC model. The Mohr-Coulomb failure yield criterion is related to the cohesion, the friction angle and the dilatancy angle. Touching the Mohr-Coulomb failure yield criterion plastic strains develop according to the flow rule:

$$\dot{\epsilon}^p = \lambda \frac{\partial g}{\partial \sigma'} \quad (2.8)$$

Due to the inclusion of this failure criterion the model is not capable of simulating material softening.

### Poisson's ratio

In the SSC model the Poisson's ratio is for unloading and reloading and the value is within the range 0.1 - 0.3. A small value for Poisson's ratio results in an increase in the horizontal-vertical stress ratio because the decrease in horizontal stress is higher than for vertical stress. This is an important phenomenon for over-consolidated materials. The Poisson ratio is calculated by dividing the difference in horizontal stress by the difference in vertical stress in oedometer unloading and reloading:

$$\frac{\nu_{ur}}{1 - \nu_{ur}} = \frac{\Delta \sigma_{xx}}{\Delta \sigma_{yy}} \quad (2.9)$$

### Over-consolidation ratio

The OCR of a soil depends on several factors, an essential factor is the elapsed time since deposition. For a normally-consolidated clay an OCR value of 1.0 would be legitimate. However, this corresponds to an elapsed time of one day since deposition in the SSC model. This would automatically lead to high values for creep strain rates and finally large and unrealistic settlements. A value in the range of 1.2-1.4 or even higher is advised (Brinkgreve et al., 2018b). In section 3.1.1 a thorough analysis is performed on the influence of the OCR on the soil behaviour.

### Visualisation of SSC model

When loading is applied the yield contour in the model expands due to hardening of the material. This hardening process occurs on the right side of the critical state line where the material is compacting. This (plastic) compaction is compensated by elastic expansion of the material as no volumetric strain can occur in undrained conditions. The elastic expansion is associated with a reduction of the effective stress, this process is visualized in figure 2.5.

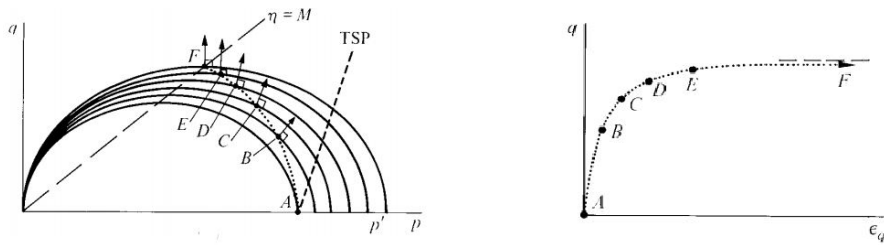


Figure 2.5: Effective and total stress paths in the  $q-p$  diagram (left) and the  $q-\epsilon_q$  diagram (right) for an undrained triaxial test (Muir-Wood, 1991).

As presented by Vermeer and Neher (1999) the SSC model is well capable to describe the dependency of the effective stress path and the undrained shear strength on the strain rate. These effects are visualized in

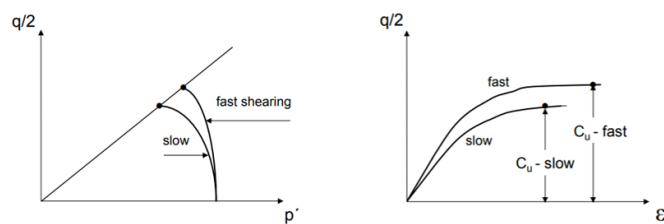


Figure 2.6: Dependency of the effective stress path and the undrained shear strength on the strain rate (Vermeer and Neher, 1999).

figure 2.6, depicting the undrained shear strength increase for a higher strain rate and the dependency of the effective stress path on the strain rate.

The SSC model describes a sharp distinction between the elastic and plastic strains. Due to this limitation no plastic strains are generated for a stress state within the yield boundary, this is known to be inaccurate especially for over-consolidated clays (Banerjee and Stipho, 1978). This phenomenon is incorporated in the model formulated by Shi et al. (2019), describing a bounding surface model incorporating time/rate effects based on the elastoplastic and viscoplastic overstress approach. The model allows time dependent viscoplastic deformations within the (bounding surface) elastic region. This model is not available for this research however.

### FE load stepping

As non-linear equations are solved in the finite element calculations, the step size and the solution algorithm affect the solution procedure. In this research the automatic load stepping procedure is adopted by the FE software for the loading calculations by performing load advancement to the ultimate level. For the procedure adopted during the consolidation calculations automatic time stepping is used.

In the automatic time step procedure the pre-defined final situation is compared to the initial situation. The final situation is reached in the final or a prior load step of the specific calculation phase. Via trial calculations and the pre-defined numerical control conditions the initial load step is determined. The final situation is defined as the load level to be reached which in this research is represented by the value for the spudcan preload target.

The arc-length control procedure is adopted to obtain the collapse loads during load-controlled calculations. The procedure converges towards a solution when the collapse load is approached and is an efficient procedure for problems with one or more critical points.

### FE formulation on consolidation

In the FE software the consolidation calculation is performed to analyse the dissipation of the excess pore pressures in the soil domain. The consolidation phase within the preload procedure is conducted after the loading phase. No additional penetration is applied and the load redistribution between the legs is initiated. The end of the consolidation calculation can be specified in three different ways. A minimum excess pore pressure, a time period or the degree of consolidation can be specified. In this research the time period criterion is adopted, the duration of each consolidation phase during the preload procedure is specified in the model. In PLAXIS compressive stresses are negative, the same applies to pore pressures such that negative excess pore pressures are used for compression.

## 2.3 Soil classification

The parameters of the cohesive soil determine the typical behaviour of the clay. During the site investigation, geotechnical properties are identified for all soil layers. These properties are used to set the design parameters of the constitutive soil model. The soil layers up to a depth of 35 m are considered and included in the FE model.

During the site investigation different tests are performed, including: cone penetration test (CPT), oedometer test, unconsolidated undrained (UU) triaxial test, consolidated undrained (CU) triaxial test and visual inspection. The results from the tests identify several soil layers in the subsurface as listed in table 2.2.

For convenience the CPT data is used to classify each of the layers according the classification chart by Robertson (2010), depicted in figure 2.7, using the normalized friction ( $R_f$ ) ratio and normalized cone resistance ( $Q_t$ ):

$$R_f = \frac{f_s}{q_t - \sigma_v} * 100\% \quad Q_t = \frac{(q_t - \sigma_{v0})}{\sigma'_{v0}} \quad (2.10)$$

Based on these results three independent soil layers are identified as the two sand layers are represented by a single layer in the model. The data points for both clay layers indicate that the clay tends to be over-consolidated over the whole depth. The two clay layers are considered separately however since the data in figure 2.7 suggests the top layer to be more over-consolidated compared to the second layer.

Depth [m]	Color	Classification
0.0 - 17.5	●	3 + 4 + 9
17.5 - 22.7	●	3 + 4
22.7 - 23.7	●	5 + 6
23.7 - 40.0	●	5 + 6

Classification no.	Soil type
1	Sensitive, fine grained
2	Organic soils
3	Clay
4	Silt mixtures
5	Sand mixtures
6	Sands
7	Gravelly to dense sand
8	Very stiff to clayey sand
9	Very stiff fine grained

Table 2.2: Classification of the different soil layers.

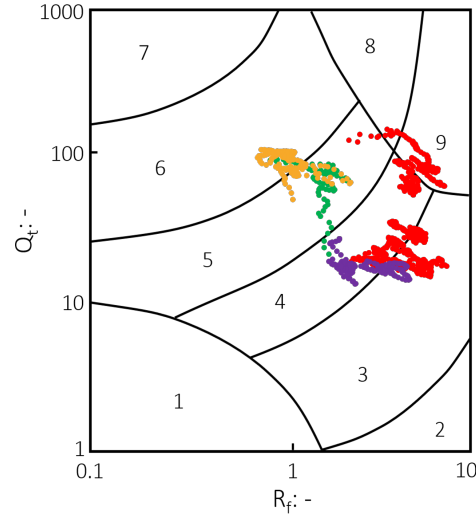


Figure 2.7: Classification chart according Robertson (2010).

The design parameters of the three soil layers are divided in three groups, the index properties, strength parameters and stiffness parameters. The parameter values are based on data retrieved from the CPT and laboratory tests. The sand parameters are determined from the CPT profile as this is the only available information for the layer. The clay parameters are mainly determined from the laboratory test results. These tests are performed on soil samples originating throughout the project site such that a reliable estimation for each of the parameter values is made. In appendix A calculations on the parameters and the results of the site investigation are presented in more detail.

In the final section the profile of the undrained shear strength over depth and the anisotropy of the soil is identified. It appears the anisotropy significantly influences the soil behaviour.

### 2.3.1 Index properties

The index properties of the soil include the unit weight ( $\gamma$ ), void ratio ( $e$ ), Poisson ratio ( $\nu$ ) and relative density ( $D_r$ ) of the soil. The unit weight of the soil is derived from the gravimetric water content ( $w$ ) and dry density ( $\gamma_d$ ) of the soil. The values for the unit weight are averaged over the depth range of the specific layer.

The void ratio is known at ten positions distributed over the project area and the depth, the values and positions are presented in figure A.1. In PLAXIS only one value for the void ratio can be specified for each layer, this single value suffices as the void ratio is relatively constant over depth for all layers.

The undrained behaviour of the clay results that both layers are nearly incompressible. This type of behaviour is associated with a Poisson ratio approaching a value of 0.5. This theoretical value represents the undrained Poisson ratio and would lead to singularity in the stiffness matrix, a value smaller than 0.5 is required in the model. The effective Poisson's ratio varies within the range 0.15-0.30.

Based on the plasticity chart and the classification chart for the clay layers, depicted in figure A.2 and 2.7 respectively, the layers are classified as almost impervious. The permeability is estimated to be in the order of  $10^{-5}$  m/day, based on generally accepted values for clays.

A useful parameter for sandy soils is the relative density,  $D_r$ . This value serves as basis to estimate the required constitutive model parameters. The relative density is determined from the CPT results according the relation

proposed by Jamiolkowski et al. (2001):

$$D_r = 100 * (0.268 * \ln(q_{t1}) - 0.675) \quad q_{t1} = \frac{q_t}{(\sigma'_{v0} * \sigma_{atm})^{0.5}} \quad q_t = q_c + u_2 * (1 - \alpha) \quad (2.11)$$

$q_t$  is the corrected cone resistance with  $\alpha$  as the net area ratio, a value of 0.5 is used for  $\alpha$ .  $u_2$  is the measured water pressure and for this sand layer a value of 0 is measured over the whole depth. The distribution of  $D_r$  over depth is shown in figure A.3 and an average value of 65% suffices to represent the whole layer. The values for the other sand parameters are based on generally accepted values for a dense sand.

Table 2.3: Index properties for each soil layer.  $v^*$  is the undrained and drained Poisson ratio for the clay and sand layers respectively.

Layer	Description	$\gamma$	$e_0$	$v^*$	$k$	$D_r$
[-]	[-]	[kN/m <sup>3</sup> ]	[-]	[-]	[m/day]	[%]
1	Clay	18.5	0.90	0.5	$10^{-5}$	-
2	Clay	20.5	0.67	0.5	$10^{-5}$	-
3	Sand	19.5	0.50	0.3	0.1	65

### 2.3.2 Strength parameters

Three strength parameters are specified for each layer: the internal friction angle, cohesion and dilatancy angle. The dilatancy angle is zero for the both clay layers and the cohesion is zero for the sand layer.

The friction angle and cohesion for both clay layers are determined from the Mohr circles at failure in an isotropically CU triaxial compression test. Only a limited amount of Mohr circles are available from the project soil data. Figure 2.8 depicts the Mohr circles and the failure envelope for both layers. Six Mohr circles correspond to a depth within clay layer 1 and two Mohr circles to a depth within clay layer 2. Since the Mohr circles vary in size a best fit for the failure envelope is estimated. The Mohr circle with the centre at 110 kPa deviates from the other circles, the cause for this deviation is not known. This Mohr circle is neglected in determining the failure envelope, this affects the strength parameters which is to be taken into account during analysis of the model results. Based on the Mohr circles and the undrained shear strength profile in figure 2.9, similar strength parameters for both clay layers are assumed. The difference between the clay layers is mainly visible in the stiffness parameters and unit weight. The cohesion,  $c$ , is set to 0 and the friction angle,  $\phi$ , is assumed to be  $30^\circ$ . Due to the limited information regarding the strength parameters both  $c$  and  $\phi$  are adjusted further during the soil model calibration to ensure the model results match the soil laboratory tests.

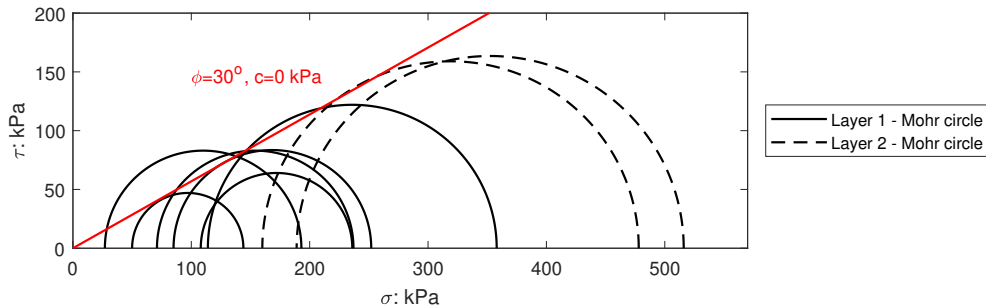


Figure 2.8: Mohr circles at failure and failure envelope in an isotropically consolidated undrained triaxial compression test.

The friction angle and dilatancy angle for the sand layer are determined from the CPT results. Using the formulas presented by Robertson and Campanella (1983) and Kulhawy and Mayne (1990) average values for the two strength parameters are determined. The results are depicted in the figures A.4a and A.4b.

### 2.3.3 Stiffness parameters

The stiffness of the two clay layers are described by the dimensionless compression index,  $C_c$ , and swelling index,  $C_s$ . Results from the oedometer tests are used to determine both indices. The compression index and swelling index represent the slope of the primary loading and unloading/reloading curve respectively. The results from the laboratory tests are depicted in figure A.5a and A.5b.

Table 2.4: Strength parameters for each soil layer.

Layer	Description	$\phi$	$c$	$\psi$
[-]	[-]	[deg]	[kPa]	[deg]
1	Clay	30	0	0
2	Clay	30	0	0
3	Sand	40	0	10

The stiffness for the sand layer is defined as the Young's modulus,  $E$ . Robertson (2009) describes the procedure to determine the Young's modulus from the CPT data, this procedure is only valid for uncemented and predominately coarse soils:

$$E = \alpha_E * (q_t - \sigma_v) \quad \alpha_E = 0.015 * (10^{0.55 * I_c + 1.68}) \quad (2.12)$$

$\alpha_E$  is the modulus factor and  $I_c$  the soil behaviour type index. The latter is calculated using the normalized friction ratio and normalized cone resistance (equation 2.10) respectively:

$$I_c = (3.47 - \log(Q_t))^2 + \left( (1.22 + \log(R_f))^2 \right)^{0.5} \quad (2.13)$$

The distribution of the Young's modulus over depth for the sand layer is presented in figure A.6. The value increases linearly with depth and is represented by the formula listed in table 2.5.

Table 2.5: Stiffness parameters for each soil layer.

Layer	Description	$C_c$	$C_s$	$E$
[-]	[-]	[-]	[-]	[kPa]
1	Clay	0.28	0.13	-
2	Clay	0.21	0.02	-
3	Sand	-	-	40 000 + 2150 * (z - 22.7)

### 2.3.4 Undrained shear strength profile

The profile of the undrained shear strength ( $s_u$ ) over depth is determined from the CPT according:

$$s_u = \frac{q_t - \sigma_v}{N_{kt}} \quad \alpha = 0.75 \quad N_{kt} = 26 \quad (2.14)$$

The equation is a general formula based on several theoretical proposals as described by Lunne et al. (1997). The value of 0.75 for  $\alpha$  is provided with the CPT measurements.  $N_{kt}$  is the empirical cone factor. The value for  $N_{kt}$  is determined by correlating the undrained shear strengths determined from the CU and UU triaxial tests with the corresponding  $q_t - \sigma_v$  values, from the CPT, at similar depths. A value of 26 is found to be appropriate for both clay layers. The profile and values of  $s_u$  following from respectively the CPT and the CU and UU triaxial tests are depicted in figure 2.9.

The undrained shear strength profile is compared to the empirical solution as suggested by Ladd and Foott (1974) which is defined as function of the effective overburden stress. The method makes use of the OCR of the soil to capture the influence of the stress history:

$$\frac{s_u}{\sigma'_{v0}} = \alpha * OCR^m \quad \alpha = \left( \frac{s_u}{\sigma'_{v0}} \right)_{NC} \quad (2.15)$$

Based on the findings of Ladd and Lee (1993) it is assumed  $m = 0.8$  and  $\left( \frac{s_u}{\sigma'_{v0}} \right)_{NC} = 0.22$ . The term  $\left( \frac{s_u}{\sigma'_{v0}} \right)$  in equation 2.15 represents the undrained strength ratio for a normally consolidated state. Schofield and Wroth (1968) and Mayne (1980) however suggested the parameter  $\alpha$  and  $m$  to depend on the friction angle and stiffness indices:

$$\alpha = \left( \frac{s_u}{\sigma'_{v0}} \right)_{NC} = \frac{3 * \sin(\phi') * e^{-\lambda}}{3 - \sin(\phi')} \quad m = \lambda = 1 - \frac{C_s}{C_c} \quad (2.16)$$

Table 2.6: Values for  $\alpha$  and  $\lambda$  for both clay layers according functions suggested by Schofield and Wroth (1968) and Mayne (1980).

Layer	$\alpha$	$\lambda$
1	0.35	0.54
2	0.24	0.90

For the two clay layers considered in this research the values are as listed in table 2.6.

The CPT and oedometer test data are used to determine the OCR distribution over depth, the profile is depicted in figure A.7. The OCR is determined from CPT data according to the formula suggested by Kulhawy and Mayne (1990):

$$OCR = k * Q_t \quad k = 0.25 \quad (2.17)$$

The Casagrande interpretation method is used to identify the OCR values for the soil samples with which oedometer tests are performed, the procedure is depicted in figure A.7. The values within the upper 5 m, following from the CPT, are extremely high and unreliable. The first clay layer is subdivided in three layers with different OCR and for the second clay layer the OCR is assumed constant. Table 2.7 lists the OCR values over depth.

Table 2.7: OCR over depth for both clay layers.

Layer	Depth [m]	OCR
1	0 - 8.0	7.0
	8.0 - 12.0	6.0
	12.0 - 17.5	5.0
2	17.5 - 22.7	4.0

The undrained shear strength profiles according Ladd and DeGroot (2003) and Mayne (1980) are illustrated in figure 2.9, starting from a depth of 6 m and an initial  $s_u$  of 60 kPa. The top part of the clay layer shows a high value for  $s_u$ , presumably caused by the presence of overburden pressure in the past.

The two clay layers are adjacent and as the value for  $s_u$  depends on the OCR the profile shows a jump at the depths with abrupt changes in OCR. The profiles according the CPT, Mayne (1980) and Ladd and Lee (1993) show similar trends for the first clay layer. For the second clay layer the  $s_u$  according the CPT and Ladd and Lee (1993) is significantly lower than the profile proposed by Mayne (1980). The undrained shear strength at the interface between clay layer 1 and 2 is approximately 100 kPa. The results indicate that the empirical formulas and the CPT coincide for the soil adopted in this research.

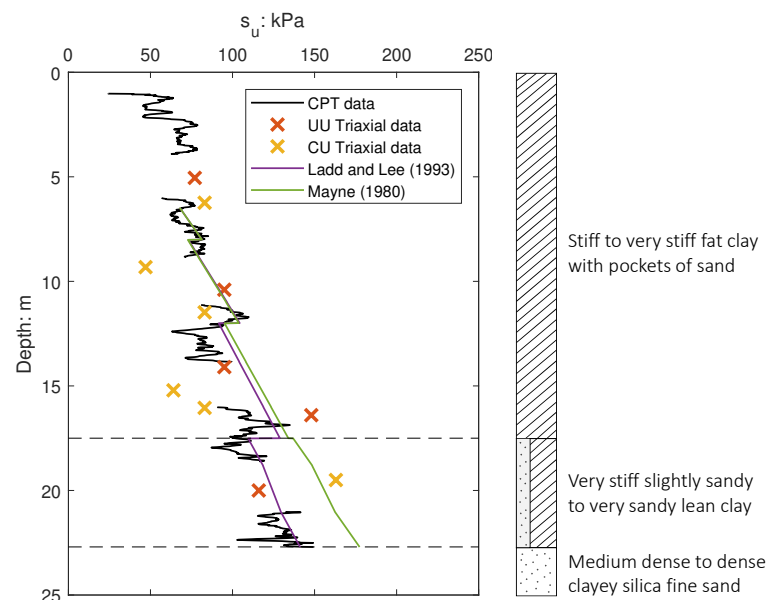


Figure 2.9: Undrained shear strength ( $s_u$ ) over depth for the clay layers between 0-22.7m, based on the CPT and CU triaxial test data and the procedures according Ladd and Lee (1993) and Mayne (1980).

### 2.3.5 Anisotropy

Isotropic linear elastic soil shows a perfectly straight stress path in a  $p'$ - $q$  plot for a CU triaxial test, indicating a constant mean effective stress. Since the stress paths for the over-consolidated soil samples from both layers are inclined, anisotropic elastic properties are expected. The stress path of the CU triaxial test for soil at a depth of 16.05 m is depicted in figure 2.10. The initial inclination of the stress path is defined as  $dq/dp'$ . Note that after the elastic phase non-linear contracting behaviour is initiated which causes inclination of the effective stress path. The relation between the mean and deviatoric stress and the volumetric and distortional

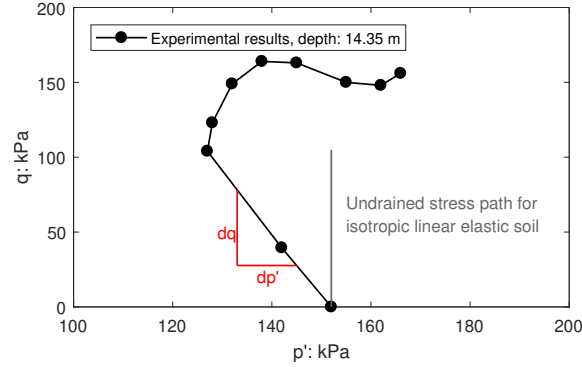


Figure 2.10: Triaxial test result at a soil depth of 14.35 m and the stress path for a perfect isotropic linear elastic soil.

strain for an anisotropic elastic material is shown in equation 2.18. The term  $J_1$  couples the mean effective stress to the distortional strain and  $J_2$  couples the deviatoric stress to the volumetric strain. The matrix is required to be symmetric considering thermodynamic considerations (Graham and Houlsby, 1983) such that  $J_1 = J_2 = J$ . In the ideal case of an isotropic material both these terms are equal to zero. By analysing the results of the oedometer and triaxial tests the high degree of anisotropy of the soil is proved. The dependency of the soil behaviour on the parameter  $J$  is examined.

$$\begin{bmatrix} dp' \\ dq \end{bmatrix} = \begin{bmatrix} K & J_1 \\ J_2 & 3G \end{bmatrix} \begin{bmatrix} d\epsilon_{vol} \\ d\epsilon_d \end{bmatrix} \rightarrow \begin{bmatrix} d\epsilon_{vol} \\ d\epsilon_d \end{bmatrix} = \frac{1}{\Delta} \begin{bmatrix} 3G & -J \\ -J & K \end{bmatrix} \begin{bmatrix} dp' \\ dq \end{bmatrix} \quad \Delta = \frac{1}{K * 3G - J^2} \quad (2.18)$$

The parameters  $K$ , the unloading/reloading stiffness, and  $G$ , the shear modulus, are pressure dependent. For the purpose of this research and for simplicity the pressure dependency is neglected and constant values for both parameters are assumed. The value for  $K$  and  $E$  are determined from oedometer and triaxial test results respectively.

$$K = \frac{\Delta p'}{\Delta \epsilon_v} \quad G = \frac{E}{2(1 + \nu)} \quad (2.19)$$

In the undrained triaxial test the volumetric strain,  $\epsilon_{vol}$ , is equal to zero and the following is true for an anisotropic soil:

$$\frac{dq}{dp'} = \frac{3G}{J_1} \quad (2.20)$$

The inclination of the CU triaxial stress path, as depicted in figure 2.10, is related to the parameters  $G$  and  $J_1$ . A soil with higher stiffness in horizontal direction shows a negative inclined stress path while a soil with a higher stiffness in vertical direction shows a positive inclined stress path (Graham and Houlsby (1983), Zwanenburg and Barends (2005)). The inclination of the effective stress path thus provides information about the degree of anisotropy. The results from figure 2.10 indicate an inclination of  $\approx -3G/4$  for the stress path.

It is interesting to investigate if the oedometer stiffness is dependent on  $J$ . The relation of the parameter to the oedometer stiffness is determined from equation 2.18. For the oedometer test the horizontal strain and change in horizontal strain are zero,  $\epsilon_h = 0$  and  $d\epsilon_h = 0$ . From the relation between the volumetric and distortional strain and the vertical and horizontal stress the change in horizontal strain is formulated as:

$$\begin{bmatrix} d\epsilon_{vol} \\ d\epsilon_d \end{bmatrix} = \begin{bmatrix} 2 & 1 \\ -2/3 & 2/3 \end{bmatrix} \begin{bmatrix} d\epsilon_h \\ d\epsilon_v \end{bmatrix} \rightarrow \begin{bmatrix} d\epsilon_h \\ d\epsilon_v \end{bmatrix} = \frac{1}{2} \begin{bmatrix} 2/3 & -1 \\ 2/3 & 2 \end{bmatrix} \begin{bmatrix} d\epsilon_{vol} \\ d\epsilon_d \end{bmatrix} \quad (2.21)$$

$$d\epsilon_h = \frac{1}{3}d\epsilon_{vol} - \frac{1}{2}d\epsilon_d = 0 \quad (2.22)$$

Using equation 2.18 this is reformulated:

$$d\epsilon_h = \frac{1}{3} \frac{1}{\Delta} (3G * dp' - J * dq) - \frac{1}{2} \frac{1}{\Delta} (-J * dp' + K * dq) = 0 \quad (2.23)$$

and the ratio  $dp'/dq$  follows from this formula in the form:

$$dp' \left( G + \frac{1}{2}J \right) = dq \left( \frac{1}{3}J + \frac{1}{2}K \right) \quad \frac{dq}{dp'} = \frac{6G + 3J}{2J + 3K} \quad (2.24)$$

Using the relation between the mean effective and deviatoric stress and the vertical and horizontal stress, the ratio  $d\sigma'_v/d\sigma'_h$  is calculated:

$$q_{max} = \sigma'_{v,max} - \sigma'_{h,max} \quad p'_{max} = \frac{1}{3} * \sigma'_{v,max} + \frac{2}{3} * \sigma'_{h,max} \quad (2.25)$$

$$\frac{d\sigma'_v}{d\sigma'_h} = \frac{3K + 4G + 4J}{3K - 2G + J} = \frac{A}{B} \quad d\sigma'_h = d\sigma'_v * \frac{B}{A} \quad (2.26)$$

With the relation between volumetric strain and vertical and horizontal stress in incremental form the oedometer stiffness can be calculated. The influence of  $J_1$  and  $J_2$  on the oedometer test results are identified and visualized. Implementation of equation 2.26 provides a relation between  $d\epsilon_v$  and  $d\sigma_v$ , representing the elastic oedometer stiffness.

$$d\epsilon_v = \frac{d\sigma_v}{E} - \frac{\nu}{E} 2 * d\sigma_h \quad \frac{d\sigma'_v}{d\epsilon_v} = \frac{E * A}{A - 2\nu * B} \quad (2.27)$$

$$A = 3K + 4G + 4J \quad B = 3K - 2G + J \quad (2.28)$$

The oedometer test at a depth of 14.35 m, subjected to a preconsolidation pressure of 500 kPa, is used as example. The parameters are listed in table 2.8. Knowing the value for  $G$ ,  $J$  is determined using the initial inclination of the triaxial test result. Based on these values the oedometer stiffness,  $E_{oed}$ , is determined.

Table 2.8: Parameter values to determine the elastic oedometer stiffness for an isotropic and an anisotropic soil.

$p_c$	E	$\nu$	$E_{oed}$	G	J	K
[kPa]	[kPa]	[-]	[kPa]	[kPa]	[kPa]	[kPa]
500	$16 * 10^3$	0.3	$34 * 10^3$	$5.6 * 10^3$	0	$90 * 10^3$
500	$16 * 10^3$	0.3	$34 * 10^3$	$5.6 * 10^3$	$-4.2 * 10^3$ ( $\approx -3G/4$ )	$60 * 10^3$

The test results indicate an unloading/reloading stiffness,  $K$ , of approximately  $50 * 10^3$  kPa. For the isotropic case as shown in table 2.8 ( $J=0$ ) a lower unloading/reloading stiffness is observed than for the anisotropic case ( $J \neq 0$ ). The influence of changing value of  $J$  on  $K$  is visualized in figure 2.11. For negative values for  $J$  the oedometer stiffness increases and the ratio  $\lambda^*/\kappa^*$  decreases. For positive values the oedometer stiffness decreases and the ratio  $\lambda^*/\kappa^*$  increases.

The oedometer results for the soil samples from clay layer 1 indicate a low unloading/reloading stiffness and a low  $\lambda^*/\kappa^*$  ratio. This stiffness is similar to the primary loading stiffness, while for most soils the unloading/reloading stiffness is significantly higher. A possible explanation for this observation could be the anisotropic behaviour of the clay.

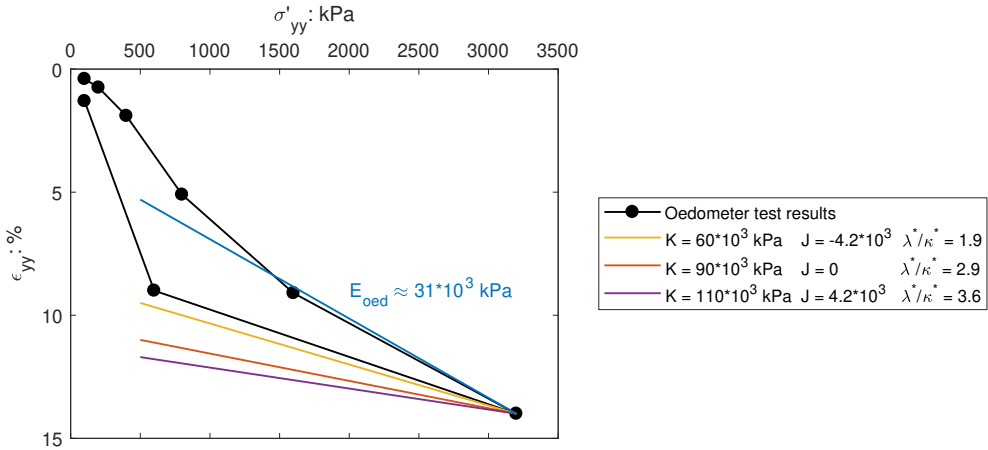


Figure 2.11: Oedometer test results for soil layer 1 at a depth of 14.35 m and influence of parameter  $J$  on the oedometer stiffness for  $G = 5.6 \cdot 10^3$  kPa.

One should take into account that the value for  $E_{oed}$ ,  $G$  and  $E$  are of influence on the unloading/reloading stiffness value. The moduli are pressure dependent and differ for other types of soil, the solution as presented here is only valid for this specific case. The feature anisotropy is not described by the SSC model and the influence is therefore disregarded in the model simulations.

## Model development

A 3D finite element model incorporating the three soil layers and the structural configuration of the vessel. The clay layers and sand layer are represented by the Soft Soil Creep (SSC) model and the Hardening Soil model with small-strain stiffness (HS-small) respectively (Brinkgreve et al., 2018b). To accurately consider the load redistribution within the flexible structure, the geometrical/mechanical properties of the structural members and the stiffness of the connection between the individual components are of importance. A leg extension mechanism is incorporated to simulate leg extension during the preload FE calculations. Structural data and models are provided by Van Oord and used to define the parameter values for the FE model.

### 3.1 Soil model

The soil model parameters are calibrated to accurately simulate the soil behaviour at the project site. Viscosity is excluded in a first approach using the Soft Soil (SS) model. Viscosity is taken into account in the final step by using the SSC model and calibrating the corresponding parameters. The calibration is performed by comparing the results of the laboratory tests on soil samples to the tests in the Soil Test function in PLAXIS (Brinkgreve et al., 2018a). The results of the laboratory tests and the different steps in the calibration procedure are presented in appendix F.

The sand layer is modelled using the Hardening Soil model with small-strain stiffness (HS-small). The specific model parameters for this layer are determined using the relative density, as presented in section 2.3.

#### 3.1.1 Clay layers

Two consecutive steps are performed to assign the correct values to the parameters of the SSC model. In the first step the soil parameters and undrained shear strength profile as presented in section 2.3 are used to derive the parameters of the SS model. This constitutive model type is suitable to simulate behaviour of compressible soft soils but excludes any creep influence. As the rate of strain applied in the triaxial tests is 0.21 %/hr the presence of strain-rate effects is assumed to be negligible. This assumption is proven to be valid from the results depicted in figure 3.7a and 3.7b. In the second step creep is included by using the SSC model and specifying the modified creep index,  $\mu^*$ . Since both clay layers are over-consolidated a cohesion higher than 0 kPa may be expected. Clay layer 1 is highly over-consolidated (OCR: 5-7) and a cohesion of 5 kPa is adopted as first approach. Clay layer 2 is a slightly less over-consolidated (OCR: 4) and a cohesion of 1 kPa is assumed. The set of model parameters is calibrated using the oedometer and triaxial test results available for both clay layers. The updated failure envelopes are depicted in figure 3.1.

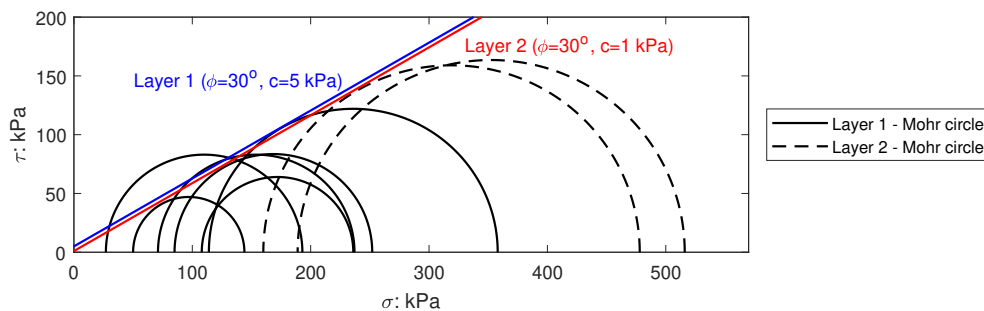


Figure 3.1: The updated failure envelopes of clay layer 1 and 2.

The value for the modified swelling and modified compression index are determined from the stiffness parameters, as defined in table 2.5. PLAXIS does not allow the ratio  $\lambda^*/\kappa^*$  to be smaller than or equal to 1, to

suffice this condition the value for  $\kappa^*$  of clay layer 1 is decreased to a value equal to  $\frac{1}{4}\lambda^*$ .

$$\lambda^* = \frac{C_c}{2.3(1+e)} \quad \kappa^* = \frac{2C_s}{2.3(1+e)} \quad \kappa^* \leq \frac{\lambda^*}{4} \quad (3.1)$$

The parameter  $K_0^{NC}$  and  $M$  are determined according:

$$K_0^{NC} = 1 - \sin(\phi) \quad M = 3 \sqrt{\frac{(1 - K_0^{nc})^2}{(1 + 2K_0^{nc})^2} + \frac{(1 - K_0^{nc})(1 - 2\nu_{ur})(\lambda^*/\kappa^* - 1)}{(1 + 2K_0^{nc})(1 - 2\nu_{ur})\lambda^*/\kappa^* - (1 - K_0^{nc})(1 + \nu_{ur})}} \quad (3.2)$$

As the parameter values for the SS model are known soil tests are performed using the Soil Test function in PLAXIS. The results of these tests coincide with the laboratory tests after calibration. In the following paragraph the calibration procedure and results are elaborated. First the stiffness parameters and secondly the strength parameters are calibrated.

### Stiffness parameters

The oedometer test results are used to calibrate the stiffness parameters  $\kappa^*$  and  $\lambda^*$ . The oedometer test and Soil Test results are depicted in figure 3.2a and 3.2b. The initial parameter values of clay layer 2 result in an accurate prediction of the loading-unloading profile, as depicted in figure 3.2b. The initial parameter values for clay layer 1 however over-predict the vertical strain with approximately 100%. The oedometer test results for clay layer 1 show a steep unloading curve close to the inclination of the loading curve, this indicated by the initial ratio  $\lambda^*/\kappa^*$  with a value close to 1. Adopting this ratio value in the model maximizes the inclination of the unloading curve, a smaller ratio value results in a decrease in inclination.

To match the vertical strain from the laboratory tests the values of both  $\kappa^*$  and  $\lambda^*$  are decreased. This adjustment also decreases the inclination of both the loading and unloading curve. In this case both the loading and unloading/reloading curve deviate from the laboratory results, as depicted by the yellow graph in figure 3.2a. It is therefore chosen to not substantially change the value for  $\lambda^*$  to ensure an accurate fit of the loading curve. The value for  $\kappa^*$  is decreased to predict the correct vertical strain, drawback is the deviation in the unloading curve. The blue graph depicted in figure 3.2a shows the loading and unloading/reloading curve following from the values of  $\lambda^*$  and  $\kappa^*$  adopted in the research. The steep unloading profile is not encountered in clay layer 2 and the initial parameter values suffice to match the loading-unloading profile. The final set of parameter values for both clay layers is listed in table 3.1.

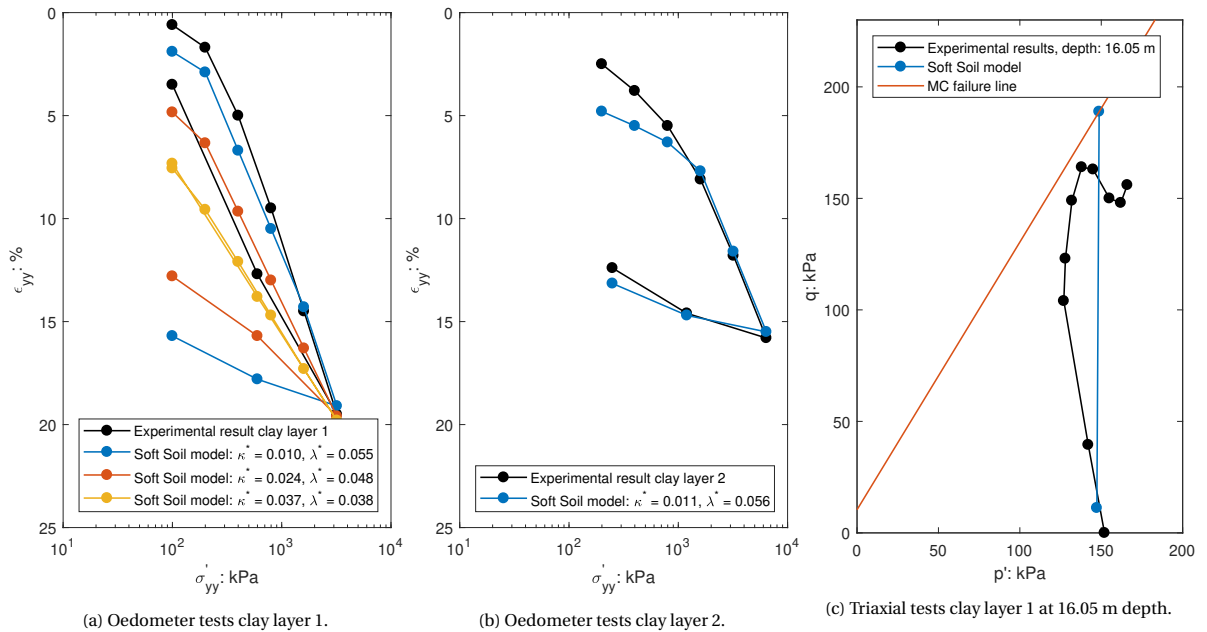


Figure 3.2: Laboratory and model test results for clay layer 1 and 2. The blue graphs indicate the results following from the parameter values adopted for the research.

### Strength parameters

The triaxial test results are used to calibrate the strength parameters  $\phi$  and  $c$ . Both parameters affect the value of  $K_0^{NC}$  and  $M$ . The parameters are adjusted to fit the CU triaxial results available in both soil layers. The SS model calculates a straight vertical stress path in the elastic region and the maximum strength is reached when the Mohr-Coulomb failure line is reached, as depicted in figure 3.2c. To match the actual strength profile at the project site the undrained shear strength is used as reference in the calibration procedure. The laboratory CU triaxial test results indicate deviation in the  $s_u$  profile over depth, the SS model is calibrated such that an sufficient average profile is predicted.

The calibration of the model requires an accurate estimate of the preconsolidation pressure of the soil samples for the triaxial tests to achieve reliable results in terms of strength and pore pressure. The isotropic consolidation phase of the soil samples is expected to follow the path as shown in figure 3.3, with zero deviatoric stress. Anisotropic soil however follows a more skewed stress path as the horizontal and vertical strain are not equal.

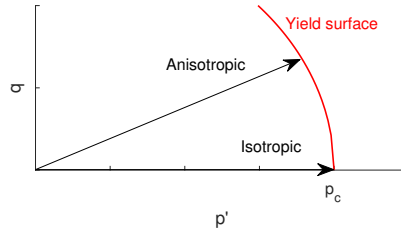


Figure 3.3: Stress path for isotropic consolidation of isotropic and anisotropic soil.

The anisotropic soil crosses the yield surface for a value of  $q$  higher than zero and the corresponding mean effective stress is lower than the preconsolidation pressure. The point where the yield surface crosses the  $p'$  axis corresponds to the value of the preconsolidation pressure,  $p_c$ , as depicted in figure 3.3. For anisotropic soil the value for  $p_c$  is determined with the initial effective vertical stress ( $\sigma'_{v,0}, \sigma'_{h,0}$ ), OCR and the earth pressure coefficient ( $K_0$ ). The initial effective stress is equal to the effective cell pressure and by using the OCR profile from figure A.7 the maximum effective horizontal stress is calculated:

$$\sigma'_{v,max} = OCR * \sigma'_{v,0} \quad \sigma'_{h,max} = K_0 * \sigma'_{v,max} \quad K_0 = (1 - \sin(\phi)) * OCR^{\sin(\phi)} \quad (3.3)$$

The deviatoric and effective mean stress are calculated using these parameters according equation 2.25. The preconsolidation pressure,  $p_c$ , is calculated using the yield function describing the yield surface as depicted in figure 3.3:

$$p' = \frac{q^2}{M^2 (p' + c * \cot(\phi))} \quad (3.4)$$

$K_0$  and  $p_c$  are both calculated for each triaxial test and used as model input parameters. The calibrated SS model parameter values for both layers are listed in table 3.1. Important to note is that clay layer 1 is subdivided in three layers adopting different values for the OCR (table 2.7).

Table 3.1: Calibrated Soft Soil parameters for clay layer 1 and 2.

Layer	$\gamma$	$e_0$	$\nu$	$k$	$\phi$	$c$	$\psi$	$\lambda^*$	$\kappa^*$	$K_0^{NC}$	$M$
[-]	[kN/m <sup>3</sup> ]	[-]	[-]	[m/day]	[deg]	[kPa]	[deg]	[-]	[-]	[-]	[-]
1	18.5	0.90	0.3	$10^{-5}$	30	5	0	0.055	0.010	0.5	1.65
2	20.5	0.65	0.3	$10^{-5}$	30	1	0	0.056	0.011	0.5	1.65

### Calibration results

The undrained shear strength profile following from the laboratory tests and the model are depicted in figure 3.4. The  $s_u$  profile at 0-9 m depth calculated by the model is significantly lower than the CPT results. The high values for  $s_u$  in the top layer are presumably caused by the presence of overburden pressure in the past. For depths higher than 9 m the deviation is less and a similar profile is observed. Since the initial spudcan depth is  $\geq 10$  m the  $s_u$  values below this depth are more relevant than the top 10 m. For the purpose of the FE model

a satisfying, conservative,  $s_u$  profile is calculated by the constitutive model.

$$s_{u,SS} = 10 + 5.1 * z \quad \text{for } z \leq 17.5 \quad (3.5)$$

$$s_{u,SS} = 91 + 5.2 * (z - 17.5) \quad \text{for } 17.5 \leq z \leq 22.7 \quad (3.6)$$

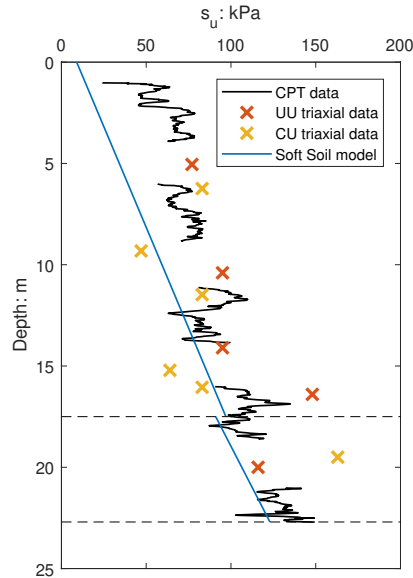


Figure 3.4: Undrained shear strength ( $s_u$ ) profile over depth for the clay layers between 0-22.7 m as calculated by the Soft Soil model.

Figure 3.5a and 3.5b show the undrained shear strength and excess pore pressure for continuous shearing of the soil sample from a depth of 16.05m. The stiffness following from the model is similar to the actual soil stiffness as the inclination of the elastic straining for both graphs coincide, figure 3.5a. Also the generation of the negative pore pressures, due to the dilative behaviour of the heavily over-consolidated clay, is calculated by the model. The maximum value for the strength as calculated by the model matches the value from the laboratory tests and the model slightly underestimates the maximum value of the excess pore pressure. The laboratory tests results show the undrained shear strength and excess pore pressures tend to decrease after the peak value for continuous shearing is reached. This is caused by softening of the soil and typical for heavily over-consolidated clay. Since softening is not included in the SS and SSC model no peak strength is visible in the model results.

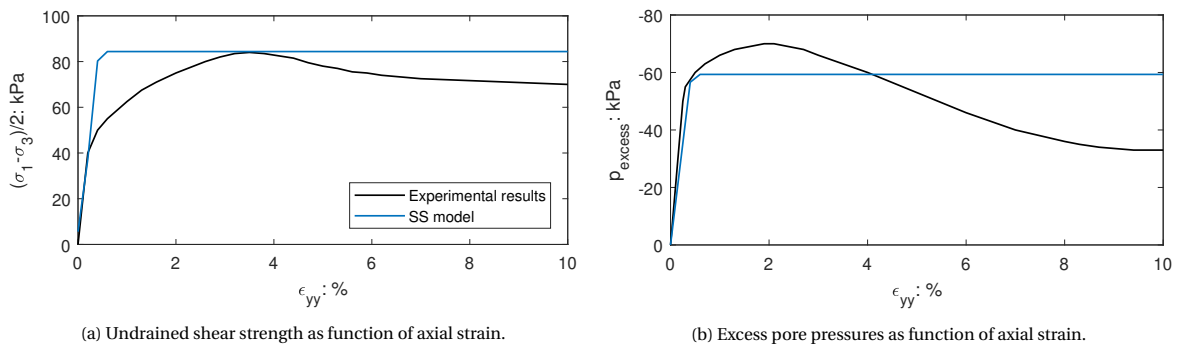


Figure 3.5: Results of the laboratory and Soft Soil model CU triaxial tests for clay layer 1.

### Creep inclusion

Switching from the SS model to the SSC model the modified creep index,  $\mu^*$ , is the only additional parameter. The parameter  $\mu^*$  can be obtained by measuring the volumetric strain on the long term and plotting it against the logarithm of time (Vermeer and Neher, 1999). In general the relation  $\lambda^*/\mu^*$  is in the range 15-25 and this ratio can be used as rough estimate for  $\mu^*$  Brinkgreve et al. (2018b). Increasing the value for  $\mu^*$  results in an

increase of the undrained shear strength and a higher stress path in the  $q-p'$  plane, as visualised in the figures F.6a - F.7b. As first estimate a value for  $\mu^*$  equal to  $\lambda^*/20$  is adopted. The effect of the choice for the value of  $\mu^*$  for a normally consolidated situation is visualised in figures F.6a - F.7b. For both clay layers increasing the parameter value results in an increase of the undrained shear strength.

Table 3.2: Values for the modified creep index,  $\mu^*$ , for both clay layers.

Layer	$\mu^*$
[ - ]	[ - ]
1	$2.75 * 10^{-3}$
2	$2.75 * 10^{-3}$

As stated in section 2.2.2 the value for the OCR parameter in the SSC model should be chosen with care. The yield surface in the SSC model is time dependent, a value of 1.0 for the OCR parameter corresponds to an elapsed time of 1 day since deposition. This would automatically lead to high values for creep strain rates and consequently large and unrealistic settlements, even without any external loading. The history of the soil should be represented by a proper OCR value and it is advised to set the OCR value in the order of 1.2-1.4 (Brinkgreve et al., 2018b) for a normally consolidated soil. Varying the OCR value in the model automatically changes the pre-consolidation pressure. To determine the exact value for the OCR model parameter to represent a NC soil with OCR equal to 1.0, the creep strain rate equation is used:

$$-\dot{\epsilon}_v^c = \frac{\mu^*}{\tau} \left( \frac{p^{eq}}{p_p^{eq}} \right)^{\frac{\lambda^* - \kappa^*}{\mu^*}} \quad (3.7)$$

In this expression the ratio  $p^{eq}/p_p^{eq}$  is the inverse of the OCR. By combining equation 3.7 with the creep strain rate as function of time,  $\dot{\epsilon} = \frac{\mu^*}{t}$ , an expression for OCR depending on the time is found:

$$OCR = \left( \frac{t}{\tau} \right)^{\frac{\mu^*}{\lambda^* - \kappa^*}} \quad (3.8)$$

Both the OCR and shear strain rate as a function of time are depicted in figure 3.6. As the values for  $\lambda^*$ ,  $\kappa^*$  and  $\mu^*$  are similar for both clay layers the corrected OCR value is valid for both layers. It is seen that for an OCR close to 1.0 the creep strain rate is extremely high. These unrealistic high rates are eliminated by using a higher OCR, for this specific problem an OCR of 1.4 is adopted.

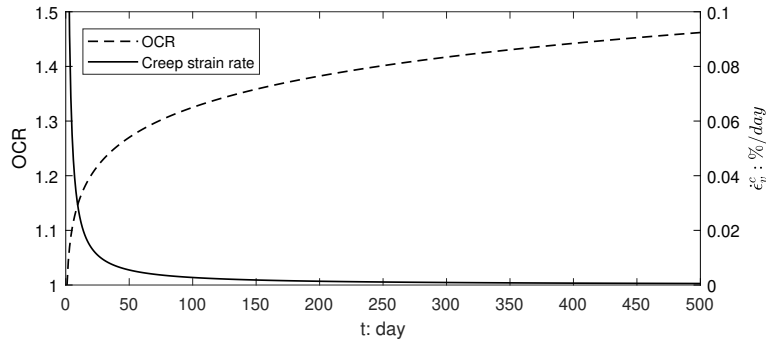


Figure 3.6: OCR and creep strain rate as function of time (equation 3.7 and 3.8).

### Strain rate effect

The effect of the strain rate differs for each soil type. Zhou and Randolph (2007) propose an empirical relation between the undrained shear strength and strain rate:

$$s_u = \left( 1 + \mu \log \left( \frac{\dot{\epsilon}_a}{\dot{\epsilon}_{ref}} \right) \right) * s_{u,ref} \quad (3.9)$$

$\dot{\epsilon}_{ref}$  is the reference shear strain rate at a strain rate varying from 1 – 4 %/h for triaxial tests (Hossain and Randolph, 2009b) and  $\mu$  is the rate of the strength increase per decade of strain rate with a range of 0.05 to 0.2. With this formula the increase in undrained shear strength for a given strength profile is calculated for a given strain rate. Below the reference shear strain rate, the undrained shear strength is rate independent. The choice of the rate parameter,  $\mu$ , depends on the preconsolidation pressure and the soil parameters.

The influence of the strain rate and the preconsolidation pressure on the strain rate for both clay layers from this research, is investigated by simulating CU triaxial tests with the SSC model and adopting the parameters as listed in table 3.1. The rate independent SS model is used to determine the reference strain rate, which is defined as the strain rate for which the undrained shear strength in the SSC model coincides with the shear strength from the SS model. The results of this analysis are summarized in figures F.8a - F.10f.

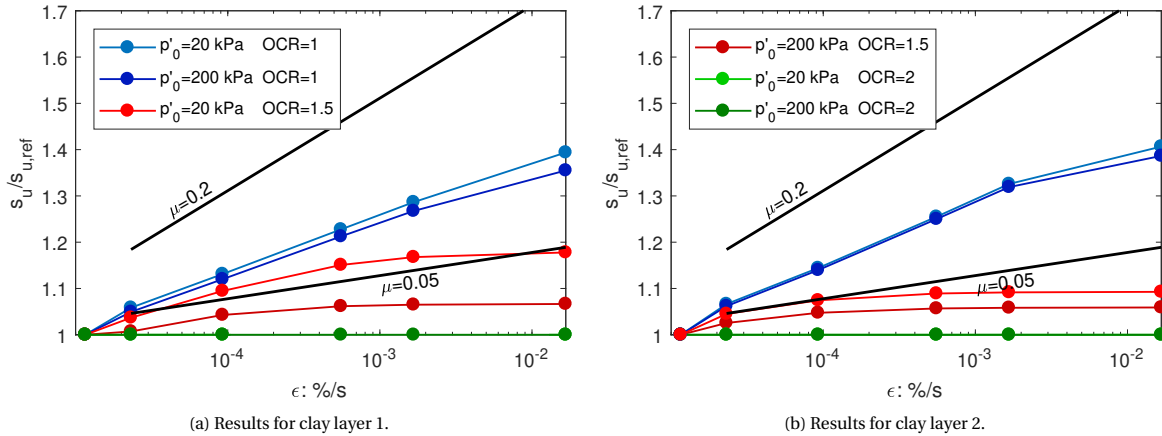


Figure 3.7: Relation between the undrained shear strength ratio and the strain rate for different preconsolidation pressures and initial confinement using a semi-log scale.

Based on this analysis the relation between the undrained shear strength ratio ( $s_u/s_{u,ref}$ ) and the strain rate for different preconsolidation pressures and initial confinement is determined for each layer. These relations are illustrated on a semi-log scale for the strain rate in figures 3.7a and 3.7b. The range for  $\mu$  as proposed by Zhou and Randolph (2007) is added to the figures.

The model indicates that the influence of the strain rate is significant for an  $OCR \leq 1.5$  for clay layer 1 and 2. The undrained strength ratio is also affected by the initial confinement pressure,  $p'_0$ . By comparing two different values for the initial confinement (20 and 200) it is seen that a lower confinement results in higher influence of the creep strains. At lower initial confinement the relative influence of the cohesion on the soil strength is higher than for higher initial confinement. This is valid for both clay layers, the influence of the initial confinement however is larger for clay layer 1. This is caused by the difference in cohesion and OCR for both layers, the cohesion is 5 and 1 kPa for clay layer 1 and 2 respectively. A higher cohesion increases the relative difference in soil strength for different initial confinement. The results further indicate that the model calculates that for higher OCR values the relative difference in soil strength at different initial confinement increases. This is only valid for  $OCR \leq 1.5$ , for the soils investigated in this research.

Zhu and Yin (2000), Sorenson et al. (2007) and Lehane et al. (2009) indicate that the over-consolidation ratio does not seem to affect the general strain-rate dependent behaviour. Test results are presented in these researches which however indicate that the magnitude of strain-rate influence is slightly more significant for lower  $OCR (\leq 2)$  than for higher OCR.

Both clay layers have an initial OCR of 4-7, indicating the creep influence calculated by the model is negligible. However, when the spudcan penetrates the vertical stress increases considerably and the OCR tends to decrease depending on the drainage conditions. In the case  $OCR \leq 1.5$  significant creep will occur. The decrease in OCR is further analysed in section 4.1.3.

### 3.1.2 Sand layer

The present sand layer will be modelled with the constitutive Hardening Soil model with small-strain stiffness. To approximate the soil properties with only limited data Brinkgreve et al. (2010) related the HS model parameters to the relative density,  $D_r$ . Due to the absence of laboratory tests on the sand layer no calibration of the model parameters is performed.

Table 3.3: Parameters for the sand layer determined from the CPT.

$\gamma_{sat}$	$\nu_{ur}$	$c$	$\phi$	$\psi$	$D_r$
[kN/m <sup>3</sup> ]	[-]	[kPa]	[deg]	[deg]	[%]
19.5	0.3	0	40	10	65

The relations to quantify the model parameters  $E_{50}^{ref}$ ,  $E_{oed}^{ref}$ ,  $E_{ur}^{ref}$ ,  $m$ ,  $R_f$ ,  $G_0^{ref}$  and  $\gamma_{0.7}$  based on  $D_r$  are:

$$E_{50}^{ref} = 6 * 10^5 * \frac{D_r}{100} \quad E_{oed}^{ref} = 6 * 10^5 * \frac{D_r}{100} \quad E_{ur}^{ref} = 18 * 10^5 * \frac{D_r}{100} \quad (3.10)$$

$$m = 0.7 - \frac{D_r}{320} \quad R_f = 1 - \frac{D_r}{800} \quad (3.11)$$

$$G_0^{ref} = 60000 + 68000 * \frac{D_r}{100} \quad \gamma_{0.7} = \left(2 - \frac{D_r}{100}\right) * 10^{-4} \quad (3.12)$$

Brinkgreve et al. (2010) also suggested a relation for the friction angle and dilatancy angle both depending on  $D_r$ . These relations lead to similar values as the relations proposed by Robertson and Campanella (1983) and Kulhawy and Mayne (1990) and are presented in section 2.3.2. The parameter values for the sand layer are listed in table 3.4.

Table 3.4: HS-small parameters for the sand layer based on the formulations suggested by Brinkgreve et al. (2010).

$E_{50}^{ref}$	$E_{oed}^{ref}$	$E_{ur}^{ref}$	$m$	$p_{ref}$	$R_f$	$G_0^{ref}$	$\gamma_{0.7}$
[kPa]	[kPa]	[kPa]	[-]	[kPa]	[-]	[kPa]	[-]
39000	39000	117000	0.5	100	0.92	104200	$1.35 * 10^{-4}$

The HS-small model allows for the inclusion of the following four features, the theory of plasticity, soil dilatancy, a yield cap and the very small-strain stiffness and its non-linear dependency.  $E_{50}^{ref}$ ,  $E_{oed}^{ref}$  and  $E_{ur}^{ref}$  respectively represent the triaxial stiffness at 50% of the maximum deviatoric stress for a certain reference cell pressure, the oedometer stiffness for a certain vertical pressure and the triaxial unloading/reloading stiffness for a certain cell reference pressure. Each of the reference stiffness moduli are used in combination with the parameter  $m$  to determine the stress dependent stiffness moduli  $E_{50}$ ,  $E_{oed}$  and  $E_{ur}$ .

The shear modulus depends on the level of shear strain since decay of the stiffness is caused by the loss of intermolecular and surface forces in the soil. In the HS-small model the parameters  $G_0$  and  $\gamma_{0.7}$  are used to describe the shear stiffness dependency. The normalized elastic shear modulus of soil shows an S shaped profile when plotted as function of the shear strain. The actual shear modulus is normalized to the initial (or maximum) shear modulus  $G_0$ .  $\gamma_{0.7}$  defines the secant shear modulus which is 72.2% of the initial value. In the HS-small model the unloading curve for the shear modulus is similar to the initial loading curve while the unloading/reloading curves are twice the value for the loading curve.

A yield surface for the shear and volumetric hardening enable the model to simulate hardening behaviour. The failure ratio,  $R_f$ , defines the ratio between the ultimate deviatoric stress and the shear strength.

### 3.2 Structural model

The industry guideline (SNAME, 2008) and standard (ISO, 2016) comprises three levels of foundation stability assessment with increasing order of complexity. In the so-called Displacement Check (Step 3) the load redistribution resulting from the overload and displacement of spudcans are accounted for. The jacking and preloading processes addressed in this report thus correspond to the Step 3 assessment from the guideline and standard. The techniques for modelling the different structural members including various levels of modelling, applicable to specific type of assessments, include:

1. Fully detailed leg model
2. Equivalent leg (Stick model)
3. Combined equivalent/detailed leg and hull model
4. Detailed single leg and leg-to-hull connection model

Each level consists of advices on the implementation of each of the structural members in the model. The results of the first three level models can be used to examine the preload requirements. In this research a model corresponding 'Equivalent leg (Stick model)' level is used.

General geometrical/mechanical properties of the Aeolus are summarized in table 3.5. Based on these properties the structural model is constructed, further specifications of the structural members are provided in the sections below.

Table 3.5: Geometrical and mechanical properties of Aeolus.

Description	Value	Unit
Length hull	139.4	m
Width hull	38.0	m
Depth hull	9.1	m
Leg length	89.3	m
Longitudinal leg spacing	69.3	m
Transverse leg spacing	29.0	m
Leg diameter	4.5	m
Maximum spudcan diameter	13.0	m
Maximum elevated weight	28000	t

Normalization of confidential data is applied throughout the report. Confidential data includes the leg loads, the spudcan penetration and the penetration rate:

$$F_{leg-norm.} = \frac{F_{leg}}{F_{leg-max.}} \quad u_{spud-norm.} = \frac{u_{spud}}{u_{spud-max}} \quad v_{spud-norm.} = \frac{v_{spud}}{v_{spud-max}} \quad (3.13)$$

The parameter  $F_{leg-max}$  defines the maximum measured leg load during the preload procedure at the project site,  $u_{spud-max}$  defines the maximum spudcan penetration measured at the project site and  $v_{spud-max}$  defines the maximum penetration rate applied during the preload procedure at the project site. In appendix K the normalization is further described and the values for each of the parameters are provided.

### 3.2.1 Spudcan

The deformations of the spudcans are negligible. The spudcan and the part of the leg below the seabed are modelled as rigid bodies and the axial and bending stiffness are neglected for this part of the structure. The geometry and corresponding dimensions of the spudcan are visualized in figure 3.8a.

The connection between the spudcan and the leg is assumed to be rigid as a finite stiffness of this connection would lead to insufficient structural integrity. As stated by Pisanò et al. (2019) a rigid connection is in agreement with reality and is in accordance with previous research (Bienen and Cassidy (2006), Bienen and Cassidy (2009), Dean and Metters (2009), Vlahos et al. (2011), Zhang et al. (2014), Cassidy et al. (2010), Cassidy (2011)).

The soil structure interaction is modelled using interface elements. The application of interface elements allows for potential slip planes in the soil body. The elements could be used to introduce soil strength reduction for a certain width and solve plasticity problems of singular points with peak values for stresses and displacements. Especially around the corners of the spudcan geometry, unrealistic high peaks in stresses and strains are obtained. By allowing for slip planes flexibility of the finite element mesh is tolerated and unrealistic stress results are prevented. The interfaces are applied along the outside surfaces of the spudcan.

The structure below the seabed includes the spudcan and a part of the leg, the geometry comprises of several corners and introduces sharp angles within the soil domain. Calculations using the exact spudcan shape show non-physical stress results at these corners. These results are only present in a relatively small volume of the soil, extending 0.5 m from the corners, and the impact on the bearing capacity is limited. However, the unrealistic high stresses and pore pressures do not allow for a consolidation calculation phase as severe divergence of the results is observed. The application of and variation in the interface elements in combination with the complex geometry does not improve the results.

To limit the number of sharp corners the shape of the structure within the soil domain is simplified as depicted in figure 3.8b. The spudcan is equipped with a perfectly horizontal bottom boundary. Interfaces are applied along the outside surfaces of the structure to exclude singularities. The interfaces are extended 1 m into the soil domain to avoid the corners of the spudcan to be fixed to the soil. For the SSC model the strength

reduction factor,  $R_{inter}$ , is used to define the strength and stiffness of the soil surrounding the structure. No strength reduction is applied as  $R_{inter} = 1.0$  is adopted in the model, meaning the interface and soil properties are exactly similar.

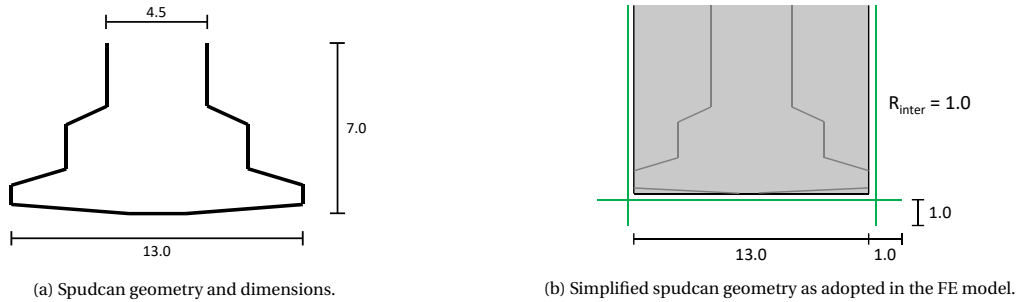


Figure 3.8: Actual and simplified spudcan shape. All dimensions are in m.

The influence of simplifying the spudcan structure on the bearing capacity and penetration is negligible. Appendix B presents an analysis of the influence of different spudcan shapes and interface configurations on the capacity and penetration.

During spudcan penetration a cavity can develop on top of the spudcan. The depth at which the cavity wall fails depends on the soil characteristics. In this research complete backfill into the cavity is assumed. The weight of the soil volume filling the cavity is subtracted from the observed bearing capacity to determine the actual leg load.

The volume of the simplified spudcan-cylinder is a summation of the volume of the spudcan and the volume of the surrounding soil extending to a distance of 6.5 m from the mid-leg axis. The total volume of the cylinder is  $13.7 \text{ m}^2$  multiplied with the reference spudcan depth. This soil volume within the cylinder is equal to  $95.7 \text{ m}^2$  multiplied with the reference spudcan depth and holds an effective unit weight weight of  $8.1 \text{ kN/m}^3$ . It should be noted that the leg load from the jacking data and the soil weight as elaborated above represent the effective loads. The uplift force for the total cylinder is equal to 137 multiplied with the reference leg load.

### 3.2.2 Extension mechanism

During the preloading procedure the leg pairs are alternately lowered and loaded up to predefined loads. To simulate the gradual extension of the legs during the calculations the use of node-to-node anchors is adopted in this research. Another possibility is the application of surface contraction on a plate, this method is explained in appendix C.

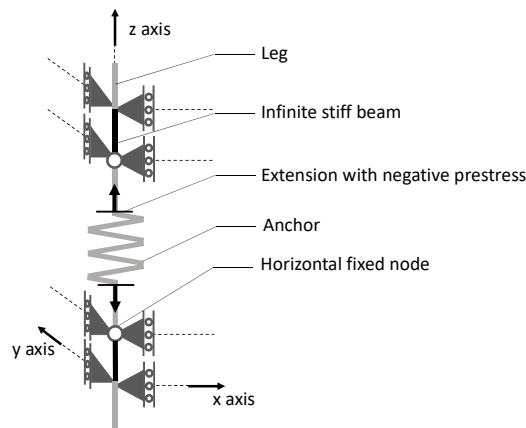


Figure 3.9: Schematisation of the node-to-node anchor as leg extension mechanism.

The node-to-node anchor is a separate structural member representing a spring connection. The anchor requires specification of the axial stiffness and an infinite bending stiffness is assumed. The node-to-node anchor can be extended or contracted during each calculation phase by assigning a pre-stress value. Pre-stress tension force is positive and leads to contraction, compression force is negative and leads to extension. At the

final step of the calculation phase the specified pre-stress force is applied. In the following calculation phases the length of the anchor is constant, offering the possibility to extend/contract anchors independently. The connection between the node-to-node anchor and the leg (represented as a beam element in the FE model) is hinged meaning that no moments are transferred through the connection. To overcome an unstable equilibrium the nodes connected via the node-to-node anchor should be fixed in horizontal direction ( $x$ ,  $y$ ), the mechanism is visualized in figure 3.9. A stable equilibrium is established but the horizontal fixation influences the behaviour of the leg itself. Positioning the extension mechanism at the top of the leg, below the leg-hull connection, prevents the corner points of the structure to translate in horizontal direction which influences the overall structural behaviour. To limit this influence the mechanism and corresponding horizontal fixations are positioned just above the seabed. This ensures the actual stiffness behaviour of the hull structure and the leg above the extension mechanism is maintained. The part of the leg below the extension mechanism is assumed to be infinite stiff and will not be able to rotate and move in horizontal direction. To simulate a rigid connection between the extension mechanism and the leg, an infinite stiff beam with a length of 0.1 m and horizontally fixed outer-end nodes are added on both sides of the mechanism.

### 3.2.3 Leg

The legs of the Aeolus are hollow cylinders and the geometrical and mechanical properties are listed in table 3.6. The part of the leg below the seabed is modelled as a rigid body, for the part of the leg above the seabed the actual leg stiffness is adopted.

Table 3.6: Geometrical and mechanical properties of the legs.

$D$	$t$	$E$	$f_y$	$\nu$	$W_{x,y}$	$I_{x,y}$
[m]	[m]	[kPa]	[kPa]	[-]	[m <sup>3</sup> /m]	[m <sup>4</sup> ]
4.5	0.1	210*10 <sup>6</sup>	690*10 <sup>3</sup>	0.3	1.488	3.347

The part of the leg above the seabed can be modelled using 3-node line elements or 6-node triangular elements. In the case of line elements the pile is represented as a thin line in the FE model and does not occupy any volume. In the case of triangular elements the pile is represented as a cylindrical hollow plate and the true volume of the pile is occupied.

Both type of elements allow for six degrees of freedom per node ( $u_x$ ,  $u_y$ ,  $u_z$ ,  $\phi_x$ ,  $\phi_y$ ,  $\phi_z$ ) and are based on Mindlin's theory for plates (Bathe, 1982) and Timoshenko's theory for beams (Timoshenko, 1921), allowing for deformations due to shearing as well as bending. The axial bending stiffness for the leg represented by beam or plate elements are exactly the same, generating the same results in axial loaded and bending problems. For the same accuracy in results the number of nodes and elements for the structure represented by beam elements is approximately one order of magnitude lower than the structure represented by plate elements. Considering the computation time and costs it is chosen to represent the legs by beam elements.

### 3.2.4 Leg-hull connection

The connection between the legs and the hull consist of different components, these include guides, fixation systems and jacking systems. The configuration of the leg-hull interface as applied at Aeolus leads to specific stiffness values. Based on earlier research and jack-up FE modelling, the leg-hull connections can be divided in rigid or spring-stiffness connections. It is expected a realistic finite value for the rotational, horizontal and vertical stiffness of the connection would behave similar to a rigid connection. For this research no finite stiffness is considered for the leg/hull connection.

Assuming a rigid connection in vertical, horizontal and rotational direction is in agreement with comparable researches (Cassidy et al. (2004a), Bienen and Cassidy (2006), Cassidy et al. (2004b), Cassidy et al. (2002), Bienen and Cassidy (2006), Bienen and Cassidy (2009), Vlahos et al. (2011), Zhang et al. (2014), Cassidy et al. (2010), Dean et al. (1997), Dean and Metters (2009), Cassidy (2011), Dimitriou (2014), Koole (2015) and Pisanò et al. (2019)).

### 3.2.5 Hull

The flexibility of the hull plays a dominant role in the force redistribution during the preload procedure. To accurately represent the flexibility and to include any asymmetry, the hull is represented by several connected beams. The beam configuration as adopted in the research is depicted in figure 3.10.

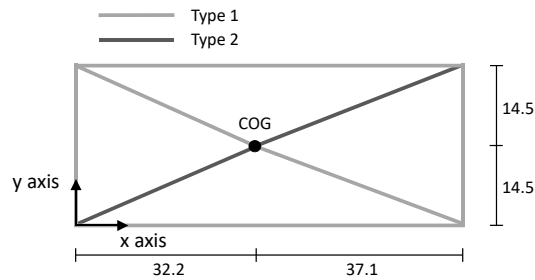


Figure 3.10: Schematic top view of the beam configuration to represent the vessel structure. All dimensions are in m.

The results of the predrive analysis, performed with a detailed FE model of the vessel, are used to assign the stiffness to each beam. In the predrive analysis stress distribution in the hull structure is analysed during extension of one of the two aft legs. This leg is extended up to the level such that the maximum leg load is applied. The maximum leg load is specified as 47.5% of the maximum elevated weight. The influence of environmental loads is not taken into account during the analysis. The predrive analysis consists of three consecutive steps:

1. Standing on 4 legs
2. Preloading port side aft leg with 47.5% of the elevated weight
3. Preloading starboard side aft leg with 47.5% of the elevated weight

When extending the PS or SB aft leg the other legs are supported in vertical direction only. All supports are equipped with rotational springs in x and y direction with a spring stiffness of  $2.9 \times 10^6$  kNm/rad. A schematic overview of step 2 and 3 of the predrive analysis are depicted in figure 3.11 a and 3.11 b. In total four governing load cases (ELLC01-04) of the vessel in elevated condition are analysed, each load case considers a different deck lay out. The COG for all of the load-cases is situated aft of the center of the four legs at  $x = 32.2$ m. The hull is loaded by a single point load at the COG and the self-weight of the beams is equal to zero.

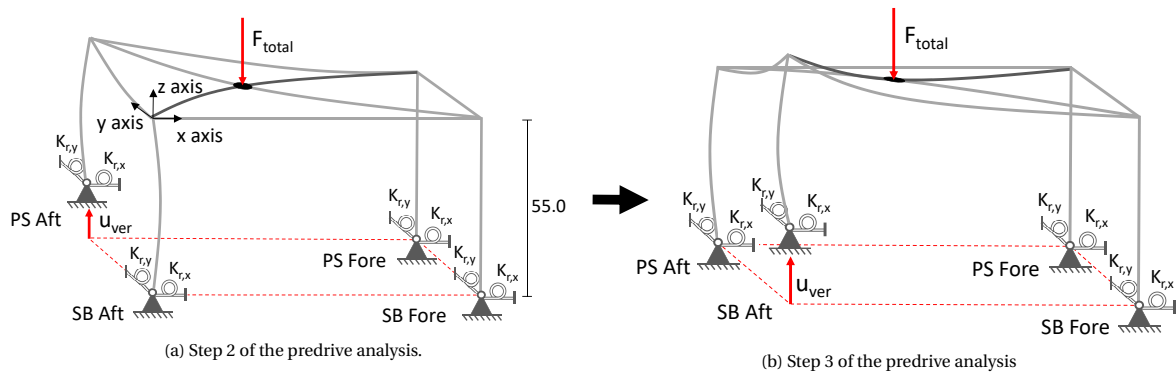


Figure 3.11: Schematisation of two steps of the predrive analysis to determine stiffness of the beams. The beams and legs are rigidly connected and the stiffness of the rotational springs in x and y direction at the supports is  $2.9 \times 10^6$  kNm/rad.

The results of the predrive analysis indicate the leg loads and displacements at the end of each step. These numbers are used to determine the stiffness of the beams for the model used in this research. The stiffness of the beams is adjusted such that the leg loads and displacements in the model coincide with the results from the predrive analysis. This is a simple but effective method to accurately represent the structural behaviour of the hull. The results of the analyses are presented in appendix D and the final stiffness values for the beams are presented in table 3.7.

In the predrive analysis the SB aft leg is displaced more than the PS aft leg to reach a preload value of 47.5% of the total weight. To simulate this asymmetric hull stiffness a lower value for the moment of inertia, and thus stiffness, is specified for the two diagonal beams connecting the SB aft and PS fore leg. A possible cause for the difference in stiffness is the crane structure present near the PS aft leg, resulting in a higher stiffness of the hull in this corner.

The results in appendix D indicate the loads for the active leg pair (PS aft and SB fore in step 2, SB aft and PS fore in step 3) as calculated by the model are similar to the predrive analysis results, the difference is  $\leq 2.73\%$ . The difference between the loads for the passive leg pair are larger, with an average difference of  $\approx 15\%$  and

Table 3.7: Geometrical and mechanical properties of the legs and beams in the model used in this research.

Beam type	Material type	$E$	$\gamma$	$I_2$	$I_3$
[-]	[-]	[kPa]	[kN/m <sup>3</sup> ]	[m <sup>4</sup> ]	[m <sup>4</sup> ]
Leg	Elastic	$210 \cdot 10^6$	0	3.35	3.35
Type 1	Elastic	$210 \cdot 10^6$	0	18	18
Type 2	Elastic	$210 \cdot 10^6$	0	15	15

some outliers up to  $\approx 50\%$ . Since the loads for the passive leg pair are approximately one order of magnitude lower than the loads for the active leg pair, the deviations are of relatively low impact on the overall force distribution in the structure.

### 3.3 FE discretization

The FE discretization is of particular importance in the soil volume as large permanent deformations and displacements occur. The 10-node tetrahedral element type is used for to represent the soil in the 3D analysis. This element provides second order interpolation of displacements and a 4 Gauss integration points. For structural components the 3-node line element, compatible with the 3-noded side of the soil element, and 6 node plate element are used to represent the behaviour of beams and plates respectively.

Local mesh refinement is applied in order to ensure an effective mesh in terms of computational time and costs.

#### 3.3.1 Soil volume

The discretization of the soil volume is based on the calculation of the bearing capacity of the spudcan at 10 m depth. The Mohr-Coulomb soil model is used to exclude interference of pore pressures and serves as a reliable and sufficient basis to start the discretization. The 'Drainage type' *Undrained B* enables simulation of undrained behaviour and the strength is modelled by using the undrained shear strength as input, making it a Tresca theory based soil model. The adopted values for each layer are presented in table 3.8. By using a one-phase model the results of the mesh refinement are comparable to the bearing capacity calculated from the ISO (2016). Note that the OCR value is no input parameter in the Mohr-Coulomb model and clay layer 1 is not subdivided as suggested in section 3.1.1.

The results of the 2D analysis and the ISO analysis are supposed to be similar. The mesh discretization however, is based on the convergence of the solution as predicted by the finite element model in 2D and 3D.

Table 3.8: Calibrated Mohr-Coulomb parameters as used for the FE discretization.

Layer	$\gamma_{unsat}$	$E$	$e_{init}$	$\nu$	$c$	$\phi$	$\psi$	Drainage
[-]	[kN/m <sup>3</sup> ]	[kPa]	[-]	[-]	[kN/m <sup>3</sup> ]	[deg]	[deg]	[-]
Clay 1	16	$25 \cdot 10^4$	0.9	0.3	$9+5.1 \cdot z$	0	0	Undr. B
Clay 2	17	$25 \cdot 10^4$	0.65	0.3	$91+5.2 \cdot (z-17.5)$	0	0	Undr. B
Sand	16	$4 \cdot 10^5 + 2150 \cdot (z-22.7)$	0.5	0.3	0	40	10	Drained

A 2D axisymmetric analysis is performed using PLAXIS 2D (Brinkgreve et al., 2018d). Since 15-node triangle elements are used in the 2D analysis the results are more accurate for the same amount of elements compared to the 3D analysis. The 15-node triangle element provides fourth order interpolation for displacements and the numerical integration involves twelve Gauss points. Compared to the 10-node tetrahedral element the difference in order of interpolation is two. One 15-node triangle element requires four 10-node tetrahedral elements to achieve similar accuracy. The results for the 2D analysis are presented in appendix E. The solution converges to a value of 0.97, as determined using the finest mesh (mesh 4). Mesh number 1 is the coarsest mesh and deviates most from the converged solution, a finer mesh leads to more accurate results.

To reduce computation time and costs in the process of mesh refinement, axisymmetry is used for the FE discretization of the soil volume. Only a quarter of the spudcan and corresponding soil volume is modelled. The soil domain is extending 30 m in both horizontal directions and 40 m in the vertical direction, this size is sufficient to exclude boundary interference. After discretization the domain size is optimized by analysing possible boundary effects. The boundary conditions applied to the model ensure fixity in horizontal direction at the vertical boundaries and fixity in vertical and horizontal direction at the bottom boundary. No groundwater flow boundary conditions are assigned since pore water pressures are not considered by the

Mohr-Coulomb model.

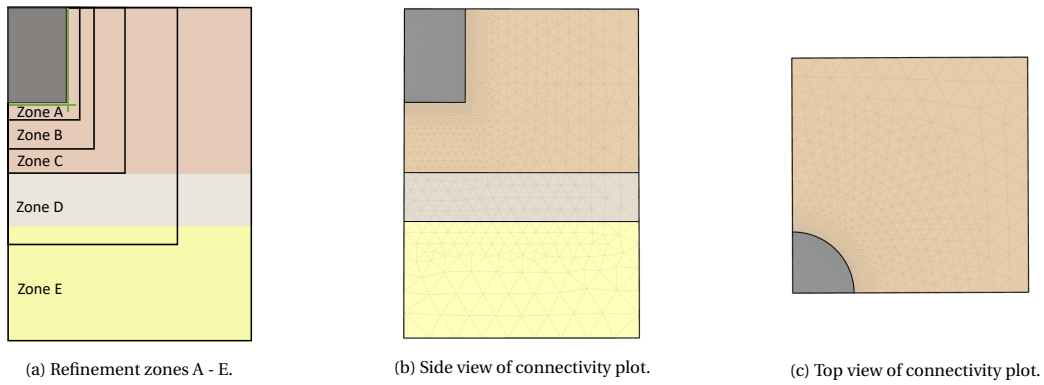


Figure 3.12: Overview of the soil domain used for mesh discretization and mesh refinement.

The domain is divided in five zones as depicted in figure 3.12a. Each zone is represented by an imaginary box within the model and the mesh is refined differently in each zone/box. In total four meshes are generated with the specifications as listed in table 3.9. The mesh is refined at and around the corners of the spudcan and directly below the spudcan, at these positions the largest displacements are expected. During the FE discretization procedure this distribution of refinement is found to be the most effective. A finer mesh extending further below the spudcan generates no improvement on the results. An overview of the mesh is shown in figure 3.12b and 3.12c, the spudcan and leg are shown in grey and the interfaces in green.

Table 3.9: The 3D meshes and specification on the number of elements and nodes and element size.

Mesh no.	No. of elements	No. of nodes	Average element size [m]					Norm. leg load
			Zone A	Zone B	Zone C	Zone D	Zone E	
1	14499	21267	0.5	0.7	1.9	3.1	3.7	1.23
2	69228	79413	0.3	0.5	1.0	2.9	3.7	1.15
3	134672	185367	0.2	0.5	0.5	2.9	3.7	1.12
4	369350	503035	0.15	0.35	0.5	2.9	3.7	1.09

The results of the analysis are depicted in figure 3.13a and 3.13b. The same trend from the 2D analysis is observed in the 3D analysis as a finer mesh converges to a lower bearing capacity. The bearing capacity calculated using 3D mesh number 4 approaches the solution of 2D mesh number 1. The accuracy achieved in the 2D analysis requires the 3D second order elements to be one-fourth of the size of the 2D fourth order elements. The size of the elements in zones B, C, D and E are larger than one-fourth of the higher order 2D elements. It is expected that smaller elements in all zones in the 3D analysis would lead to a result approaching the, more accurate, 2D meshes. The computation time for mesh 3 and 4 is significant, despite the fact that only a quarter of the domain is modelled. A finer mesh increases the computation time and costs. The optimal combination of the computation time and accuracy for the purpose of this research is achieved via mesh number 3.

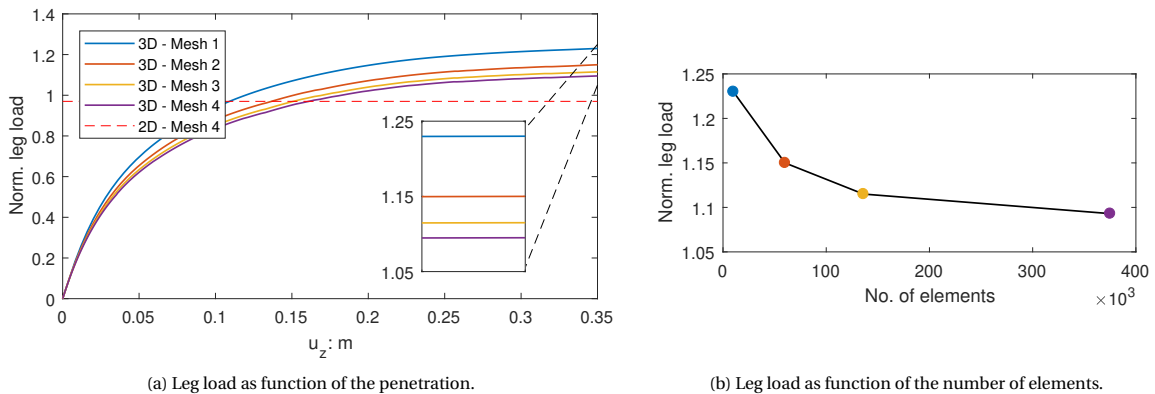


Figure 3.13: Visualization of the results of the 3D mesh discretization.

The rough estimate for the bearing capacity at 10 m depth determined from the ISO (2016) is 0.9 on the scale of the normalized leg load. This value is lower than the converged solution in 2D and 3D. The ISO adopts an ultimate bearing capacity based on undrained failure,  $\phi = 0^\circ$ , since the spudcan represents a circular footing the product  $N_c * s_c$  is taken as 6.0. The Skempton bearing capacity factors are used and the soil properties are specified in table 3.8. The deviation between the ISO based solution and the 2D finite element solution is approximately 7%, the ISO based solution could serve as a lower capacity limit for this specific case.

### 3.3.2 Structural components

The discretization of the structural components requires no investigation. The legs above seabed and hull structure are discretized using 3-node beam elements. This element allows for six degrees of freedom per node and is based on Mindlin's theory for beams (Bathe, 1982) allowing for deflection due to shearing as well as bending. Elements with a size of 3.6 m for the legs and hull structure are used, being the coarsest mesh applicable to this type of element in PLAXIS. This elements size leads to the same results for deformations and forces as for an element size of 0.2 m.

The spudcans and legs below seabed are modelled as rigid bodies. The rigid bodies do not deform and only translate or rotate related to the so-called rigid body reference point.

### 3.4 Total model

The total model after FE discretization is depicted in figure 3.14. The optimal mesh for the soil domain for a single spudcan is determined in the discretization analysis, this mesh is adopted for each spudcan in the total model. The soil domain consists of three different soil layers. The first soil layer consists of clay and is subdivided in three sub-layers adopting a different value for the OCR. The second layer also consists of clay and at the bottom of the domain is a dense sand layer.

The optimal domain dimensions, ensuring no interference of the boundaries, are determined after application of the two-phases SSC and HS-small model in the discretized mesh. The influence of the presence and height of the sand layer is examined by assigning different heights to the layer and evaluating the maximum bearing capacity. The bottom of the sand layer is fully fixed, which implies that the bottom does not deform or displace. The influence of the side boundary is examined with the same approach as the width of the domain is decreased and the capacity is evaluated accordingly. The results indicate a limited influence of the sand layer on the capacity as the differences are small (<2%) varying the layer height between 0 and 20 m. Taking into account the OCR decreases as the spudcan proceeds to penetrate, as described in section 3.1.1, the sand layer is incorporated extending from a depth of 22.7 m to 35 m. The side boundaries do not influence the results using a width  $\geq 25$  m from the leg mid-axis.

The soil volume is fixed in horizontal direction at the vertical boundaries and fixed in horizontal and vertical direction at the bottom boundary. The top boundary is free to translate and rotate in any direction. Groundwater flow boundary conditions are assigned to each of the boundaries, seepage is allowed for the top, bottom and side boundaries. The position of the COG of the structure is positioned 1.5 m aft of the mid-axis of the hull. The diagonal beams, representing part of the hull structure, are connected at this point. The total number of elements and nodes for the total FE model are 391391 and 546692 respectively.

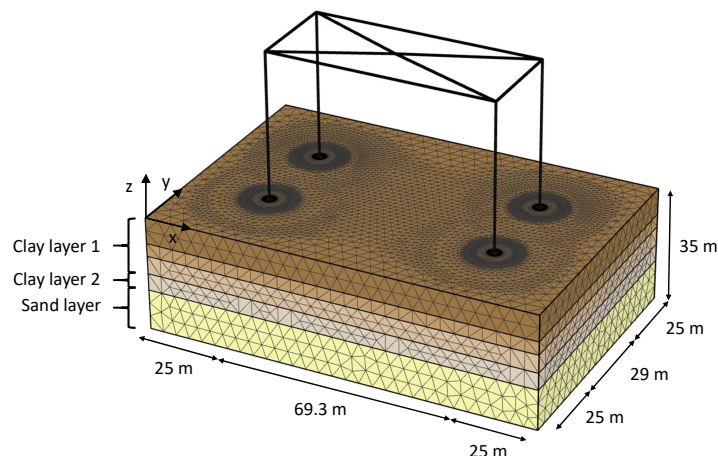


Figure 3.14: 3D FE mesh of the jack-up vessel and soil domain dimensions.

## Simulations

Simulations are performed of the spudcan penetration and the preload procedure. By comparing the results of both type of simulations the influence of the viscous effects and isotach behaviour on the leg load redistribution is analysed. The jacking data is used to verify the results of the FE model created in this research. The application of the alternative preload procedures is investigated and the results are compared to the results of the normal preload procedure. The results are evaluated and argumentation on the choice for the type of procedure is formulated.

### 4.1 Method

To correctly simulate the spudcan installation and preload procedure the development of the OCR distribution over depth and the different phases of the preload procedure are to be identified. Information on the procedure followed during preloading is retrieved from the jacking data from the project site. The data reveals information on the preload target and the possible variation in leg extension rate. But, more importantly, indicates the extent of the influence of viscous effects on the leg load redistribution and the applied preload procedure.

As the spudcan is loaded during the preload procedure, the total vertical stress on the soil increases significantly and, depending on the drainage conditions, the OCR tends to decrease. To what extent the OCR decreases over the depth determines the magnitude of creep strains calculated and incorporated by the constitutive model.

The analyses of the jacking data, the OCR development and the application of the FE procedure are elaborated in the next section. Before conducting simulations of the spudcan penetration and the preload procedure an overview of the different simulation-cases is provided.

#### 4.1.1 Jacking data

The jacking data of the preload procedure at the project site is depicted appendix I. The first figure in the appendix depicts the leg load as function of time and the second figure depicts the spudcan penetration as function of time. The data is used to identify the variation in penetration depth and leg load, the preload target and the number of leg pair load cycles.

Based on the COG positions, specified in appendix D, the highest loads and penetration depths are expected for the SB aft and PS aft. The jacking data indicates a similar trend as the aft spudcans are within a normalized depth range of 1.05 - 1.15 and the forwards spudcans within a depth range of 0.95 - 1.0. A slightly higher target leg preload value for the aft legs than for the forward legs is applied, being respectively 0.88 and 0.95 of the maximum leg load observed in the jacking data.

First the PS aft and SB forward leg are preloaded after which the SB aft and PS forward leg are preloaded. The number of preload cycles can not be determined from the jacking data as the legs are extended several times and the consolidation phases are shorter than 15 minutes. The time covered for each leg pair to be preloaded is approximately 60 minutes, which corresponds to three to four preload cycles.

The grey areas in both figures each comprise a time domain of 25 minutes in which the final preload cycle for one of the leg pairs is executed. The data covered by the grey area is depicted in more detail in the third figure. In these time domains the spudcan penetrations are constant while the loads vary.

#### 4.1.2 FE preload procedure

In this research only the preload procedure of the complete installation procedure is considered. As this is the final part of the total installation procedure only relatively small strains ( $\leq 1.0$  m) may be expected. A small deformation finite element (SDFE) analysis is performed and a wished-in-place (WIP) method is used to conduct the preload stage. The FE preload procedure is subdivided in three phases:

- Phase I - Geostatic stress state
- Phase II - Self-weight installation
- Phase III - Preload cycle of one leg pair (PS aft and SB fwd, SB aft and PS fwd) followed by consolidation of the soil domain.

During the first phase the geostatic stress state within the soil domain, in absence of any structural components and external loads, is calculated. During the installation phase the spudcans are positioned at the predetermined depth, as a WIP method is used the installation effects are neglected. The predetermined depth corresponds to the bearing capacity equal to the leg load reached just before the preload phase starts. This depth and corresponding leg load differs for each individual leg due to the position of the COG, the deck stiffness and interference of the other spudcans. By assuring similar additional penetrations for each leg a flat operating vessel-deck and a similar and comparable soil state below each spudcan is ensured. The final calculation is the preload phase and additional penetration is expected. By alternately extending the two diagonal opposite leg pairs the legs are preloaded up to the preload target. This calculation phase is followed by a consolidation calculation during which the leg extension is stopped. The FE software allows for a consolidation phase during which excess pore pressures dissipate and consolidation and potential viscous effects could result in load redistribution between the leg pairs. The change in permeability during the consolidation calculation is negligible, as shown by the analysis presented in appendix G.

The predetermined depth for each spudcan is based on the expected leg load and the bearing capacity of the soil. The total weight of the vessel is  $28 \cdot 10^3$  ton, by applying a point load at the COG position of the vessel structure the leg load distribution is determined. The leg load redistribution is based on the predrive analysis results. The loads in the aft legs are higher and similar to the jacking data, consequently the aft spudcans are positioned at larger depth than the forward spudcans.

The load at the spudcan tip level indicated by the jacking data represents the effective weight of the vessel taken by the specific leg. In the model the leg loads are specified and monitored in the node-to-node anchors, positioned just above the seabed level. As in the actual situation a certain soil volume is present on top of the spudcan, assuming complete backfill (section 3.2.1), this load portion is to be added in the model. The total load at the spudcan tip level is the sum of the effective leg load, the soil backfill effective weight, and the uplift force of the cylinder (representing the spudcan and soil volume). Figure 4.1 depicts a schematisation of these loads. The values correspond to a normalized spudcan depth of 1.2 and 1.1 for the aft and forward legs respectively. The target preload values, 0.95 for the aft legs and 0.88 for the forwards legs, correspond to the effective normalized leg load.

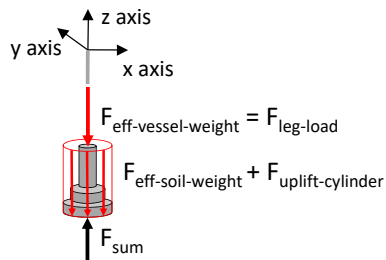


Figure 4.1: Visualisation of the loads.

#### 4.1.3 OCR development

The OCR distribution for the initial situation and the situation where the spudcan is loaded are depicted in figure 4.2. Consolidation is allowed for a specific amount of days and the OCR distribution develops correspondingly. In the FE model a different OCR is assigned to each layer causing a layered distribution, in reality the OCR distribution over depth is more gradual. The initial OCR at a depth of 8-12 m is 6 and directly below the spudcan decreases to a value of 3.5 after 1 day of consolidation, for the depth range 12-17.5 m the OCR decreases from 5 to a value of 2.5. For clay layer 2 the initial OCR is 4 and likewise decreases to a value of 2.5. As the jack-up vessel is jacked for a maximum duration of one day, corresponding the installation cycle time per wind turbine, the OCR distribution for this consolidation period reflects the most accurate stress situation within the soil domain. For a longer consolidation duration the OCR decreases further as the excess pore pressures continue to dissipate and the effective vertical stresses increase. The potential change of the OCR due to remoulding of the soil below the spudcan, during penetration, is neglected.

The distribution of the OCR in the top layer is relatively inhomogeneous close to the spudcan cylinder. This is probably caused by the soil flowing around the corner and along the vertical cylinder boundary. The brown area in the figure depicting the OCR distribution after 100 days indicates an OCR value higher than 7.0.

The minimum value for the OCR after one day of consolidation is 2.5. The figures illustrating the influence of the strain rate on the soil strength, figure 3.7a and 3.7b, indicate that the model does not show any viscous effects for an  $OCR > 2$ .

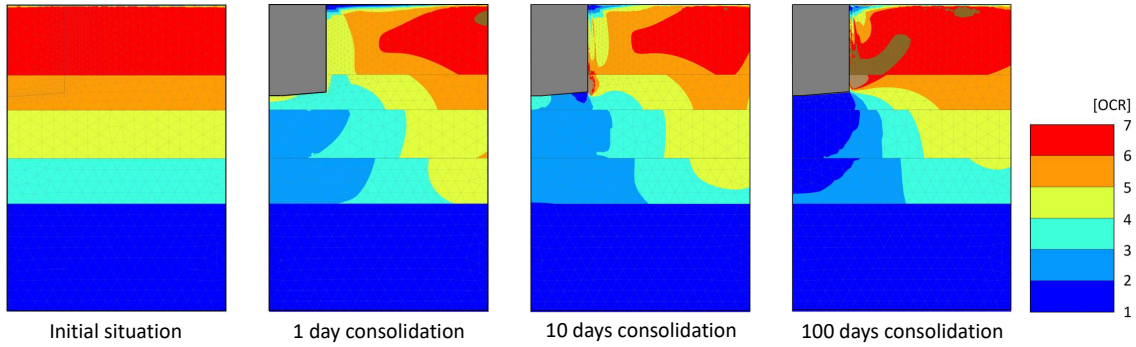


Figure 4.2: OCR profile within the soil domain before and after loading, after 1, 10 and 100 days of consolidation.

#### 4.1.4 Simulations specification

Two types of simulations are performed, the single spudcan penetration and the total model preload procedure. For each type of simulation six case-calculations are performed, allowing to investigate the influence of different parameters and procedures on the extent of the viscous effects and leg load redistribution. In case 1 the OCR values following from the analysis from section 4.1.3 are used and the initial spudcan depths are varied. In case 2 the distribution of the OCR is varied, case 3 considers a lower spudcan penetration rate and in case 4 a smaller permeability of the clay layers is adopted. In case 5 and 6 the type of preload procedure is varied.

In table 4.1 the value range or variation for each parameter are specified for the six independent cases.

Table 4.1: The six simulation cases, each addressing a different model parameter.

Case	Norm. initial depth	OCR	Permeability	Preload procedure	Norm. penetration rate
[-]	[-]	[-]	[m/day]	[-]	[-]
1	0.9 - 1.2	2.5 - 4.0	$10^{-5}$	Normal	0.80
2	1.1 - 1.2	1.4	$10^{-5}$	Normal	0.80
3	1.1 - 1.2	1.4	$10^{-5}$	Normal	0.13
4	1.1 - 1.2	1.4	$10^{-3}$	Normal	0.80
5	1.1 - 1.2	1.4	$10^{-5}$	Overshooting	0.80
6	1.1 - 1.2	1.4	$10^{-5}$	Alternative	0.80

## 4.2 Results

The results for the six cases for both types of simulations are presented in the following section. In the single spudcan penetration simulation interference of the structure and other spudcans is excluded. Figure 4.6a depicts a schematic overview of the single spudcan penetration. A fixed-end anchor is attached to the mid-axis of the spudcan. The anchor is pre-stressed up to the preload target value, during the simulation the anchor extends and the spudcan is pushed into the soil. The simulation provides insight in the pore pressure distribution and the deformations in the soil domain and the extent of the influence of viscous effects without the mechanism of leg load redistribution.

The complete preload procedure is performed with the total FE model, including all spudcans and the connecting structure. The simulation of the preload procedure provides insight in the quantitative effects of the soil processes and the applied preload procedure. In the figures depicting the results of the preload procedure additional dashed lines are presented, these additional lines are also depicted in figure 4.3. The normalized preload target for the aft and forward legs, being 0.95 and 0.88, are depicted as two horizontal dashed black lines. The preload criterion as adopted in this research is a leg load reduction of 400 ton / 15 min and in the graphs indicated as a horizontal dashed red line.

Further, the preload procedure is divided in different stages. The vertical dashed lines indicate the start of the next stage in the procedure and the stage-number is indicated at the top of the graph. A stage indicates either a preload cycle or the initial loading of the active leg pair up till the preload target. During the final stage the initial leg load distribution is re-established. The total number of stages differs for each case and depends on the number of preload cycles performed.

In appendix J additional results of the simulations are presented, including the ship corner displacements, the absolute leg extension and the displacement and deformations of the complete hull structure.

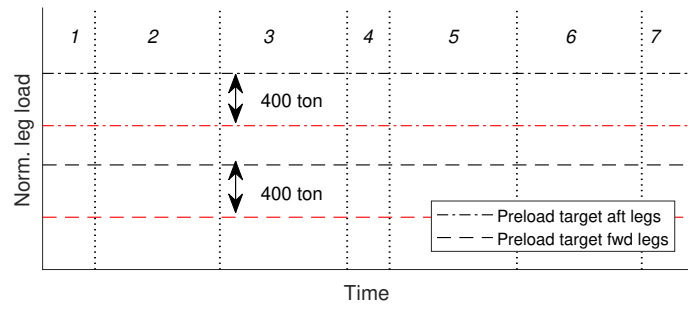


Figure 4.3: Clarification on additional lines in results of the preload procedure.

4.2.1 Case 1

Figure 4.4 depicts the total penetration as function of the leg load. The normalized initial depth of the spudcan is varied in the range 0.9 - 1.2 . For a larger initial spudcan depth the total settlement, after applying the preload target, is smaller. The settlement at the normalized preload value of 0.95 for the spudcan at a normalized depth of 0.9 is 250% higher than for a normalized depth of 1.2. The results for different penetration rates are identical and the influence of viscous effects is negligible.

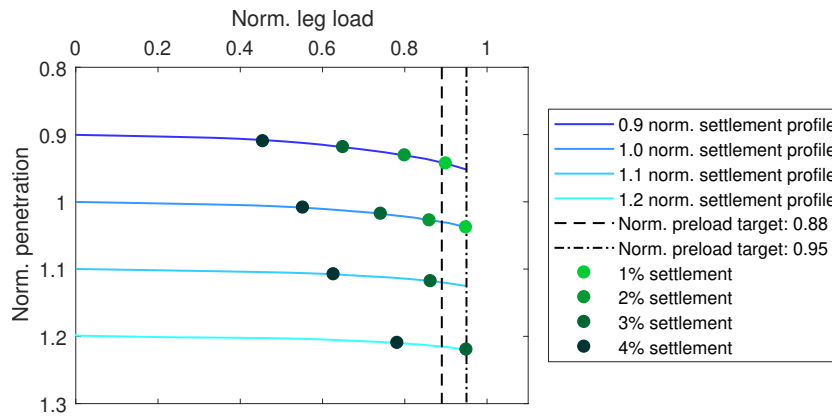


Figure 4.4: Single spudcan penetration, case 1.

The spudcan penetration and leg load as function of time, for a normalized initial spudcan depth of 1.1, are depicted in figure 4.5b and 4.5a respectively. The additional penetration during consolidation is limited to only 0.2% of the total penetration and the leg load reduces with 1.4%. The initial OCR values of the different layers are within the range 2.5 - 4.0. Based on the results of the model indicating the effect of the OCR on the creep rate and total amount of creep, as presented in section 3.1.1, the viscous effects are negligible in this range of the OCR. Consequently, in case 1 the additional spudcan penetration and leg load reduction during the consolidation calculation phase are solely caused by consolidation.

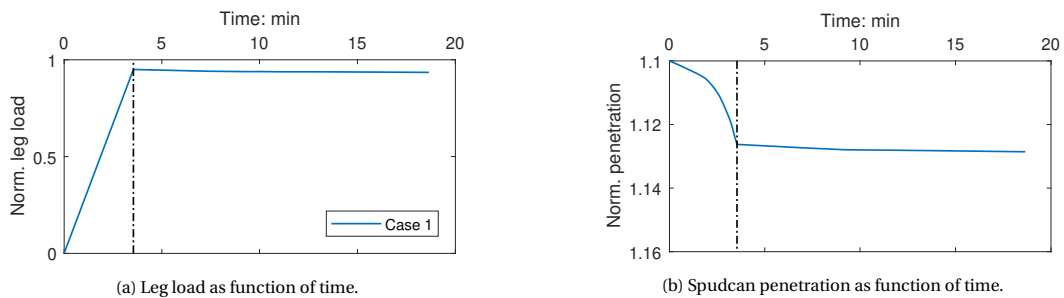


Figure 4.5: Single spudcan penetration with a normalized initial depth of 1.1.

Figure 4.6b and 4.6d respectively depict the total displacements and excess pore pressures within the soil domain after spudcan penetration. The width of the soil domain from the mid-axis of the spudcan is 25 m. The total displacements are high directly below and around the spudcan and decrease with an increasing distance from the spudcan. The results indicate soil displacements and deformations within the soil domain up to 15 m from the spudcan mid-axis. The excess pore pressures show a similar profile; the highest pressures

are observed directly below the spudcan. The excess pore pressures decrease to zero at approximately 20 m from the mid-axis of the spudcan.

The distribution of the plastic points is depicted in figure 4.6b and provides insight in the plastic state of the different soil layers. A failure point indicates that the stresses are located on the failure surface, a hardening point represents a point on the shear hardening envelope and a cap+hardening point indicates a point that is on the shear hardening and cap hardening envelope. The latter two type of plastic points are only possible to occur in the soil represented by the HS-small in this model. As indicated by the plastic points the soil below and around the spudcans fails, the failure zone extends to the depth of the sand layer. Within the sand layer both hardening and cap+hardening points are present, hardening occurs for the complete sand layer.

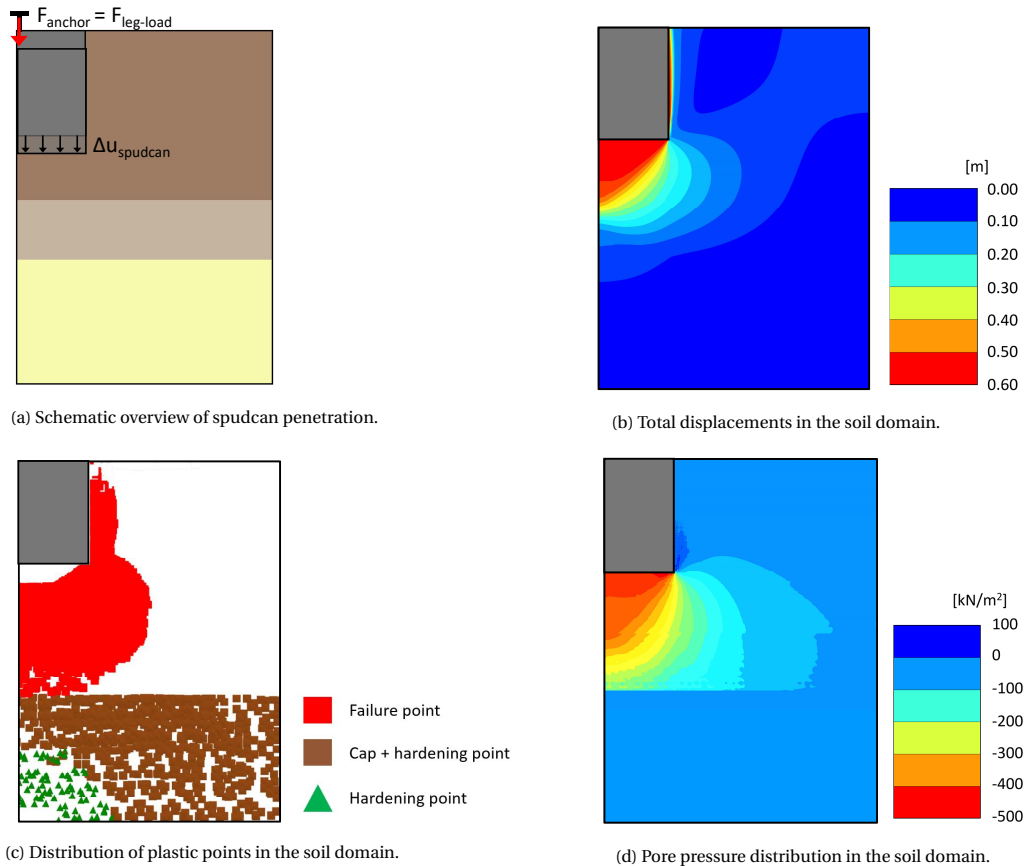


Figure 4.6: Visualization of the results of a single spudcan penetration in a cross section of the soil domain.

Based on the results of the single spudcan simulations it is expected the additional penetration for the legs at a normalized initial depth within the range 0.9-1.2 is limited to 4% of the total penetration. Figure 4.7a depicts the leg spudcan settlements as a function of leg load during the preload procedure with a normalized spudcan depth of 0.9 and 1.0 for the forward and aft legs respectively.

The settlement of the spudcans of the active leg pair is more than 15% of the total penetration and yet the preload target is not reached. The red signs in the figure indicate failure of the soil. Apparently penetration of a spudcan does influence the penetration of an adjacent spudcan. Figure 4.7b depicts the spudcan settlement as function of the leg load with a normalized initial spudcan depth of 1.1 and 1.2 for the forward and aft spudcans respectively. The preload target is reached at a normalized penetration depth of 1.14 for the forward legs and 1.25 for the aft legs.

The influence of the two aft spudcans, with a normalized initial depth of 1.2, is visualized in figure 4.8. The figures depict a cross section of the soil domain with the total soil displacements and plastic points before and after the first preload cycle. The distribution of the total soil displacements and plastic points within the soil domain both are not symmetric, indicating interference of the adjacent spudcan. The plastic points in figure 4.8d indicate the stresses in the soil are on the failure surface and are extending to two times the spudcan diameter from the leg mid-axis. The distribution of failure points within the soil domain during single spudcan penetration, as depicted in figure 4.6b, is limited to only one time the spudcan diameter from

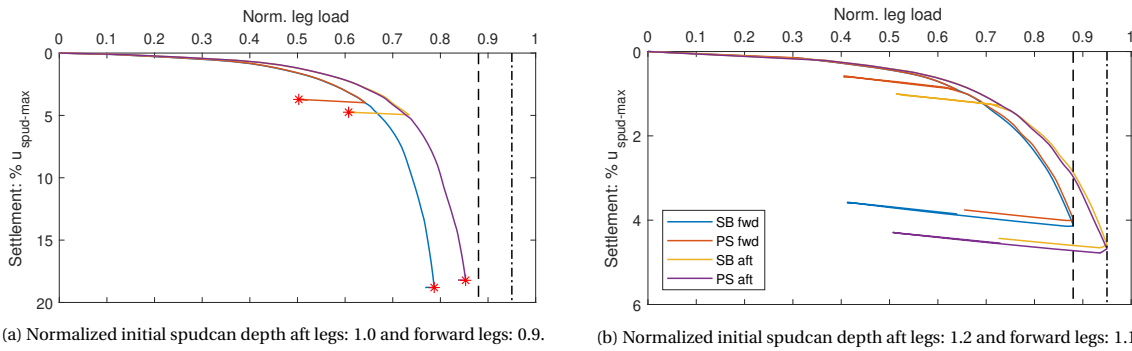


Figure 4.7: Preloading procedure with different initial spudcan depths.

the leg mid-axis. The reciprocal influence of the forward spudcans and of the aft spudcans emphasizes the importance of one model comprising all spudcans in the same 3D soil domain.

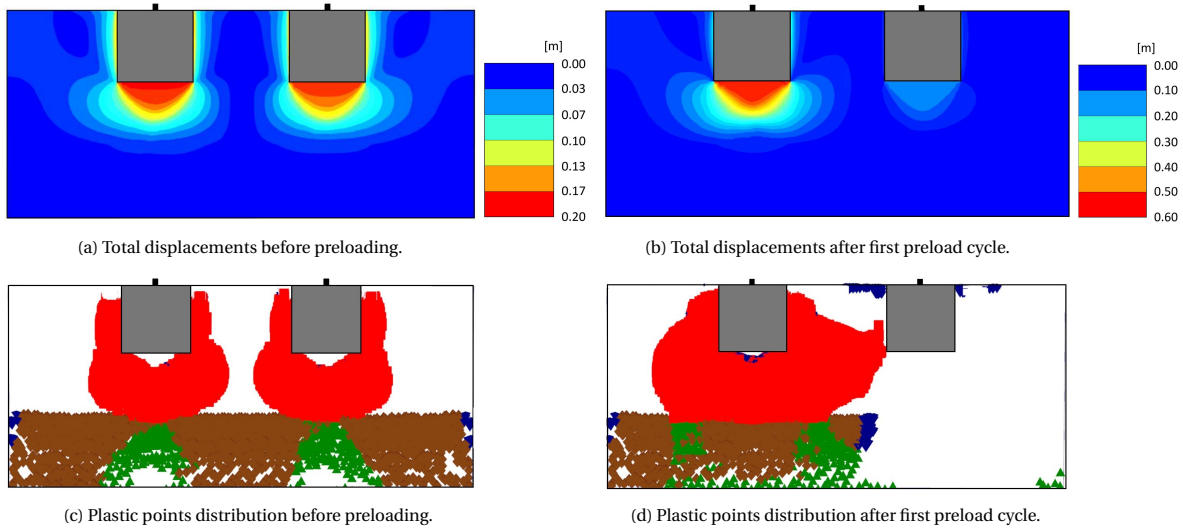


Figure 4.8: Visualization of the influence of the two forward or aft adjacent spudcans.

Figure 4.9a and 4.9b respectively depict the leg load and spudcan penetration as function of time. The black and red dashed lines in the figure 4.9a represent the preload target and the preload criterion respectively. The leg load reduction during the consolidation phase is limited to 1.3% for both the aft and forward legs. This leg load reduction is similar to the value calculated for the single spudcan and is solely caused by consolidation of the soil. The leg load reduction is well below the preload criterion of 400 ton / 15 min and one preload cycle per leg pair suffices to meet the preload criterion.

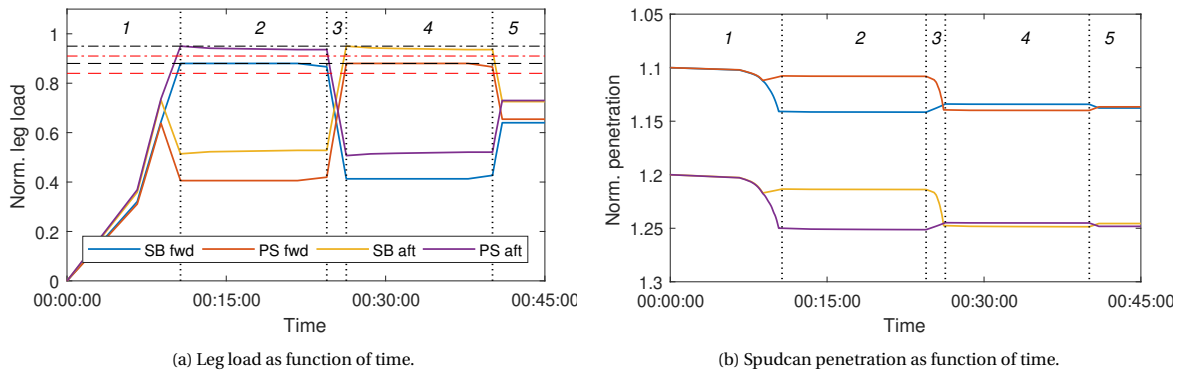


Figure 4.9: Preload procedure, case 1. The normalized initial spudcan depth is 1.1 and 1.2 for the forward and aft spudcans respectively.

The displacements of the ship corners during the procedure vary in a very limited range. The ship corner dis-

placement is calculated by subtracting the leg penetration distance from the total leg extension. At the end of the procedure the ship is slightly tilted aft as the forward corners are displaced slightly more upwards relative to the aft corners, as depicted in figure J.3e. This is a consequence of the choice for the initial spudcan depth, as the penetration during installation and preloading changes by varying the initial depth of the spudcans.

**4.2.2 Case 2**

In case 2 the OCR is decreased to a value of 1.4 for all clay layers. The results for the single spudcan penetration, depicted in figure 4.10b, indicate a larger spudcan penetration in case 2 compared to case 1. During the consolidation phase the additional penetration in case 2 is 0.6% of the total spudcan penetration, which is equal to three times the penetration as calculated in case 1. The leg load as function of time is depicted in figure 4.10a, the load reduces with 3.6% which is considerably more than in case 1. The difference between both cases is induced by the viscous effects of the soil as introduced in case 2 by adopting lower values for the OCR. The additional viscous resistance, present during penetration, diminishes when penetration is stopped and causes the leg load to reduce. To incorporate viscous effects in the model, the OCR distribution adopted in case 2 is also adopted in cases 3, 4, 5 and 6.

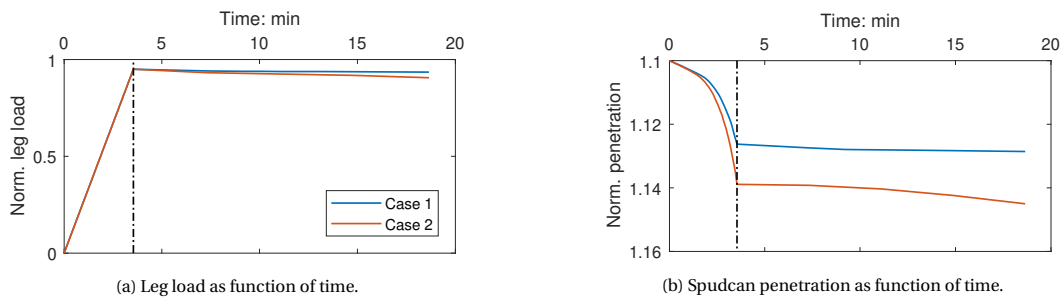


Figure 4.10: Single spudcan penetration, case 1 and 2.

The additional spudcan penetration during the preload procedure in case 2 is 6% and 7% of the total penetration for the forward and aft legs respectively, as depicted in figure 4.11b. The additional penetration for all legs is approximately 30% larger than in case 1. The leg load reduces with approximately 6% during the first preload cycle as depicted in figure 4.11a. This reduction is considerably more than the reduction of 3.6% calculated in the simulation with a single spudcan. The difference between both values is initiated by the isotach behaviour of the clay which is induced by the viscous effects.

The isotach behaviour of the clay results in a higher stress relaxation and creep rate for the active leg pair compared to the passive leg pair. The strength of the soil surrounding the active leg pair is fully mobilized as the spudcans proceed to penetrate. Since the relaxation and creep rate are dependent on the distance from the failure surface, rapid stress relaxation is observed for the active leg pair relative to the passive leg pair. The mechanisms initiates a load redistribution from the active leg pair to the passive leg pair.

To suffice the preload criterion multiple preload cycles for each leg pair are required. The leg load reduction during the second preload cycle is 5%, this is 17% less compared to the first cycle. However, the preload criterion is not met and multiple preload cycles are required. The difference between the load reduction of the two leg pairs is negligible.

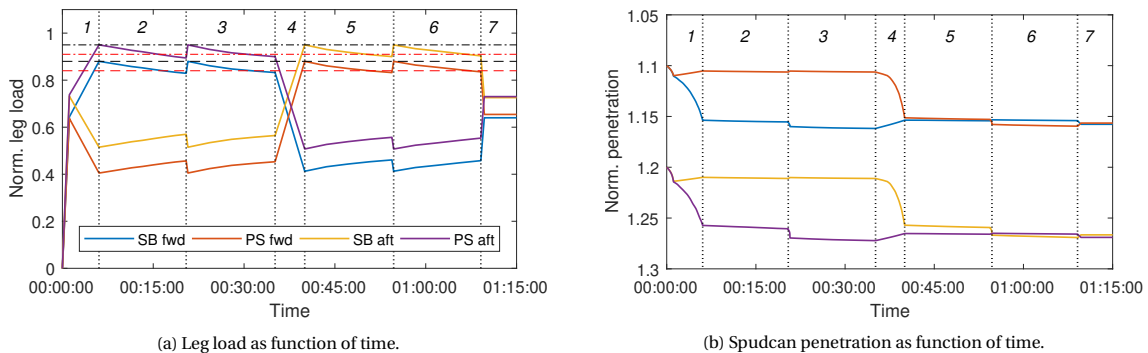


Figure 4.11: Preload procedure, case 2.

**4.2.3 Case 3**

In case 3 the normalized spudcan penetration rate is decreased from 0.8 to 0.13. Since the leg extension mechanism is force-controlled the penetration rate during the simulation is not perfectly constant. The exact penetration rate can be determined from the tangent line to the graph indicating the penetration as function of time. Figure 4.12a and 4.12b respectively depict the leg load and spudcan penetration depth as function of time for the single spudcan simulation. The spudcan penetration is larger in case 3 compared to case 2. However, the additional penetration and leg load reduction during the consolidation phase are lower. The resistance of the soil increases as the penetration rate is higher, caused by the additional viscous resistance. Consequently, the spudcan penetration during the initial loading phase is larger when adopting a lower penetration rate. During the consolidation phase however, the additional viscous resistance diminishes and larger settlements are observed for the case adopting a higher penetration rate. The total penetration after the consolidation phase is similar for both cases.

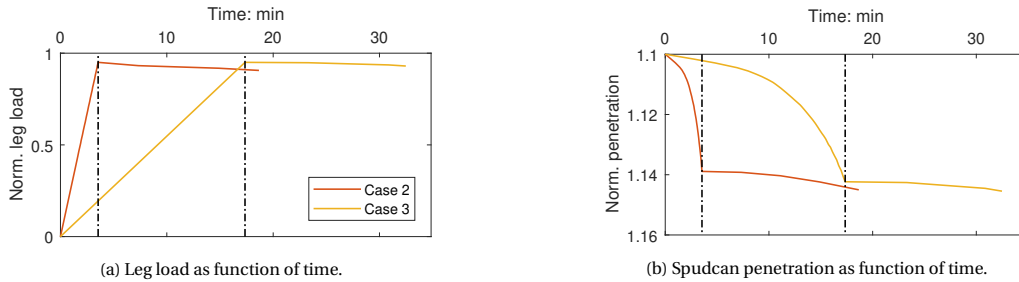


Figure 4.12: Single pudcan penetration, case 2 and 3.

Also for the simulation of the preload procedure the lower penetration rate results in a larger spudcan penetration. After the first preload phase the spudcan penetration is approximately 10% larger in case 3 than in case 2. The leg load reduction during the first preload cycle however, is 4.4% and significantly lower than the load reduction of 6% in case 2. The leg load reduction decreases with approximately 25% compared to a normalized penetration rate of 0.8, though a second preload cycle is required to meet the preload criterion. During the consolidation phase of the second preload cycle the leg load reduces with 3% and the preload criterion is met.

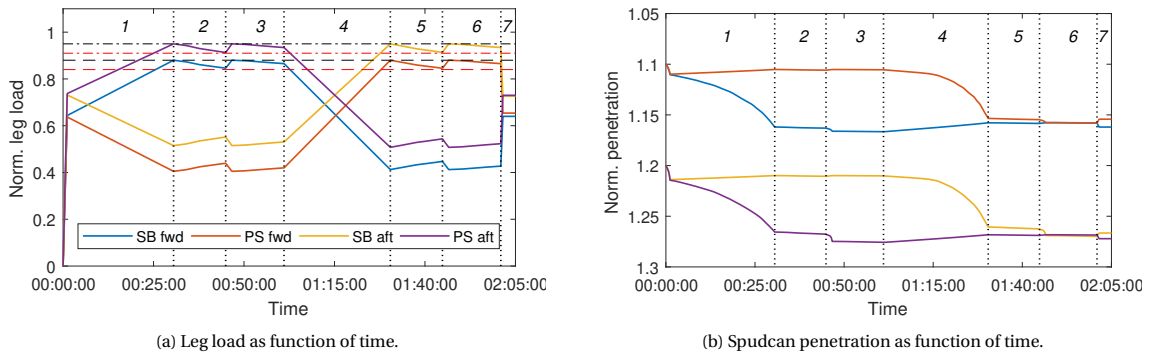


Figure 4.13: Preload procedure, case 3.

**4.2.4 Case 4**

The permeability of the clay layer is increased from  $10^{-5}$  to  $10^{-3}$  m/day in case 4. During the loading phase of the single spudcan simulation the leg load and penetration are similar to case 2, as depicted in figure 4.14a and 4.14b. The results indicate that during the consolidation phase the additional penetration and the leg load reduction are larger in case 4. As the permeability is significantly increased a higher degree of consolidation is reached within a similar period of time. Consequently, the rate of soil settlement and leg load reduction is larger. For the simulation of the single spudcan penetration in case 4 the leg load reduction is 8% and the additional spudcan penetration is 1% of the total spudcan penetration, this is respectively 120% and 70% more than in case 2.

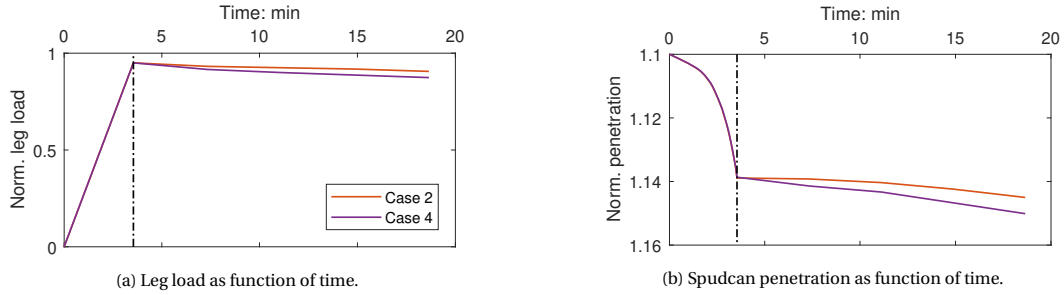


Figure 4.14: Single spudcan penetration case 2 and 4.

Also for the simulation of the preload procedure the additional penetration and leg load reduction during consolidation are larger. The load reduction in the first preload cycle is approximately 8.4% and in the second preload cycle 7%. The preload criterion is not met after two preload cycles and multiple cycles are required. The increase in spudcan penetration over time during the preload cycles in case 4 follows a more gradual path relative to case 2. The penetration continues during the consolidation phase and a smaller step of increase of the penetration at the start of the second preload cycle is observed. Further, at the end of the preload procedure in case 4 the penetration of the SB forward and PS aft leg are higher compared to the adjacent forward or aft leg. In case 2 this difference in penetration at the end of the procedure is negligible.

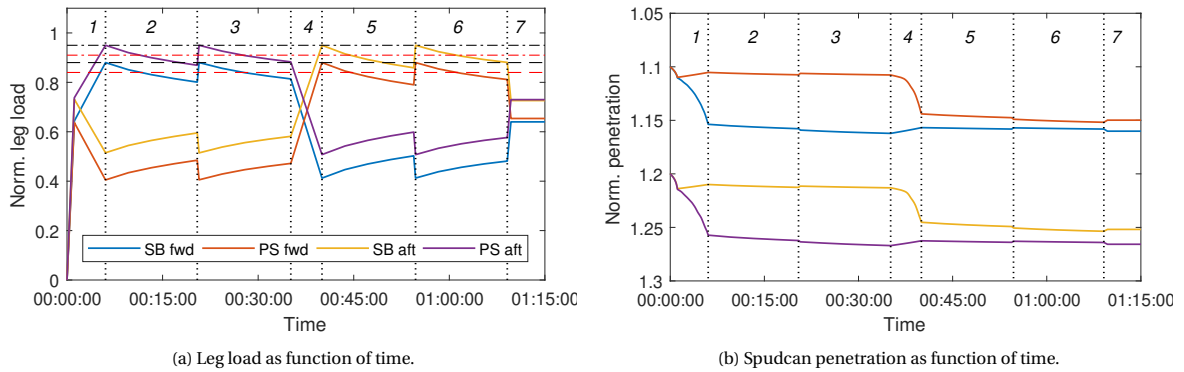


Figure 4.15: Preload procedure, case 4.

**4.2.5 Case 5**

The overshooting procedure, proposed by Cathie et al. (2017), is developed in an attempt to improve the preload duration. During the procedure the preload target is overshoot to bring the spudcan to the depth, which would have been reached by the creep-like additional penetration under the normal preload procedure. Once the overshoot preload target is reached the leg load is actively reduced to the normal preload target before starting the consolidation phase. With this procedure it is likely that the preload can be sustained without additional penetration.

The procedure adopted in this research is slightly different: the leg load is *not* actively reduced to the normal preload target *before* starting the consolidation phase. The consolidation phase is started and from the moment the leg load reduces from the overshoot preload target to the normal preload target, consolidation is continued for 15 minutes.

The value of the normalized preload target in case 5 is increased to a value of 1.0 and 0.95 for the aft and forward legs respectively, 5% larger than the initial preload target. As a larger load is applied the spudcan penetrates further, as depicted in figure 4.16b, and causing the absolute spudcan penetration rate to be slightly higher than in case 2. The additional spudcan penetration during the consolidation phase for case 5 shows a linear increase. The leg load reduction is similar for both cases, as depicted in figure 4.16a.

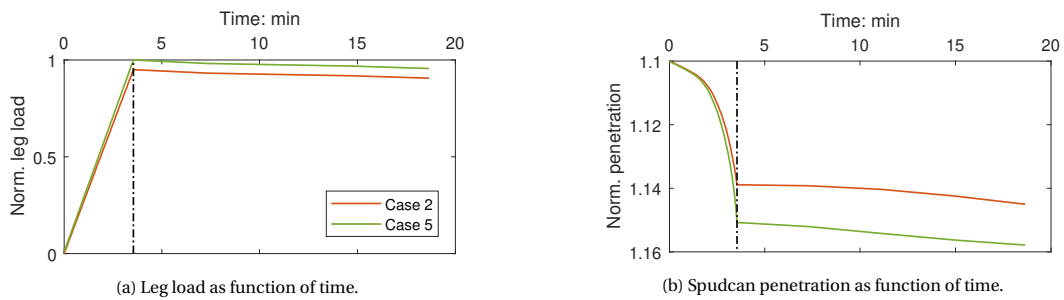


Figure 4.16: Single spudcan penetration, case 2 and 5.

The results of the preload procedure are depicted in figure 4.17a and 4.17b. The preload criterion is met during the first preload cycle as the leg load reduces with only 8.4% during the complete consolidation phase. As the preload target is overshoot with 5%, the leg load reduction relative to the normal preload target is only 3.4%. Compared to the normal procedure, the overshooting procedure is effective in reducing the preload cycles to meet the preload criterion.

As the leg penetrations are larger during the overshooting procedure compared to the normal procedure, slightly more time is required to reach this additional penetration depth. In combination with the extended consolidation phase, one preload cycle takes considerably more time during the overshooting procedure as adopted and executed in this research.

When adopting the exact same overshooting procedure proposed by Cathie et al. (2017), the duration of one preload cycle is similar to the duration of one preload cycle of the normal preload procedure. This procedure is expected to be effective in reducing both the required number of preload cycles and the preload duration.

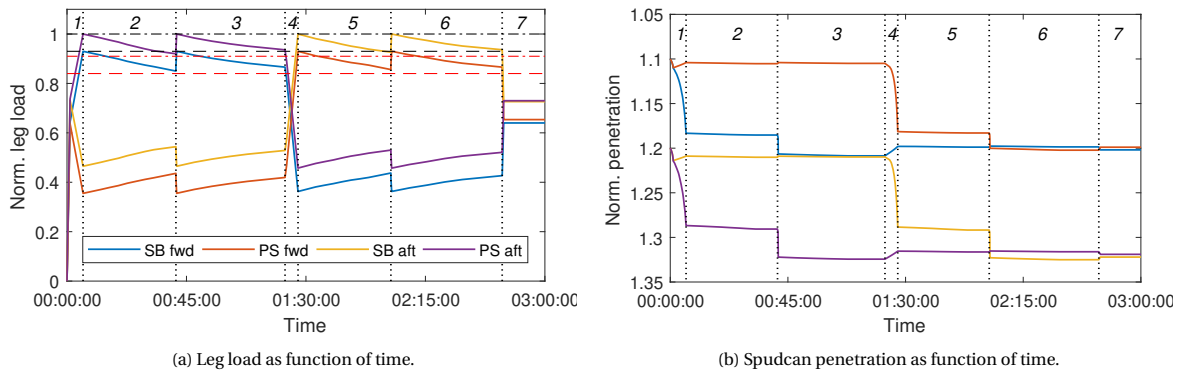


Figure 4.17: Preload procedure, case 5.

**4.2.6 Case 6**

The preload procedure consists of a consolidation phase during which the leg load development, leg load reduction, and additional penetration are monitored. A possible variation, which is regularly performed in practice, is maintaining the leg load at the preload target during the 'first' consolidation phase. The legs are continuously extended to effectuate a constant leg load. During the 'second' consolidation phase the legs are not extended and leg load redistribution is allowed to occur.

The leg load and spudcan penetration over time are depicted in figure 4.18a and 4.18b respectively. As the preload target is kept constant during the consolidation phase in all cases for the single spudcan simulation, the spudcan penetration is similar for case 2 and 6. The spudcan penetration for case 6 continues for the 'second' consolidation phase, the results indicate a decreasing rate of spudcan penetration as the graph tends to flatten out.

The total leg load reduction in case 6 is slightly smaller than in case 2. During the first 15 minutes the preload target is maintained after which the leg load reduction starts. During the 'second' consolidation phase in case 6 the leg load reduction is smaller than the leg load reduction during the 'first' consolidation phase in case 2.

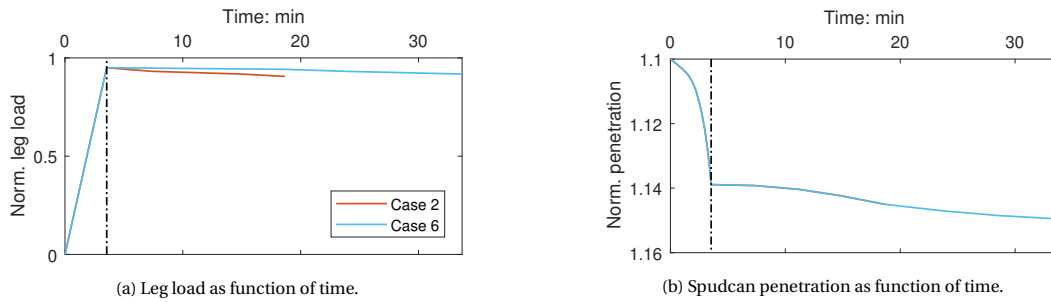


Figure 4.18: Single spudcan penetration, case 1 and 6.

Figure 4.19a and 4.19b depict the leg load and penetration over time during the preload procedure. The results indicate that the penetration of the active leg pair gradually increases and the preload target is maintained.

The leg load shows a linear decrease during the 'second' consolidation phase, the total load reduction at the end of this phase is 4.6%. This reduction is slightly lower compared to the reduction reached during the second preload cycle in case 2. Although the improvement is small and a second preload cycle is required, the procedure adopted in this case appears to be an effective method to decrease the leg load reduction compared to the normal preload procedure.

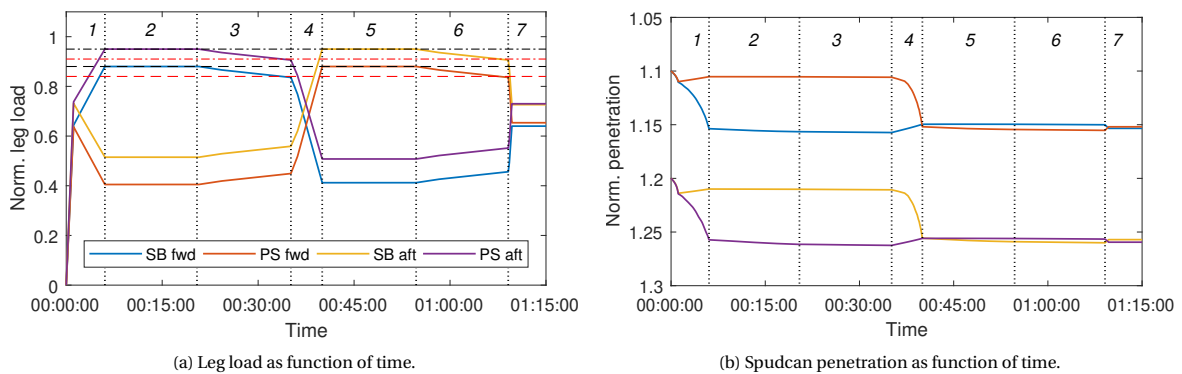


Figure 4.19: Preload procedure, case 6.

#### 4.2.7 Comparison jacking data

Figure 4.20 and 4.21 respectively depict the leg load and spudcan penetration as a function of time from the jacking data and FE model. The dashed coloured lines represent the jacking data and the solid lines the model results. The aft and forward legs are depicted in separate figures.

According to the jacking data the total preload procedure takes approximately two hours, the duration of preloading one leg pair is one hour. The number of preload cycles can not be determined from the jacking data as the legs are continuously extended. One consolidation phase is performed at the end of preloading each leg pair and this phase is ended after approximately 25 minutes. This specific preload strategy is simulated with the FE model, one preload cycle per leg pair is performed and this cycle is followed by a consolidation phase of 25 minutes.

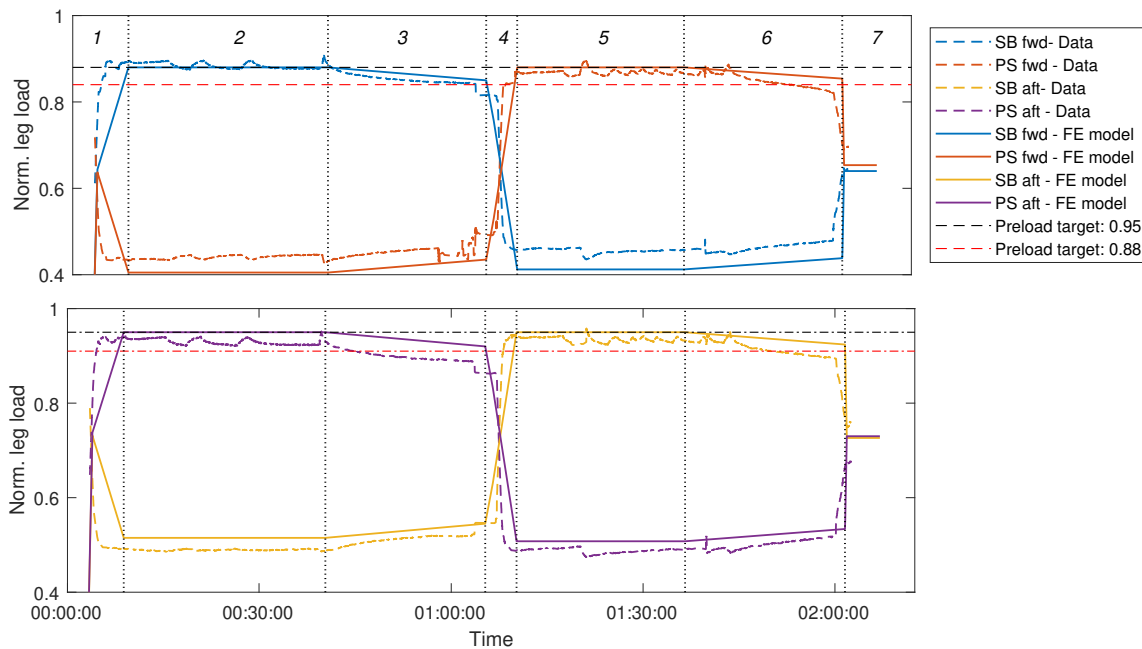


Figure 4.20: Leg load as function of time; jacking data and FE model results.

By continuously extending the legs, the load on the active leg pair is maintained at the target preload. The total leg load reduction during the only consolidation phase is equal to 6% for both the forward and aft legs. During the first 5 minutes of the consolidation phase (stage 3 and 6) the leg load reduces with 50% of the total load reduction. The load reduction flattens out in the final part of the consolidation phase; the load reduction in the final 10 minutes is limited to 10% only.

In the FE model calculations the leg load reduction during the total consolidation phase is equal to 3.2% of the total leg load. The preload criterion is met as the leg load reduces with only 2% in the first 15 minutes. The leg load reduction during the consolidation phase for the 'second' (stage 6) leg pair is 2.6% and slightly lower than the load reduction for the 'first' leg pair (stage 3).

The model calculates a linear reduction in leg load during the consolidation phase. The jacking data indicates rapid load reduction in the first part of the consolidation phase. In the FE model the time-steps for the fully implicit scheme of integration, used for the consolidation phase, are relatively large and an average of four time-steps is adopted to complete the consolidation phase. The large time-steps cause the leg load reduction to deviate from the leg load reduction of the jacking data.

The load reduction for the active leg pair causes a load increase for the passive leg pair. The leg load for the passive leg pair in the jacking data however, is relatively constant and the load increase is smaller than the decrease for the active leg pair. This deviation is also seen in the total load which is equal to the sum of all four leg loads. The total load is expected to be constant over time, however the profile follows a similar path as the load advancement of the active leg pair. This disparity is presumably caused by measurement errors or inaccuracy. The leg load reduction and increase of respectively the active leg pair and passive leg pair calculated by the model are identical.

According to the jacking data the normalized spudcan penetration after the preload procedure is approximately 1.0 and 1.1 for the forward and aft legs respectively. During preloading the active leg pair is continu-

ously extended to maintain the leg load at the preload target. The penetration of the passive leg pair remains constant. At the moment preloading is switched to the other leg pair (stage 4), the penetration of the 'new' passive leg pair decreases and the penetration of the 'new' active leg pair increases.

The FE model calculates that the normalized total penetration at the end of the preload procedure is approximately 1.15 and 1.25 for the forward and aft legs respectively, being 15% larger than observed from the jacking data. The spudcan penetration profile calculated by the model during the complete procedure however, matches with the profile of the jacking data. The trend of spudcan penetration increase and decrease at the moment preloading is switched to the other leg pair, is captured rather well by the model.

The additional penetration is continuous throughout the time domain according to the jacking data. The additional spudcan penetration calculated by the FE model indicates most of the additional penetration occurs during the second half of stage 2.

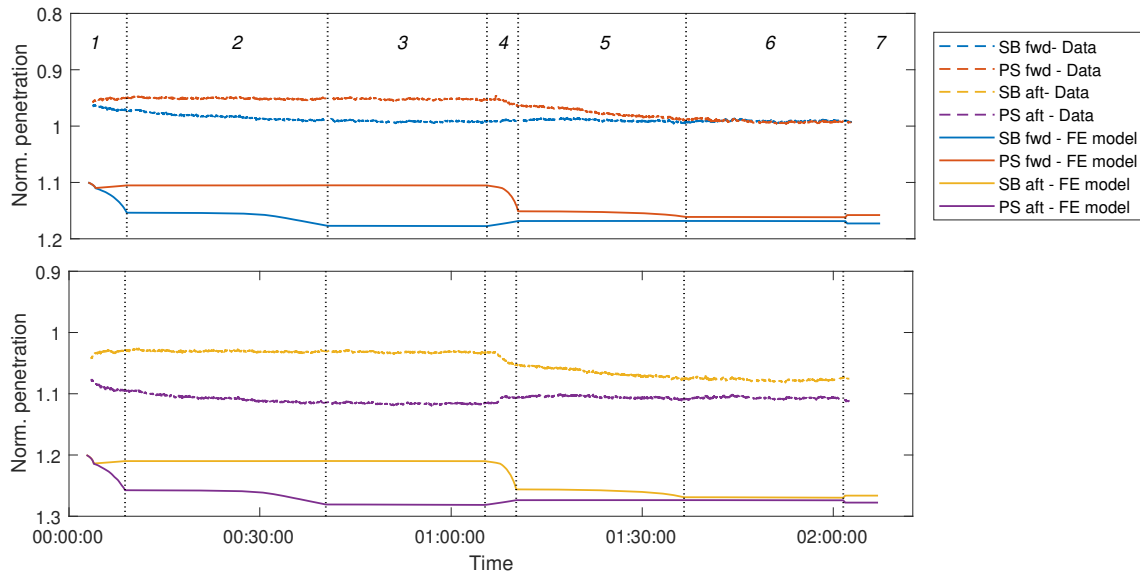


Figure 4.21: Spudcan penetration as function of time, jacking data and FE model results plotted in one graph.

By performing the exact same preload procedure in the model as the jacking data, the preload criterion is met. The leg load reduction during the consolidation phase is smaller than indicated by the jacking data. The model results indicate a shorter preload duration would suffice to satisfy the preload criterion. An iterative process is required to identify when the preload criterion is satisfied and to assess the minimum preload duration according to the model.

In appendix J.3 an alternative simulation of the preload procedure with the model is presented. The preload criterion is met during the fourth preload cycle for the 'first' leg pair and the third preload cycle for the 'second' leg pair. The total duration of this preload procedure is larger than for the procedure as depicted in figure 4.20 and 4.21.

### 4.3 Discussion

Two types of simulations are performed in this research; (1) the simulation of the penetration of a single spudcan into the soil domain and (2) the simulation of the complete preload procedure for the jack-up vessel Aeolus. During the simulation of the single spudcan penetration any interference of adjacent spudcans on the soil behaviour is excluded and leg load redistribution can not occur. By performing six case-specific calculations the soil behaviour is analysed and the significance of possible mechanisms on the leg load reduction and the spudcan penetration are examined. The simulation of the complete preload procedure, including all four legs and the vessel structure, incorporates the mechanism of leg load redistribution. Leg load redistribution is initiated by the isotach behaviour of the clay and affects the leg load reduction and the spudcan penetration.

Note that in this research a Small Deformation Finite Element (SDFE) analysis is performed and the Wished-In-Place (WIP) method is adopted. The mesh of the soil domain is discretized to identify the optimal mesh in terms of accuracy and computation time. These choices affect the model calculations and results.

#### Soil characteristics

The spudcan penetrations in the simulation of the preload procedure are larger than in the simulation of the single spudcan. The total spudcan penetration for the forward legs in case 2, adopting a reduced OCR for all clay layers, is 50% larger than in the simulation of the single spudcan. The adjacent forward and adjacent aft spudcans reciprocally influence the spudcan penetration into the soil. This influence emphasizes the importance of one model comprising all spudcans to accurately predict the total spudcan penetration.

During the preload procedure the spudcans are loaded and the total vertical stress in the soil increases. The OCR tends to decrease during the spudcan loading, depending on the drainage conditions. The reduction in OCR for one day of consolidation is adopted for case 1 of both simulations, an OCR in the range 2.5 - 4.0 is calculated by the model. The potential change of the OCR due to remoulding of the soil below the spudcan, during penetration, is neglected in this research. The leg load reduction for the first preload cycle in case 1 is solely caused by consolidation. The viscous effects calculated by the model are negligible, which is caused by the application of high OCR values. The model calculates a negligible amount of creep when adopting an OCR value higher than 2. This is substantiated by the results of the analysis relating the undrained shear strength ratio to the strain rate, as presented in section 3.1.1 and depicted in figure 3.7. In case 2, adopting reduced OCR values of 1.4, the viscous effects are more significant. The OCR determines to a large extent the occurrence of the viscous effects in the model. Consequently, the leg load reduction and the time required for sufficient preloading calculated by the model are significantly affected by the adopted values for the OCR of the soil layers.

Zhu and Yin (2000), Sorenson et al. (2007) and Lehane et al. (2009) indicate that the over-consolidation ratio does not seem to affect the general strain-rate dependent behaviour. Test results are presented in these researches which however indicate that the magnitude of strain-rate influence is slightly more significant for lower OCR ( $\leq 2$ ) than for higher OCR.

For high OCR values ( $> 2$ ) the Soft Soil Creep model calculates a very limited amount of creep during spudcan penetration, such that the influence of viscous effects can be neglected. To calculate the amount and rate of creep for over-consolidated soils with the SSC model the OCR input should be decreased. The calculation of the amount and rate of creep by the model is highly dependent on the OCR input, the sensitivity of the creep output to the OCR input is unrealistic. The model does not capture viscous soil behaviour during the preload procedure for OCR input  $\geq 2$ . Consequently, to simulate the preload procedure in (highly) over-consolidated clays the SSC model requires a significant lower OCR input than the actual OCR. Further research on varies over-consolidated soils is advised to identify what the effect of the OCR is on the extent of viscous behaviour of clay.

In this research the permeability of the clay layers is assumed to be equal to  $10^{-5}$  m/day. The effect of the permeability is examined in case 4 by increasing the permeability to  $10^{-3}$  m/day. The excess pore pressures dissipate faster in the soil with larger permeability and a higher degree of consolidation is reached in the consolidation phase of 15 minutes. The total spudcan penetration and leg load reduction are larger and the soil settlement rate and leg load reduction rate increase. These effects influence the total duration of the preload procedure and an accurate estimation of the soil permeability is required to accurately predict this duration.

The Soft Soil Creep model is capable to model the viscous effects and isotach behaviour of the clay. The simulation results of case 1 - 6 indicate the influence of consolidation, viscous and isotach behaviour of clay on

the spudcan penetration and the preload procedure.

In case 1 the leg load reduction is solely caused by the consolidation of the soil. As described in the previous paragraph viscous effects are excluded in case 1, yet a decrease in leg load is calculated for both type of simulations. The consolidation of the soil induces only a small leg load reduction.

The viscous effects are identified by analysing the results from case 2 and 3. The leg load reduction and leg penetration of the active leg pair are larger for a higher penetration rate. At the moment penetration is stopped the viscous resistance diminishes and the spudcan continues to penetrate to create equilibrium. The viscous resistance is larger for a higher penetration rate, causing a larger leg load reduction.

Together with creep and stress relaxation the viscous effects induce the isotach behaviour of clay. The rate of creep and stress relaxation increase for higher strain rates and for a stress state closer to the failure surface. This establishes the process of load redistribution between the active and passive leg pair. During the normal preload procedure the normalized load on the active forward and aft leg is 0.88 and 0.95 respectively, the normalized load on the passive forward and aft leg is 0.40 and 0.52. The stress state of the soil surrounding the active legs is closer to the failure surface which initiates a higher stress relaxation rate of the soil compared to the soil surrounding the passive legs. Consequently, the leg load redistribution is initiated and the load transfers from the active leg pair to the passive leg pair.

The model developed in this research is well capable to incorporate the mechanism of leg load redistribution between the four legs of the jack-up vessel Aeolus.

The soil behaviour, including the extent of the viscous effects, is determined by the soil parameters adopted in the model. Based on the laboratory and in-situ soil tests, the soil is classified and soil parameters are determined and translated to model parameters. Inhomogeneous soil conditions may be expected throughout the project site. As the tests are performed on soil samples originating from different locations at the project site, the test results vary and an approximation of the parameter values is made. The model parameters are calibrated using the results from the oedometer and the triaxial tests. The determination of the values for the modified creep index ( $\mu^*$ ) and the permeability ( $k$ ) of the clay are roughly estimated and based on general observations. Further site specific laboratory and scale model testing are required for a more accurate estimation of the model parameters. The outcomes of this analysis are needed to confirm the soil behaviour, as calculated by the adopted model, corresponds to reality.

The laboratory and in-situ test results indicate elastic anisotropic soil behaviour. The stress paths in a  $p' - q$  plot for the CU triaxial tests on the over-consolidated clay at the project site are inclined within the elastic region of the test. For isotropic linear elastic soil a perfectly straight path is expected, the observed inclination could indicate anisotropic elastic soil properties. The Soft Soil Creep model is not capable to describe the feature of anisotropy and the influence is therefore disregarded in the model simulations. Note that after the elastic phase non-linear contracting behaviour is initiated which causes inclination of the effective stress path in the test results.

One of the possible consequences of the anisotropy of the soil is the steep inclination of both the loading and unloading/reloading curve in the oedometer test results for clay layer 1. The model is not capable to accurately describe the steep inclination of both curves and only the loading curve can be matched. Consequently, the unloading/reloading stiffness of clay layer 1 is overestimated and during unloading the soil expansion is underestimated and potentially affects the leg load redistribution during the preload duration.

Further research is required to identify the consequences of the anisotropy of the soil and the steep loading and unloading/reloading curves on the spudcan penetration and leg load reduction.

#### **Spudcan penetration and preload duration**

The preload procedure adopted at the project site does not consist of separate consecutive preload cycles. After reaching the preload target the leg load is kept constant by continuously extending the legs and one consolidation phase of 25 minutes for each leg pair is executed. The same procedure is simulated with the FE model.

The normalized spudcan penetration depth at the end of the preload procedure, as calculated by the model, is 1.15 and 1.25 for the forward and aft spudcans respectively. The FE model slightly overestimates the spudcan penetration as the penetration depth following from the jacking data is 15% smaller. According to the jacking data the duration of the total preload procedure is approximately two hours. When adopting the same procedure in the model the leg load reduction satisfies the preload criterion. The model results indicate a shorter preload duration would suffice to satisfy the preload criterion. An iterative process is required to identify the minimum preload duration according to the model. The FE model however underestimates the total preload duration.

**Preloading procedure**

The type of preload procedure is varied in an attempt to improve the duration of the total procedure. Two variations of the normal procedure are examined, the overshooting procedure and the alternative procedure. During the procedure the preload target is overshoot to bring the spudcan to the depth, which would have been reached by the creep-like additional penetration under the normal preload procedure. Once the overshoot preload target is reached the leg load is actively reduced to the normal preload target before starting the consolidation phase. The procedure adopted in this research is slightly different: the leg load is *not* actively reduced to the normal preload target *before* starting the consolidation phase. The consolidation phase is started and from the moment the leg load reduces from the overshoot preload target to the normal preload target, consolidation is continued for 15 minutes.

During the alternative procedure the leg load is maintained at the preload target for a longer period of time before starting the consolidation phase.

Both procedures are effective in reducing the number of preload cycles to satisfy the preload criterion. However, compared to the normal preload procedure the duration of one preload cycle increases for both methods. The duration of the preload cycle for the overshooting procedure, as adopted and executed in this research, is longer as the penetration depth is larger and the consolidation phase is extended. For the soil conditions in this research, approximately 45 minutes are required for one preload cycle. The duration of one preload cycle of the alternative procedure depends on the length of the period of time during which the leg load is maintained at the preload target. This phase is followed by the consolidation phase of 15 minutes. One preload cycle of the normal procedure takes significantly less time, being 15 to 20 minutes.

The normal preload procedure requires three preload cycles per leg pair to satisfy the preload criterion. The overshooting and alternative procedure require only one preload cycle. For the given soil conditions, the time to complete the procedure is similar for all methods and approximately equal to 90 minutes. For this specific case the overshooting and alternative method do not improve the time to complete the preload procedure.

When adopting the exact same overshooting procedure proposed by Cathie et al. (2017), the duration of one preload cycle is similar to the duration of one preload cycle of the normal preload procedure. This procedure is expected to be effective in reducing both the required number of preload cycles and the preload duration.

Another possible variation is changing the penetration rate for the normal preload procedure. Reducing the penetration rate results in a lower leg load reduction and is effective in reducing the number of preload cycles. However, due to the lower spudcan penetration rate the duration of a preload cycle increases. For the given soil conditions the time to complete the preload procedure is approximately equal to 120 minutes, adopting a lower penetration rate increases the time to complete the preload procedure.

## Conclusion and recommendations

### 5.1 Conclusion

The aim of this research is to assess the preload duration of the jack-up vessel Aeolus in cohesive soil. In the paragraphs below conclusions on the research sub-objectives and finally the main objective are formulated.

*Represent the soil conditions and behaviour in a 3D FE model.*

A comprehensive 3D finite element model of the soil, the structure and the interaction of both is created using the Finite Element (FE) software package PLAXIS 3D. Small Deformation Finite Element (SDFE) analyses are conducted and the spudcan penetration is simulated via the Wished-In-Place (WIP) method. Jacking data, including the leg load and penetration as function of time during the preload procedure at the project site, is available and used for the verification of the 3D model.

The characteristics and parameters of the soil at the project site are identified by analysing available laboratory and in-situ test results. Two clay layers extending to a depth of 22.7 m and a sand layer beneath are identified and characterised. The clay layers are highly over-consolidated with an OCR in the range of 4 to 7. The results from the laboratory test results indicate elastic anisotropic behaviour of the over-consolidated top clay layer. A possible consequence of the anisotropy of the clay is the relatively high unloading/reloading stiffness for the top clay layer, which is indicated by the oedometer test results showing a steep inclined unloading/reloading curve.

The Soft Soil Creep (SSC) model is used as constitutive model and accounts for viscous effects by formulating irreversible strains by means of viscoplasticity. The feature anisotropy is not described by the SSC model and the influence is therefore disregarded in the model simulations. The influence of the preconsolidation pressure and the strain rate on the undrained shear strength of the clay layer is investigated by simulating consolidated undrained triaxial tests. The Soft Soil Creep calculates that the influence of the strain rate on the undrained strength is negligible for  $OCR \geq 2$ .

*Capture the structural behaviour of Aeolus in a 3D FE model.*

The vessel structure is included in the 3D model to accurately consider the load redistribution between the legs. A simple beam configuration is designed to represent the flexible hull structure. The stiffness of the beams are calibrated based on the results of the predrive analysis of a detailed FE model of the vessel.

A node-to-node anchor element is applied within each leg to establish leg extension and to penetrate the spudcans during the FE simulations. The elements are force-controlled and appear to be effective to simulate the lowering of the legs during the preload procedure. Each leg is equipped with a spudcan which is represented by a rigid body. Interface elements are applied around the spudcan to allow for potential slip planes in the soil domain and to exclude potential singularities.

*Simulate the preload procedure by combining the structural and soil components.*

The complete 3D FE model consists of the soil domain and the simplified vessel structure. The model is capable to simulate the complete preload procedure. The viscous effects and isotach behaviour are captured well by the model and allow for the simulation of load redistribution between the legs.

Two types of simulations are performed: (1) the single spudcan penetration and (2) the complete preload procedure including all four legs and the connecting structure. Comparison of the results of the two simulations indicates that the penetration of a spudcan influences the penetration of an adjacent spudcan. The reciprocal influence of the forward spudcan and of the aft spudcans emphasizes the importance of one model comprising all spudcans in the same 3D soil domain.

Based on the comparison of the jacking data and the model results it is concluded that the model slightly overestimates the spudcan penetration and underestimates the total preload duration.

*Analyse the leg load redistribution during the preload procedure.*

As a result of the sensitivity of the creep output to the OCR input and in an attempt to incorporate the viscous soil behaviour, the OCR input is significantly reduced compared the actual OCR of the soil. During spudcan penetration the OCR is expected to vary in the range 2.5 - 4 while an OCR model input of 1.4 is adopted to capture the viscous effects, as observed in the jacking data. The viscous behaviour of the clay is proportional to the load redistribution between the legs of the vessel and affects the total preload duration. The potential change of the OCR and soil strength due to remoulding of the soil below the spudcan, during penetration, is neglected in this research.

The overshooting and alternative procedure are variations on the normal preload procedure. The procedures are simulated to examine possible improvements of the preload duration. The overshooting procedure adopted in this research differs from the procedure proposed by Cathie et al. (2017): in this research the leg load is *not* actively reduced to the normal preload target *before* starting the consolidation phase.

Both the overshooting and alternative preload procedure are effective in reducing the number of preload cycles to satisfy the preload criterion. For both procedures the duration of a preload cycle however, increases compared to the normal procedure. For the soil conditions adopted in this research both procedure types do not improve the elapsed time to complete the total preload procedure. It is expected that the preload duration of the overshooting procedure is improved by actively reducing the leg load to the normal preload target, before starting the consolidation phase.

Using a lower spudcan penetration rate during the normal preload procedure is also effective in reducing the number of preload cycles but significantly increases the elapsed time to complete the preload procedure.

**Develop a 3D model to assess the preload duration of the jack-up vessel Aeolus in cohesive soil.**

A 3D model is developed to conduct a SDFE analysis of the preload procedure of the jack-up vessel Aeolus. The Soft Soil Creep (SSC) model is used as constitutive model and accounts for viscous effects by formulating irreversible strains by means of viscoplasticity. The vessel structure is represented by a simple beam configuration which is capable to accurately consider the load redistribution between the legs during preloading. Given the limitations of the model and the consequences of the assumptions made, this model is capable to assess the preload duration. The above conclusions have been made on the basis of site specific soil conditions.

## 5.2 Limitations

In this research some important assumptions were made. The main assumptions and corresponding supposed consequences are:

- Idealised and perfect homogeneous soil conditions are assumed as the SSC model input. The soil model is calibrated for the best fit with the laboratory and in-situ soil tests. It is however unlikely that similar soil conditions are found at all four legs and throughout the project site.  
As the structural components and corresponding geometrical and mechanical characteristics are based on the specifications of Aeolus and the soil conditions are site specific, the results from this research tend to be location specific. Further site specific laboratory and scale model testing are required to confirm observations drawn from this research.
- In the FE simulation of the preload procedure the effects of horizontal environmental and operational loading are neglected. This type of loading could influence the observed leg loads, spudcan penetrations and overall behaviour. However, as vessel preloading is only conducted during, though subjective, calm weather circumstances, predominantly vertical loads are deemed to influence the loads. Therefore it is expected that disregarding any influence of horizontal loading on the preload procedure has a small effect on the results.
- Complete backfill mechanism is assumed during spudcan penetration. The weight of the soil volume flowing on top of the spudcan affects the final penetration of the spudcan. The use of complete backfill is a conservative approach, as the total spudcan load increases when more soil is to be carried. Backfill is a complex mechanism and to identify at which depth the process starts, further research is required.

The main limitations of this research due to the choice of the FE software in combination with the constitutive soil model are:

- The calculation of the amount and rate of creep by the Soft Soil Creep model is highly dependent on the OCR input. The model does not capture viscous soil behaviour during the preload procedure for an OCR input  $\geq 2$ . Consequently, for the application of simulating the preload procedure in (highly)

over-consolidated clays, the SSC model requires a significant lower OCR input than the actual OCR at the project site.

- Oedometer tests, performed with soil samples from the project site, show that the value for the unloading/reloading stiffness for clay layer 1 is similar to the value of the primary loading stiffness. This is a possible consequence of the anisotropy of the results as described in section 2.3.5. The SSC model does not allow to simultaneously represent high values for both stiffness parameters. For the purpose of this research it is chosen to match the primary loading stiffness from the laboratory tests and allow for deviation from the actual unloading/reloading stiffness. The model overpredicts the unloading/reloading stiffness causing the soil rebound effect to be underestimated. The test and model results and calibration of the model parameters are presented in section 3.1.1.
- In this research Small Deformation Finite Element (SDFE) analyses are conducted. A simplified approach is used where spudcan penetration is simulated via Wished-In-Place (WIP) method. Complete spudcan penetration, starting at the soil surface, is associated with large deformations. To accurately capture the corresponding large strains and displacements and installation effects a Large Deformation Finite Element (LDFE) or a Material Point Method (MPM) analysis is required. Both methods are relatively complicated and computationally expensive.
- The results from the consolidated undrained triaxial tests, performed on different soil samples from both clay layers (layer 1 and 2), indicate anisotropic elastic properties for both clay layers. The SSC model does not incorporate soil anisotropy and the phenomenon is disregarded in the model simulations.
- Both clay layers are identified to be over-consolidated with an OCR varying within the range 4 - 7 prior to spudcan loading. For over-consolidated clays the plastic strains already start to generate at a stress state within the yield boundary (Banerjee and Stipho, 1978). This phenomenon is not captured by the SSC model as it describes a sharp distinction between the elastic and plastic strains.
- The leg extension mechanism within the 3D FE model requires horizontal fixation of the corresponding nodes to ensure stable equilibrium. Due to the fixation the spudcan is prevented to move horizontally. Application of the 3D FE model in simulations where horizontal loads (uneven seabed) are to be considered, results in unreliable leg loads, spudcan penetrations and overall behaviour.

### 5.3 Recommendations

Based on the outcomes of the research recommendations for further research are proposed. The recommendations are:

- The preload procedure simulation in the 3D FE software is relatively expensive in terms of time and memory usage. For a 2D PLAXIS axisymmetric analysis 15-node triangle elements are used and for a 3D PLAXIS analysis 10-node tetrahedral elements are used, the difference in order of interpolation between the elements is two. Compared to 2D, modelling the complete soil domain in 3D requires a significant amount of elements to achieve the same accuracy which slackens the computation time and increases the required memory usage. Spudcan penetration can be modelled making use of a 2D axisymmetric model. By connecting the individual spudcan models via a 3D model incorporating the vessel structure, the load redistribution can be simulated. Adopting an approach combining 2D axisymmetric and 3D modelling in future research optimizes the number of elements and memory usage. Note, this method is only allowed on the condition that the reciprocal influence of the spudcans within the soil domain is negligible.
- The leg load reduction over time is affected by several processes, including: consolidation, viscous effects and leg load redistribution. The effect of this criterion on the total duration of the procedure can be examined by accurately determining the loads on the vessel and the leg load over time, which is feasible with the model as developed in this research. However, the justification of the formulation of the preload criterion in relation to the vessel structure, the soil characteristics and the interaction of both could be subject of further research. This research could provide a more thorough insight in this criterion value in relation to the system and could have a positive impact on the preload duration.
- The calculation of the amount and rate of creep by the Soft Soil Creep (SSC) model is highly dependent on the OCR input. Further research on the viscous behaviour of over-consolidated (OC) soils may lead to a better understanding of the extent of viscous effects in OC clays during preloading. Further, this research could contribute to the development of a procedure on how to accurately represent viscous behaviour of OC soils by the SSC model or any other constitutive model.

- In the absence of test results to accurately determine the modified creep index,  $\mu^*$ , the value can be roughly estimated and based on general observations. In preparation of the site specific assessment of the preload procedure it is advisable to conduct undrained creep tests to obtain a more accurate value for  $\mu^*$ .
- Remoulding of the soil below the spudcan, during penetration, is neglected in this research. However, remoulding potentially affects the strength and the over-consolidation ratio (OCR) of the soil surrounding the spudcan. Further research on strength degradation and reduction of the OCR during spudcan penetration could lead to more insight in the extent of the effect of remoulding.

# Bibliography

- Andersen, K. H., Andresen, L., Jostad, H., and Clukey, E. C. Effect of skirt-tip geometry on set-up outside suction anchors in soft clay. *International Conference on Offshore Mechanics and Arctic Engineering*, 2004.
- Andresen, L., Edgers, L., and Jostad, H. P. Capacity analysis of suction anchors in clay by PLAXIS 3D foundation. *Plaxis Bulletin*, 24:5–9, 2008.
- Augustesen, A., Liingaard, M., and Lade, P. V. Evaluation of time-dependent behaviour of soils. *International journal of geomechanics*, 4(3):137–156, 2004.
- Banerjee, P. K. and Stipho, A. S. Associated and non-associated constitutive relations for undrained behaviour of isotropic soft clays. *International Journal Numerical Analysis Methods Geomechanics*, 2(1):35–56, 1978.
- Bathe, K. J. *Finite Element procedures in engineering analysis*. Prentice-Hall New Jersey, 1982.
- Bienen, B. and Cassidy, M. J. Advances in the three-dimensional fluid-structure-soil interaction analysis of offshore jack-up structures. *Marine Structures*, 19:110–140, 2006.
- Bienen, B. and Cassidy, M. J. Three-dimensional numerical analysis of centrifuge experiments on a model jack-up drilling rig on sand. *Canadian Geotechnical Journal*, 46:208–224, 2009.
- Bienen, B. and Cassidy, M. J. Set up and resulting punch-through risk of jack-up spudcans during installation. *Journal of Geotechnical and Geoenvironmental Engineering*, 139(12):2048–2059, 2013.
- Brinkgreve, R. B. J. *Geomaterial models and numerical analysis of softening*. PhD thesis, Delft University of Technology, The Netherlands, 1994.
- Brinkgreve, R. B. J., Engin, E., and Engin, H. K. Validation of empirical formulas to derive model parameters for sands. *Numerical methods in geotechnical engineering* (eds T. Benz and S. Nordal). Rotterdam, The Netherlands: CRC Press/Balkema, 2010.
- Brinkgreve, R. B. J., Burg, M., Liim, L. J., and Andreykiv, A. On the practical use of the material point method for offshore geotechnical applications. Seoul, 2017. *Proceedings of the 19th International Conference on Soil Mechanics and Geotechnical Engineering*.
- Brinkgreve, R. B. J., Kumarswamy, S., Swolfs, W. M., and Foria, F. *PLAXIS 3D Reference Manual*. PLAXIS B.V., The Netherlands, 2018a.
- Brinkgreve, R. B. J., Kumarswamy, S., Swolfs, W. M., and Foria, F. *PLAXIS 3D Materials Models Manual*. PLAXIS B.V., The Netherlands, 2018b.
- Brinkgreve, R. B. J., Kumarswamy, S., Swolfs, W. M., and Foria, F. *PLAXIS Finite Element Code for soil and Rock Analyses*. The Netherlands: 3D-Version, 2018c.
- Brinkgreve, R. B. J., Kumarswamy, S., Swolfs, W. M., and Foria, F. *PLAXIS Finite Element Code for soil and Rock Analyses*. The Netherlands: 2D-Version, 2018d.
- Cassidy, M. J. Offshore foundation systems for resource recovery: Assessing the three-dimensional response of jack-up platforms. *KSCE Journal of Civil Engineering*, 15(4):623–634, 2011.
- Cassidy, M. J., Taylor, P. H., Taylor, R. E., and Houlsby, G. T. Evaluation of long-term extreme response statistics of jack-up platforms. *Ocean Engineering*, 29:1603–1631, 2002.
- Cassidy, M. J., Martin, C. M., and Houlsby, G. T. Development and application of force resultant models describing jack-up foundation behaviour. *Marine Structures*, 17:165–193, 2004a.
- Cassidy, M. J., Taylor, R. E., and Houlsby, G. T. Analysis of jack-up units using a constrained newwave methodology. *Applied Ocean Research*, 23(4):221–234, 2004b.

- Cassidy, M. J., Vlahos, G., and Hodder, M. Assessing appropriate stiffness levels for spudcan foundations on dense sand. *Marine Structures*, 23:187–208, 2010.
- Cathie, D. N., Versteede, H., and Kuo, M. Y. K. Planning the preloading procedure to account for rate-effects in clays. London, 2017. International Conference: The Jack-Up Platform.
- Dean, E. T. R. *Offshore geotechnical engineering - Principles and Practice*. ICE Publishing, 2010.
- Dean, E. T. R. and Metters, R. Cyclic stiffness degradation in non-linear jackup dynamics. Houston, 2009. Proceedings of Offshore Technology Conference, OTC 19998.
- Dean, E. T. R., James, R. G., Schofield, A. N., and Tsukamoto, Y. Numerical modelling of three-leg jackup behaviour subject to horizontal load. *Soils and Foundations*, 37(2):17–26, 1997.
- Dimitriou, A. Improving jack-up capabilities. Master's thesis, Delft University of Technology, 2014.
- Fila, J. Numerical assessment of preloading strategies for jack-up vessels in cohesive soils. Master's thesis, Delft University of Technology, 2018.
- Globaldata. *Healthy competition: demand grows for specialised offshore vessels*. World Expro, 2012.
- Graham, J. and Houlsby, G. T. Anisotropic elasticity of a natural clay. *Géotechnique*, 33(2):165–180, 1983.
- Hedrick, W. P. and Verret, S. M. Jackup operations: new operational recommended practices. Houston, Texas, 2007. Proceedings of Offshore Technology Conference, OTC 18980.
- Hossain, M. and Randolph, M. F. Deep-penetrating spudcan foundations on layered clays: numerical analysis. *Géotechnique*, 60(3):171–184, 2010.
- Hossain, M., Hu, Y., Randolph, M. F., and White, D. J. Limiting cavity depth for spudcan foundations penetrating clay. *Géotechnique*, 55(9):679–690, 2005.
- Hossain, M. S. and Randolph, M. F. New mechanism-based design approach for spudcan foundations on single layer clay. *Journal of Geotechnical and Geoenvironmental Engineering*, 135(9):1264–1274, 2009a.
- Hossain, M. S. and Randolph, M. F. Effect of strain rate and strain softening on the penetration resistance of spudcan foundations on clay. *International Journal of Geomechanics*, 9(3):122–132, 2009b.
- Hossain, M. S., Randolph, M. F., Hu, Y., and White, D. J. Cavity stability and bearing capacity of spudcan foundations on clay. Houston, Texas, 2006. Proceedings of Offshore Technology Conference, OTC 17770.
- Houlsby, G. T. Interactions in offshore foundation design. *Géotechnique*, 66(10):791–825, 2016.
- Houlsby, G. T. and Martin, C. T. Undrained bearing capacity factors for conical footings on clay. *Géotechnique*, 53(5):513–520, 2003.
- Hu, Y. and Randolph, M. F. A practical numerical approach for large deformation problems in soil. *International Journal for Numerical and Analytical Methods in Geomechanics*, 22:327–350, 1998.
- InSafeJIP. Improved guidelines for the prediction of geotechnical performance of spudcan foundations during installation and removal of jack-up units. Technical report, Joint Industry Funded Project, 2011.
- ISO. Petroleum and natural gas industries – site-specific assessment of mobile offshore units – part 1: Jack-ups. Technical report, International Organization for Standardization, ISO19905-1, 2016.
- Jamiolkowski, M., Lopresti, D. C. F., and Manassero, M. Evaluation of relative density and shear strength of sands from cone penetration test and flat dilatometer test. Soil Behavior and Soft Ground Construction (GSP 119), ASCE, Reston/VA, 201-238, 2001.
- Karstunen, M. and Amavasai, A. *Soft soil modelling and parameter determination*. Chalmers University of Technology, Gothenburg, Sweden, 2017.
- Koole, T. Modern jack-ups and their dynamic behaviour. Master's thesis, Delft University of Technology, 2015.

- Kulhawy, F. H. and Mayne, P. H. *Manual on estimating soil properties for foundation design*. Electric Power Research Institute, Report EL 6800, 1990.
- Ladd, C. C. and DeGroot, D. J. Recommended practice for soft ground site characterization: Arthur casagrande lecture. Cambridge, 2003. Proceedings of Soil and Rock America, P. J. Culligan, H. H. Einstein, and A. J. Whittle, eds., Verslag Gluckauf GMBH, Essan, Germany, 1:3-57, 2003.
- Ladd, C. C. and Foott, R. New design procedure for stability of soft clays. *Journal of Geotechnical Engineering ASCE*, 100:763–786, 1974.
- Ladd, C. C. and Lee, S. Engineering properties of segipe clay: Tps progress rept no 4. Cambridge, 1993. Research Rept R93-07, Dept of Civil and Environmental Eng, MIT.
- le Tirant, P. *Design guides for offshore structures*. Technip Editions, 1993.
- Lee, J. and Randolph, M. Penetrometer-based assessment of spudcan penetration resistance. *Journal of Geotechnical and Geoenvironmental Engineering*, 137(6):587–596, 2011.
- Lehane, B. M., Oloughlin, C. D., Gaudin, C., and Randolph, M. F. Rate effects on penetrometer resistance in kaolin. *Géotechnique*, 59(1):41–52, 2009.
- Luking, J., Wenzel, S., and Martens, L. Modelling installation and construction of offshore wind farms. pages 1–12. 33rd International Conference on Ocean, Offshore and Arctic Engineering, OMAE2014, 2014.
- Lunne, T., Robertson, P. K., and Powell, J. J. M. *Cone-penetration testing in geotechnical practice*. Taylor and Francis, 1997.
- Mahajan, S. P. and Budhu, M. Viscous effects on penetrating shafts in clays. *Acta Geotechnica*, 1:157–165, 2006.
- Martin, C. M. *Physical and numerical modelling of offshore foundations under combined loads*. PhD thesis, University of Oxford, 1994.
- Mayne, P. W. Cam-clay predictions of undrained strength. *Journal of Geotechnical Engineering Division*, 106: 1219–1242, 1980.
- Menzies, D. and Roper, R. Comparison of jackup rig spudcan penetration methods in clay. Houston, Texas, 2008. Proceedings of Offshore Technology Conference, OTC 19545.
- Muir-Wood, D. *Soil behaviour and critical state soil mechanics*. Cambridge University Press, Cambridge, 1991.
- Osborne, J., Bienen, B., Cassidy, M. J., and Randolph, M. F. Improved guidelines for the prediction of geotechnical performance of spudcan foundations during installation and removal of jack-up units, otc 20291. Proceedings of Offshore Technology Conference, 2009.
- Pisanò, F., Schipper, R., and Schreppers, G. J. Input of fully 3d fe soil-structure modelling to the operational analysis of jack-up structures. *Marine Structures*, 63:269–288, 2019.
- Pucker, T., Bienen, B., and Henke, S. Cpt based prediction of foundation penetration in siliceous sand. *Applied Ocean Research*, 41:9–18, 2013.
- Qiu, G. and Grabe, J. Numerical investigation of bearing capacity due to spudcan penetration in sand overlying clay. *Canadian Geotechnical Journal*, 49(12):1393–1407, 2012.
- Randolph, M. and Gourvenec, S. *Offshore geotechnical engineering*. Spon Press, 2011.
- Richardson, A. M. and Whitman, R. V. Effect of strain rate upon undrained shear resistance of a saturated remoulded fat clay. *Géotechnique*, 13(4):310–324, 1963.
- Robertson, P. K. Interpretation of cone penetration tests - a unified approach. *Canadian Geotechnical Journal*, 46:1337–1355, 2009.
- Robertson, P. K. Soil behaviour type from the cpt: an update. California, 2010. 2nd International Symposium on Cone Penetration Testing, CPT'10.

- Robertson, P. K. and Campanella, R. G. Interpretation of cone penetration tests. part i: Sand. *Canadian Geotechnical Journal*, 20(4):718–733, 1983.
- Schofield, A. and Wroth, P. *Critical state soil mechanics*. Cambridge University, 1968.
- Shi, Z., Hambleton, J. P., and Buscarnera, F. Bounding surface elasto-viscoplasticity: a general constitutive framework for rate-dependent geomaterials. *Journal of Engineering Mechanics*, 145(3):1–13, 2019.
- Sivasithamparam, N., Karstunen, M., and Bonnier, P. Modelling creep behaviour of anisotropic soft soils. *Computers and Geotechnics*, 69:46–57, 2015.
- Skempton, A. W. The bearing capacity of clays. London, 1951. Building Research Congress, Division 1, Part 3: 180-189.
- SNAME. *Guidelines for Site Specific Assessment of Mobile Jack-Up Units*. The Society of Naval Architects and Marine Engineers, 2008.
- Sorenson, K. K., Baudet, B. A., and Simpson, B. Influence of structure on time-dependent behaviour of a stiff sedimentary clay. *Géotechnique*, 1:113–124, 2007.
- Stanier, S. A., Ragni, R., Bienen, B., and Cassidy, M. J. Observing the effects of sustained loading on spudcan footings in clay. *Géotechnique*, 64(11):918–926, 2014.
- Tho, K. K., Leung, C. F., Chow, Y. K., and Swaddiwudhipon, S. Eulerian finite element simulation of spudcan-pile interaction. *Canadian Geotechnical Journal*, 50(6):595–608, 2012a.
- Tho, K. K., Leung, C. F., Chow, Y. K., and Swaddiwudhipong, S. Eulerian finite-element technique for analysis of jack-up spudcan penetration. *International Journal of Geomechanics*, 12(1):64–73, 2012b.
- Thompson, R. S. G. *Development of non-linear numerical models appropriate for the analysis of jack-up units*. PhD thesis, University of Oxford, 1996.
- Timoshenko, S. P. On the correction of shear of the differential equation for transverse vibration of prismatic bars. *Philosophical Magazine*, 41:744–746, 1921.
- Veritas, D. N. Recommended practice dnv-rp-c104, self-elevating units. Technical report, Norway: Det Norske Veritas, 2015.
- Vermeer, P. A. and Neher, H. P. A soft soil model that accounts for creep. *Proc. Int. Symp. Beyond 2000 in Computational Geotechnics - 10 years of PLAXIS International*, pages 249–261, 1999.
- Vlahos, G., Cassidy, M. J., and Martin, C. M. Numerical simulation of pushover tests on a model jack-up platform. *Géotechnique*, 61(11):947–960, 2011.
- Yu, L., Hu, Y., Randolph, M. F., and Kong, X. Numerical study of spudcan penetration in loose sand overlaying clay. *Computers and Geotechnics*, 46:1–12, 2012.
- Zeevart, L. Discussion on effect of driving piles into soft clay. *Transactions ASCE*, 115:286–292, 1948.
- Zhang, Y., Bienen, B., and Cassidy, M. J. Jack-up push-over analyses featuring a new force resultant model for spudcans in soft clay. *Ocean Engineering*, 81:139–149, 2014.
- Zhou, H. and Randolph, M. F. Computational techniques and shear band development for cylindrical and spherical penetrometers in strain-softening in clay. *International Journal of Geomechanics*, 7(4):287–295, 2007.
- Zhu, J. and Yin, J. Strain=rate-dependent stress-strain behavior of overconsolidated hong kong marine clay. *Canadian Geotechnical Journal*, 37(6):1272–1282, 2000.
- Zwanenburg, C. and Barends, F. B. J. Unravelling the anisotropy of peat. Osaka, Japan, 2005. Proceedings of the 16th International Conference on Soil Mechanics and Geotechnical Engineering, page 469-474.

## Soil parameters

### Void ratio ( $e_0$ )

The void ratio is known at 10 depths, eight in clay layer 1 and two in clay layer 2. The void ratio over depth is relatively constant for both layers, an average value representing the void ratio for each layer suffices.

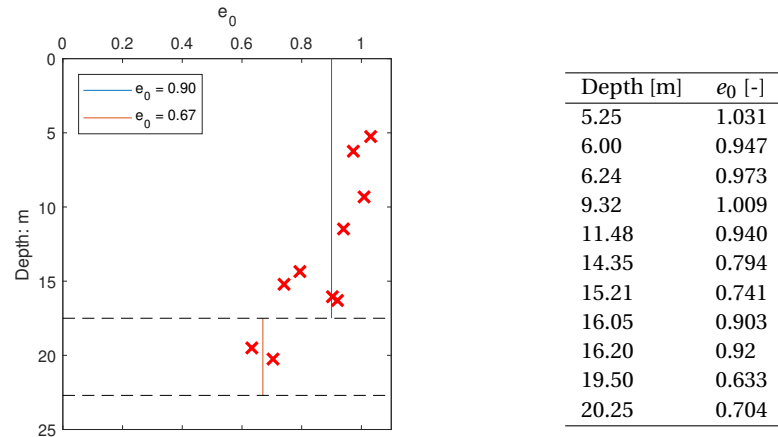


Figure A.1: The (initial) void ratio over depth.

### Permeability ( $k$ )

The plasticity chart, figure A.2, and the soil classification chart from chapter 2.3, figure 2.7, indicate a clay with low permeability. An estimated value of 10 m/day is assumed for the permeability of the clay in both layers.

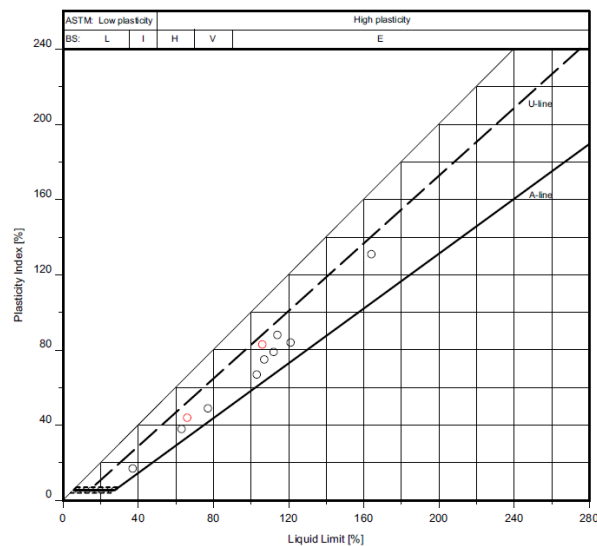


Figure A.2: Plasticity chart for the two clay layers, represented by both the black and red circles.

### Relative Density ( $D_r$ )

Based on the relations as proposed by Jamiolkowski et al. (2001) the relative density,  $D_r$ , is determined from the CPT results. The relation between the corrected cone resistance,  $q_{t1}$ , and  $D_r$  is given next to figure A.3 below. An average value of 65% is assumed for the whole sand layer. The relations proposed by Brinkgreve et al. (2010) link the  $D_r$  to the Hardening Soil (HS) model parameters.

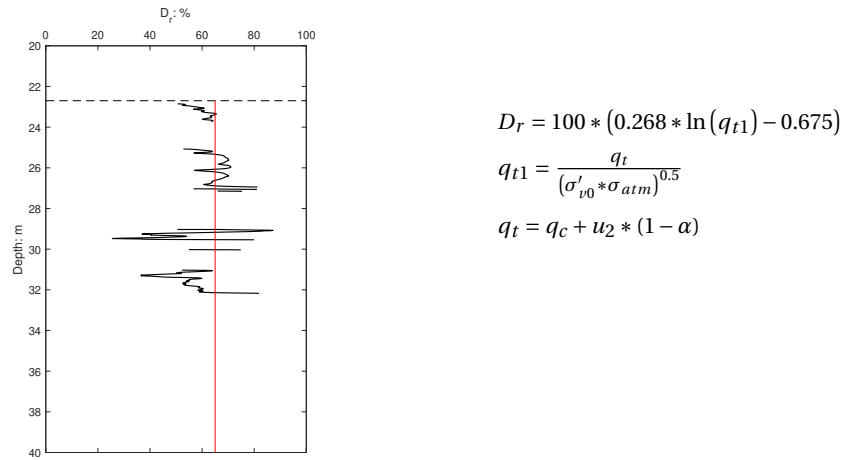


Figure A.3: Relative density,  $D_r$ , profile over depth, the average value for the sand layer is 65%.

### Friction angle ( $\phi$ ) and dilatancy angle ( $\psi$ )

The friction and dilatancy angle,  $\phi$  and  $\psi$  respectively, for the sand layer are determined from the CPT results using the relations as proposed by Robertson and Campanella (1983) and Kulhawy and Mayne (1990). An average value for each parameters is used to represent the sand layer,  $\phi = 40^\circ$  and  $\psi = 10^\circ$ .

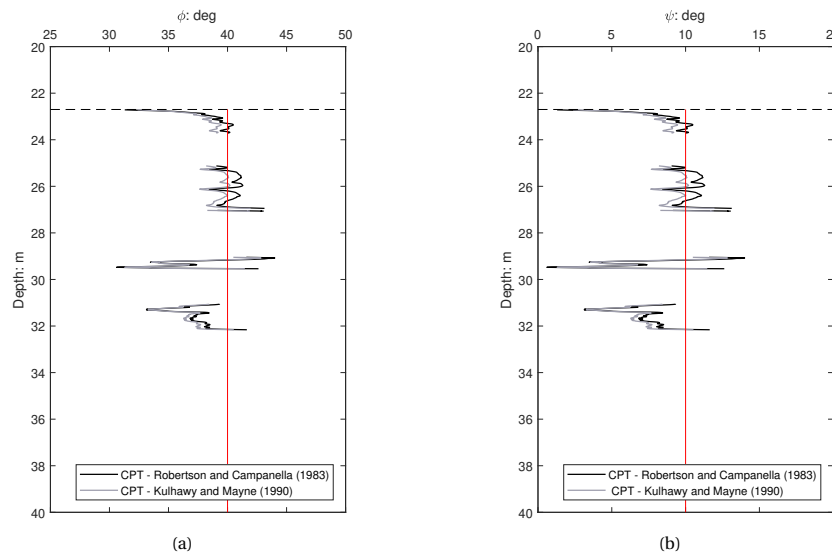


Figure A.4: (a) Friction angle and (b) dilatancy angle over depth for the sand layer between 22.7-40.0 m, based on the CPT data. The two profiles are determined according the formulas presented by Robertson and Campanella (1983) and Kulhawy and Mayne (1990). Based on these results an average value for both parameters are chosen:  $\phi = 40$  and  $\psi = 10$ .

Robertson and Campanella (1983):

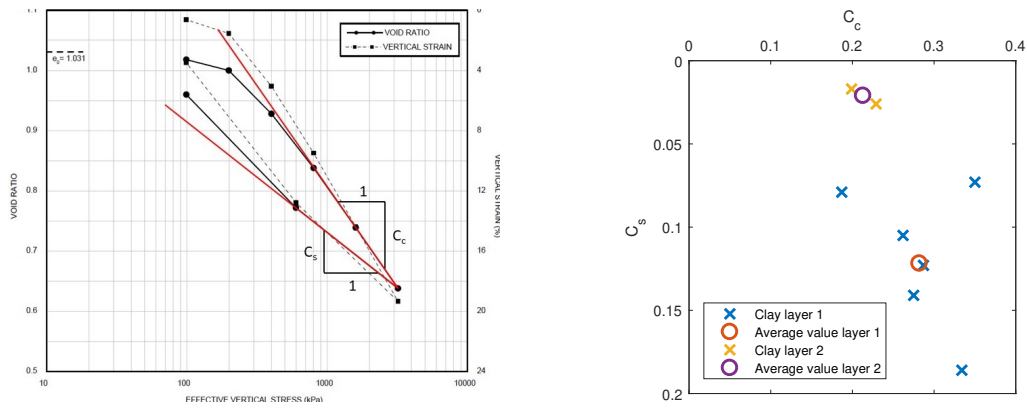
$$\tan(\phi) = \frac{1}{2.68} \left( \log\left(\frac{q_c}{\sigma'_{v0}}\right) + 0.29 \right) \quad (\text{A.1})$$

Kulhawy and Mayne (1990):

$$\phi = 17.6 + 11 * \log(Q_t) \quad (\text{A.2})$$

### Compression and swelling index ( $C_c, C_s$ )

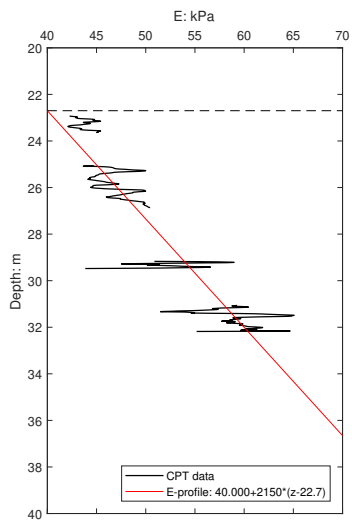
Both stiffness indices follow from the oedometer results. The compression index is determined from the tangent of the loading curve and the swelling index from the tangent of the unloading curve. The procedure is shown in figure A.5a, the results following from the eight oedometer tests are depicted in figure A.5b. Average values for both parameters in both layers are selected.



(a) Example to determine the stiffness parameters using the oedometer test results. (b) Calculated and average compression and swelling indices for both clay layers.

### Young's Modulus (E)

A relation between Young's Modulus and the corrected cone resistance is proposed by Robertson (2009). The modulus factor, as used in this relation, is determined from the soil behaviour type index. The relations are listed next to figure A.6.



$$E = \alpha_E * (q_t - \sigma_v)$$

$$\alpha_E = 0.015 * (10^{0.55 * I_c + 1.68})$$

$$I_c = (3.47 - \log(Q_t))^2 + \left( (1.22 + \log(R_f))^2 \right)^{0.5}$$

$$R_f = \frac{f_s}{q_t - \sigma_v} * 100\%$$

Figure A.6: Young's modulus ( $E$ ) over depth for the sand layer between 22.7-40.0 m, based on the CPT data.

### Over-consolidation ratio (OCR)

The over-consolidation ratio (OCR) is related to the CPT results via the normalized cone resistance, as suggested by Kulhawy and Mayne (1990). Using the Casagrande interpretation method also from the oedometer test results the OCR is determined. The results following from both methods are depicted in figure A.7. The values for the OCR following from the CPT results within the upper 5 m are extremely high and might be unreliable. Clay layer 1 is subdivided in three layers each with a different OCR, clay layer 2 is represented by just one OCR. The chosen values for these layers are added to the figure.

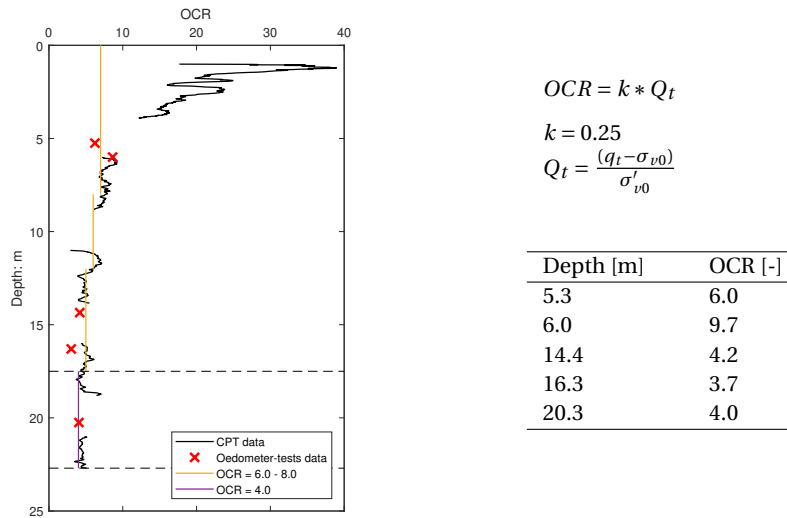


Figure A.7: Over-consolidation ratio (OCR) over depth for the clay layers between 0-22.7 m, based on the CPT data and oedometer test data.

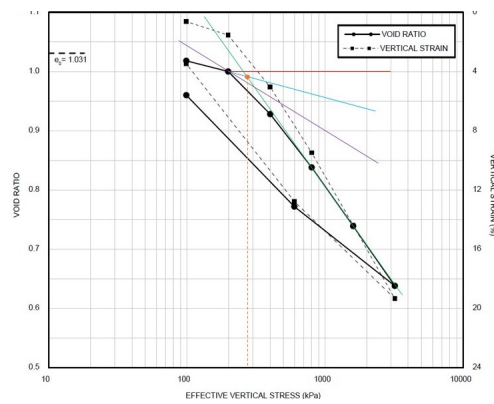


Figure A.8: Example of the Casagrande method applied at oedometer test results.

## FE spudcan shape

Using the exact spudcan shape to penetrate into the soil results in unrealistic high peaks in stresses and strains. Application of interface elements in combination with the exact spudcan shape does not improve the results. To limit the number of sharp corners the shape of the structure within the soil domain is simplified. Three different designs are used for a penetration simulation, the exact spudcan shape, the simplified spudcan shape including tip and the simplified spudcan shape excluding tip. These designs are depicted in figure B.1a, B.1b and B.1c respectively. The exact spudcan shape does not include interfaces and the two simplified designs are used both with and without interfaces.

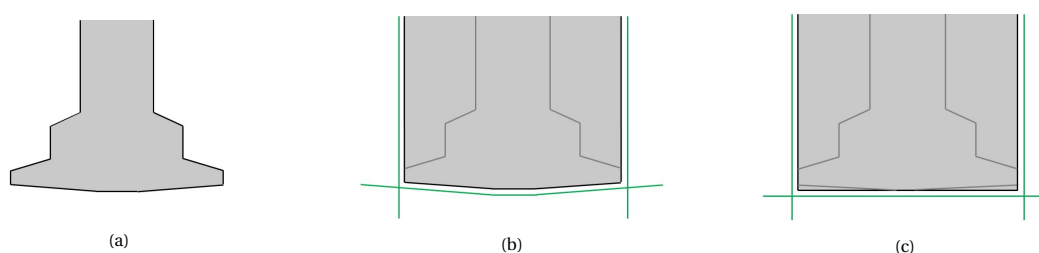


Figure B.1: Three spudcan designs used for the bearing capacity analysis. (a) Exact spudcan shape, (b) simplified spudcan shape including the tip and (c) simplified spudcan shape excluding the tip. The green lines in the latter two figures represent the interface configuration.

The results for the bearing capacity analyses are depicted in figure B.2. The changes in spudcan have limited effect on the bearing capacity and penetration. The normalized leg load at a penetration of 0.35 m (relative to the normalized initial depth of 1.0) varies between 0.92 and 0.9 for all variants. It is concluded adapting the spudcan shape has negligible impact on the calculation.

It should be noted that for the variant with the exact spudcan shape the weight of the soil volume on top of the spudcan is added to the observed bearing capacity, assuming complete backfill.

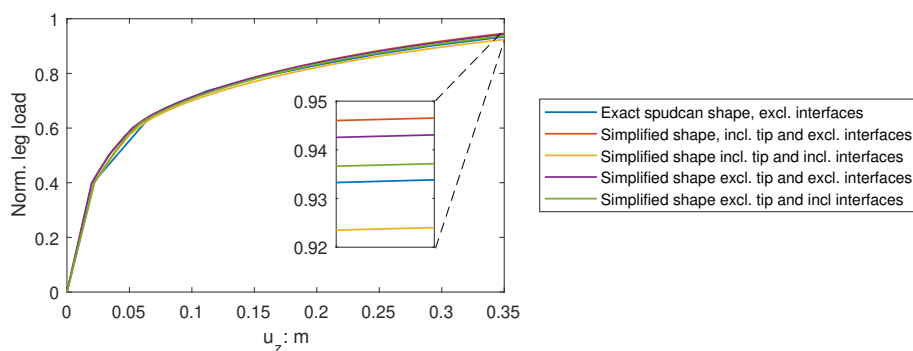


Figure B.2: Leg load as function of additional penetration for different spudcan designs, the normalized initial spudcan depth in this analysis is 1.0.

## Extension mechanism

Surface contraction can be applied to a plate component to simulate contraction or extension of the component. By specifying a constant contraction in percentage the plate component contracts for a positive value and extends for a negative value. Since the surface contraction only can be applied on a flat plate, two plates positioned in an angle of  $90^\circ$  can be used to approach the behaviour of the circular leg. Further, the plate is rigidly connected to the leg-beams which establishes a representative continuous leg.

Since only contraction and extension of the component can be specified, this analysis is displacement controlled. PLAXIS does not enable the user to limit the displacement when a certain load is reached, while this is essential to control and regulate the applied leg load during the preloading stage. The extension mechanism using the surface contraction option is illustrated in figure C.1.

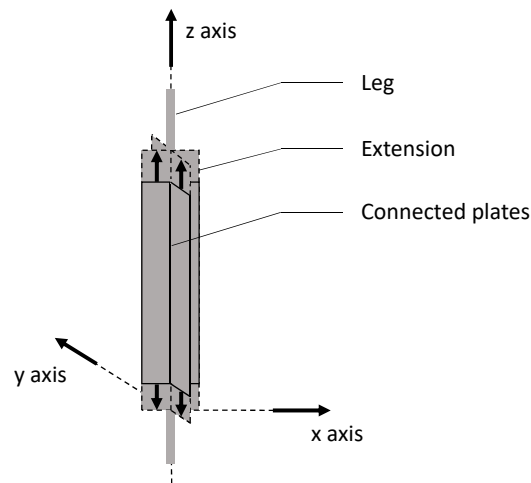


Figure C.1: Surface contraction as leg extension mechanism.

D

## Results predrive analysis - Confidential

## 2D mesh discretization

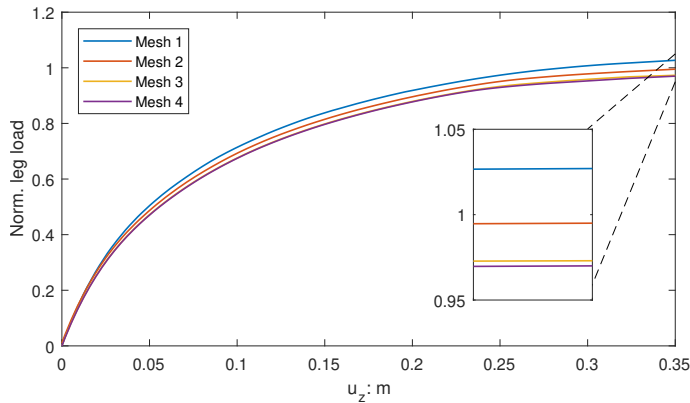
Mesh discretization is performed in 2D using axisymmetry. With PLAXIS 2D a 'slice' of the spudcan and the soil volume is modelled in a 2D plane. This analysis is performed using the Mohr-Coulomb constitutive model with parameter values as described in table 3.8. 15-node triangle elements are used, the element provides second order interpolation of displacements and four Gauss integration points. Five different mesh discretizations are used, the specifications are shown in table E.1. The mesh discretization is based on the calculation of the bearing capacity for the spudcan at a depth of 10 meter.

Since in the axisymmetric analysis only one radian of the circular spudcan is modelled, the result from the 2D PLAXIS model should be multiplied by  $2 * \pi$  to determine the total leg load.

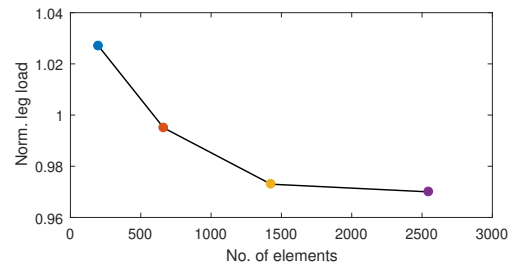
In figure E.1a the result for each of the meshes is shown. Applying smaller elements results in a higher accuracy, closer to the actual solution. The five meshes result in similar bearing capacity values, the difference between the most fine and most coarse mesh is only 3%. The result of the finest 2D mesh, mesh 4, is used as reference for the 3D discretization.

Table E.1: The 2D meshes with specification on the number of elements and nodes.

Mesh	No. of elements	No. of nodes	Smallest element size [m]	Calc. leg load [MN]
Mesh 1	199	1655	1.0	1.03
Mesh 2	663	5427	0.6	1.00
Mesh 3	1426	11589	0.4	0.97
Mesh 4	2574	20837	0.3	0.97



(a) Leg load as function of the penetration.



(b) Leg load as function of the number of elements.

Figure E.1: Mesh discretization results for the 2D analysis.

## Calibration soil model

This appendix depicts the results of the calibration of the Soft Soil Creep model. The model parameters are calibrated using the laboratory test results, oedometer and consolidated undrained triaxial test. Creep is excluded when the other parameters are calibrated using the Soft Soil model. The modified creep index is the final parameter to be calibrated using the SSC model. The following information is presented in the appendix:

- Soil parameters
- Soft Soil model calibration
- Laboratory and PLAXIS test results
- Soft Soil Creep model calibration

### Soil parameters

In table F.1 the soil parameters are shown as determined from the in-situ and laboratory tests.

Table F.1: Soil parameters for both clay layers.

Layer	$\gamma$	$e_0$	$\nu$	$k$	$\phi$	$c$	$\psi$	$C_c$	$C_s$	$s_u$
[-]	[kN/m <sup>3</sup> ]	[-]	[-]	[m/day]	[deg]	[kPa]	[deg]	[-]	[-]	[kPa]
1	18.5	0.90	0.5	$10^{-5}$	30	0	0	0.28	0.13	$70 + 4.16 * z$
2	20.5	0.65	0.5	$10^{-5}$	30	0	0	0.21	0.02	$146 + 4.62 * (z - 17.5)$

### Soft Soil model calibration

Based on the soil parameters in table F.1 the parameters for the Soft Soil model are determined, using formulas 3.1 and 3.2. The values following from these formulas are listed in table F.2.

Table F.2: Initial converted Soft Soil model parameters.

Layer	$\gamma$	$e_0$	$\nu$	$k$	$\phi$	$c$	$\psi$	$\lambda^*$	$\kappa^*$	$K_0^{NC}$	$M$
[-]	[kN/m <sup>3</sup> ]	[-]	[-]	[m/day]	[deg]	[kPa]	[deg]	[-]	[-]	[-]	[-]
1	18.5	0.90	0.3	$10^{-5}$	30	0	0	0.065	0.016	0.5	1.65
2	20.5	0.65	0.3	$10^{-5}$	30	0	0	0.056	0.014	0.5	1.65

The initially calculated value for  $\kappa^*$  of clay layer 1 is too high and the value is recalculated using the thumb rule:  $\kappa^* = \lambda^* / 4$ .

The oedometer test results are used to calibrate the stiffness parameters,  $\lambda^*$  and  $\kappa^*$ . The consolidated undrained triaxial test results are used to calibrate the strength parameters,  $\phi$ ,  $c$  and  $\psi$ . The calibrated Soft Soil model parameters are shown in table F.3.

Table F.3: Calibrated Soft Soil model parameters.

Layer	$\gamma$	$e_0$	$\nu$	$k$	$\phi$	$c$	$\psi$	$\lambda^*$	$\kappa^*$	$K_0^{NC}$	$M$
[-]	[kN/m <sup>3</sup> ]	[-]	[-]	[m/day]	[deg]	[kPa]	[deg]	[-]	[-]	[-]	[-]
1	18.5	0.90	0.3	$10^{-5}$	30	5	0	0.055	0.010	0.5	1.65
2	20.5	0.65	0.3	$10^{-5}$	30	1	0	0.056	0.011	0.5	1.65

## Laboratory and PLAXIS test results

The results of the laboratory and PLAXIS test results (oedometer, CU triaxial) are shown presented in this section. In PLAXIS the Soil Test feature is used to simulate the tests. Note that these results follow from the Soft Soil model using the values for the model parameters as listed in table E.3.

### 1. Oedometer test results

Table E.4: Laboratory and Soft Soil model oedometer test results.

	Depth [m]	$p_c$ [kPa]	OCR [-]	$\epsilon_{yy,max}$		Figure
				Lab test [%]	SS model [%]	
Layer 1	4.1	500	14.5	13.1	15.5	F.1b
	5.25	200	6	19.5	18.1	F.1a
	14.35	500	4.2	14	15.5	F.1b
	16.3	500	3.7	14	15.5	F.1b
Layer 2	10.15	1200	5.9	15.8	16.3	F.2a
	20.25	700	4.1	16.7	16.3	F.2b

#### A. Clay layer 1

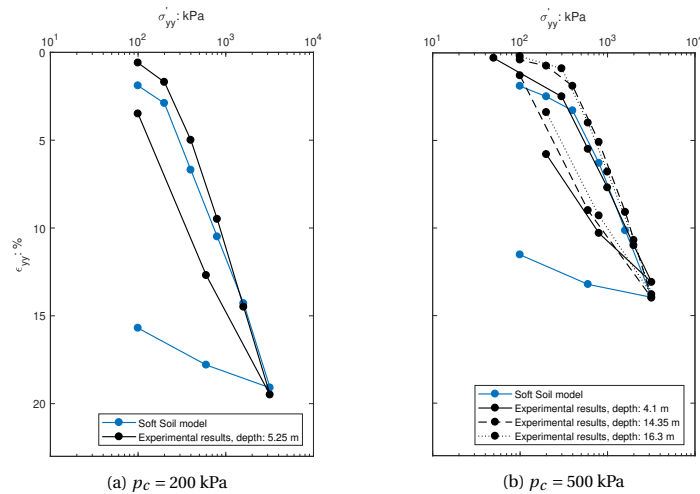


Figure E1: Laboratory and Soft Soil model oedometer results for three different values of the preconsolidation stress for clay layer 1.

#### B. Clay layer 2

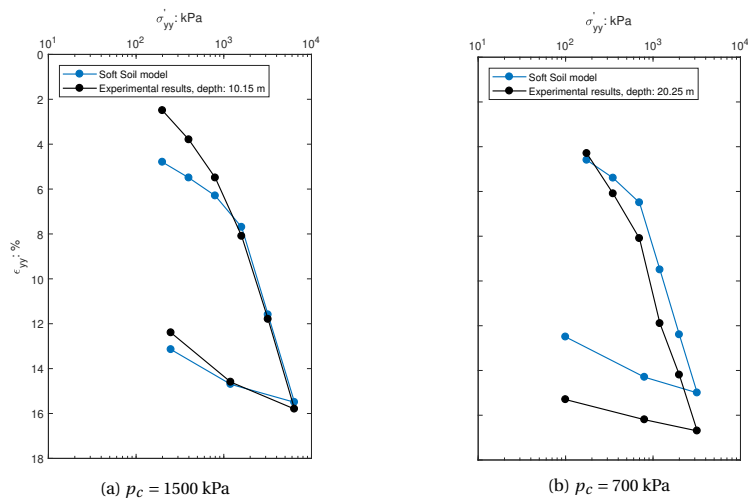


Figure E2: Laboratory and Soft Soil model oedometer results for three different values of the preconsolidation stress for clay layer 2.

## 2. CU triaxial test results

The preconsolidation pressure for each of the triaxial test results is listed in table E5. The preconsolidation pressure is used to simulate the CU triaxial test results in the Soil Test feature in PLAXIS.

Table E5: Characteristics of the CU triaxial tests.

	Depth	$\sigma'_{v,0}, \sigma'_{h,0}$	OCR	$\sigma'_{v,max}$	$K_0$	$\sigma'_{h,max}$	$q_{max}$	$p'_{max}$	$p_c$
	[m]	[kPa]	[-]	[kPa]	[-]	[kPa]	[kPa]	[kPa]	[kPa]
Layer 1	6.24	66	6.0	396	1.23	488	92	457	473
	9.32	90	5.0	450	1.13	510	60	490	496
	11.48	116	5.0	580	1.13	658	78	632	640
	15.21	134	4.5	603	1.08	652	49	635	639
	16.05	151	4.5	678	1.08	734	55	716	720
Layer 2	9.22	106	9.8	1039	1.41	1464	425	1322	1441
	19.5	172	4.0	688	1.09	751	63	730	735

Table E6: Laboratory and Soft Soil model CU triaxial test results.

	Depth	Cel pressure	$s_u$		$p_{excess,max}$		Figure
			Lab test	SS model	Lab test	SS model	
	[m]	[kPa]	[kPa]	[kPa]	[kPa]	[kPa]	
Layer 1	6.24	66	83	43	47	30	E4a
	9.32	90	47	50.6	58	38	E4b
	11.48	116	83	64	71	47	E4c
	15.21	134	64	76	85	53	E4d
	16.05	151	84	84	95	59	E4e
Layer 2	9.22	106	159	59	53	49	E5a
	19.5	172	164	102	70	72	E5b

### A. Clay layer 1

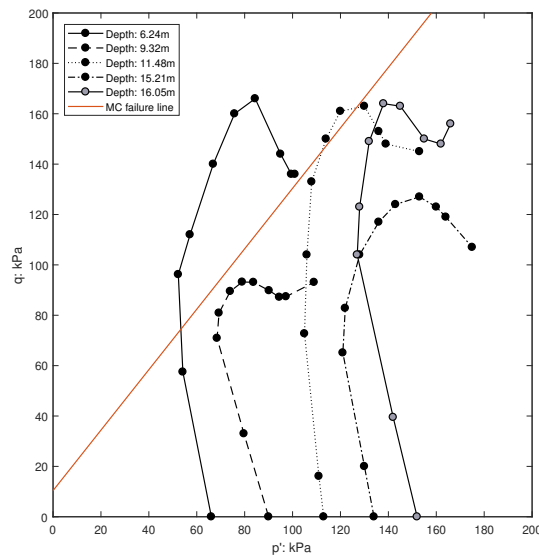


Figure E3:  $q - p'$  stress path for the laboratory CU triaxial test results and the CSL from the Soft Soil model for clay layer 1.

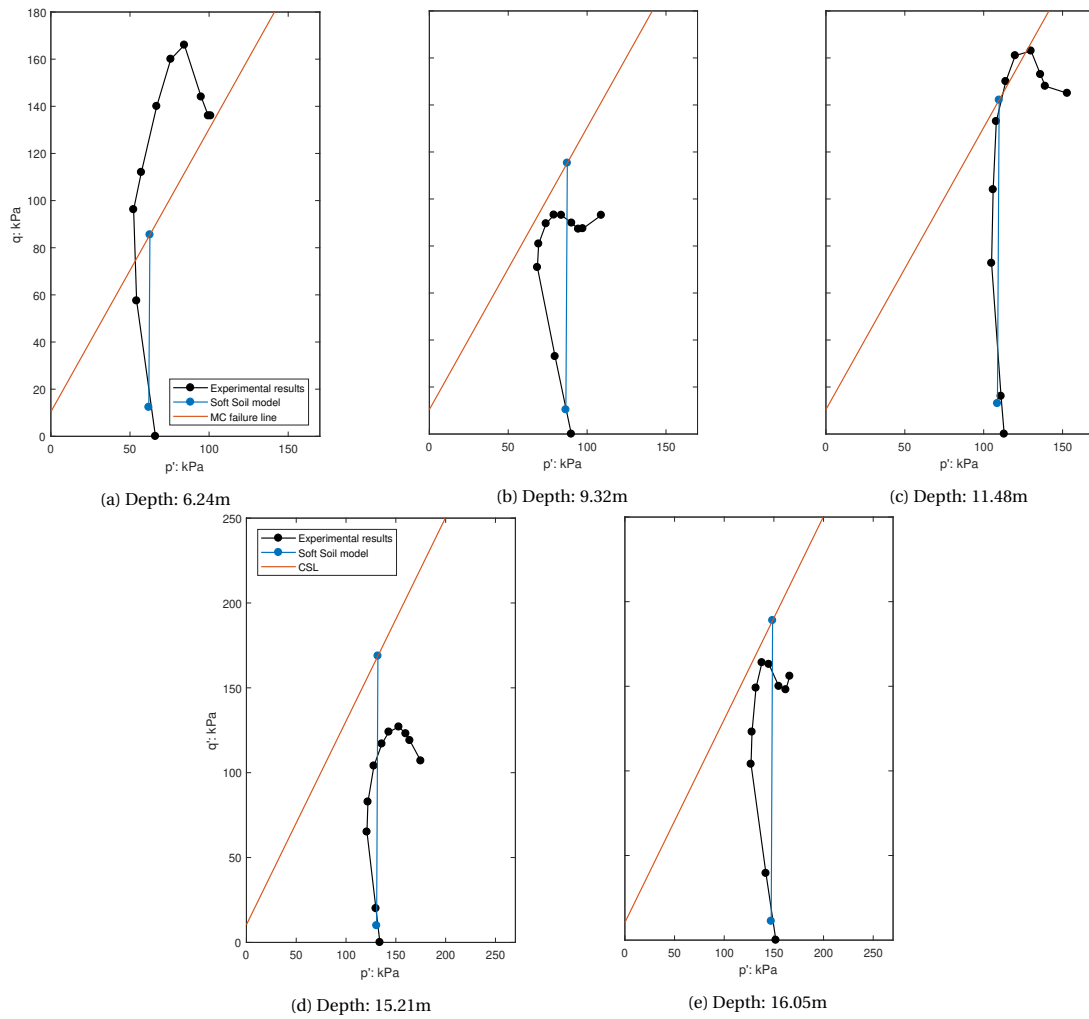


Figure F4:  $q - p'$  stress path for the laboratory and Soft Soil model CU triaxial test for clay layer 1.

## B. Clay layer 2

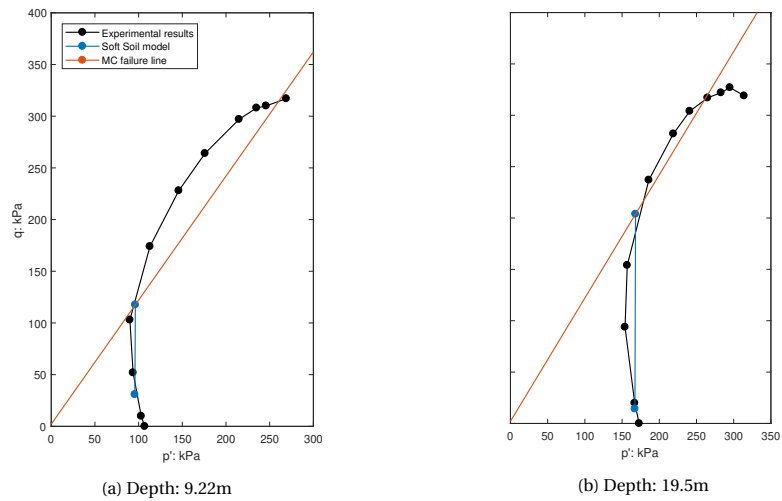


Figure F5:  $q - p'$  stress path for the laboratory and Soft Soil model CU triaxial test for clay layer 2.

## Soft Soil Creep model calibration

The modified creep index,  $\mu^*$ , is the final calibrated parameter. The influence of the modified creep index on the stress path and the undrained shear strength is presented for both clay layers. The influence of the OCR and strain rate are visualized by performing CU triaxial tests in the Soil Test feature in PLAXIS.

### 1. Influence modified creep index

#### A. Clay layer 1

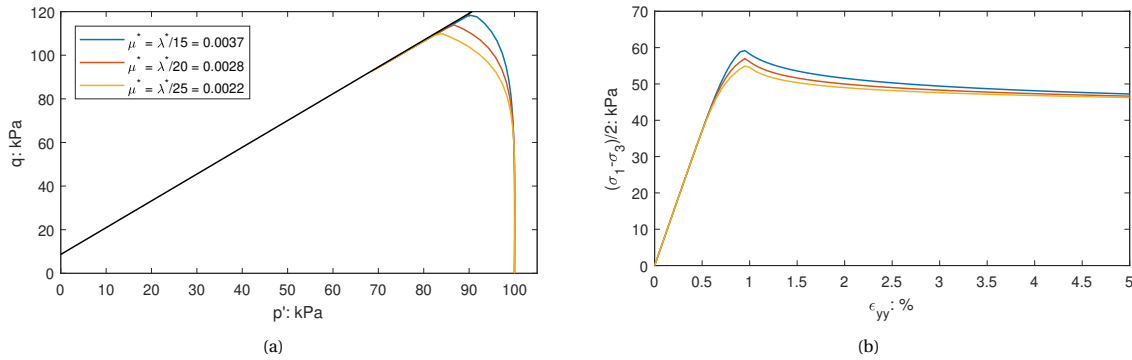


Figure F6: Influence of different values for  $\mu^*$ :  $\frac{\lambda^*}{15}$ ,  $\frac{\lambda^*}{20}$  and  $\frac{\lambda^*}{25}$ . The CU triaxial test conditions are  $\sigma_{cell,init} = 100 \text{ kN/m}^2$ ,  $\epsilon_{yy,max} = 5\%$ ,  $t = 0.1 \text{ day}$  and  $p_c = 0 \text{ kN/m}^2$ .

#### B. Clay layer 2

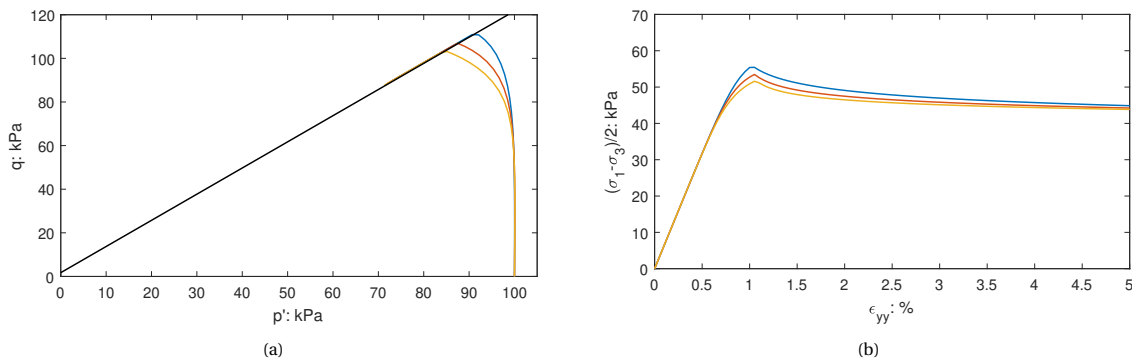


Figure F7: Influence of different values for  $\mu^*$ :  $\frac{\lambda^*}{15}$ ,  $\frac{\lambda^*}{20}$  and  $\frac{\lambda^*}{25}$ . The CU triaxial test conditions are  $\sigma_{cell,init} = 100 \text{ kN/m}^2$ ,  $\epsilon_{yy,max} = 5\%$ ,  $t = 0.1 \text{ day}$  and  $p_c = 0 \text{ kN/m}^2$ .

2. Influence OCR and strain rate

A. Clay layer 1

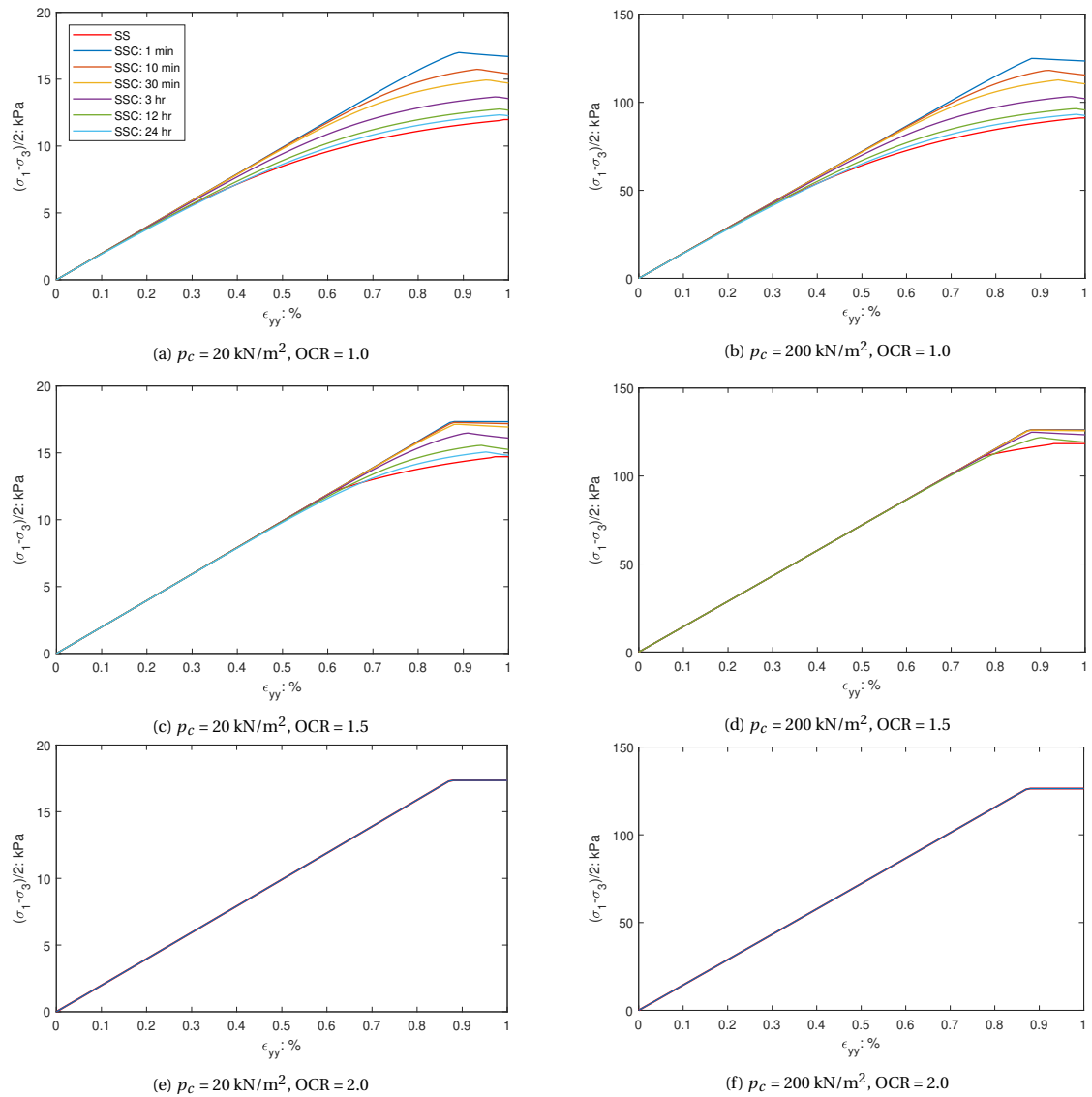


Figure E8: Undrained shear strength for clay layer 1 for different strain rates, OCR and confinement. The value for  $\mu^*$  is set to 0.0028 ( $= \frac{A^*}{20}$ ) and the CU triaxial test conditions are  $\epsilon_{yy,max} = 1\%$ ,  $t = \text{variable}$  and  $p_c = \text{variable}$ .

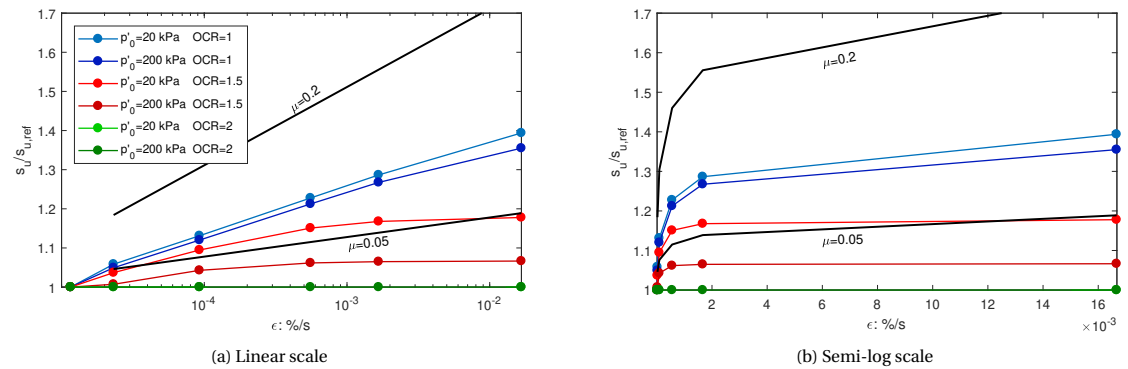
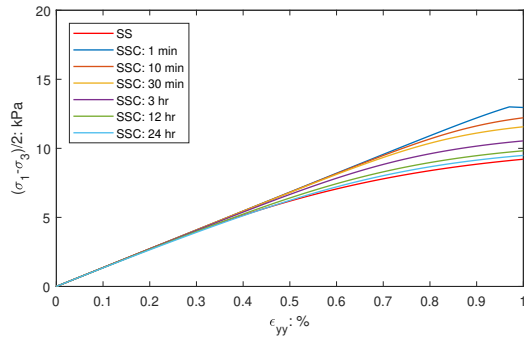
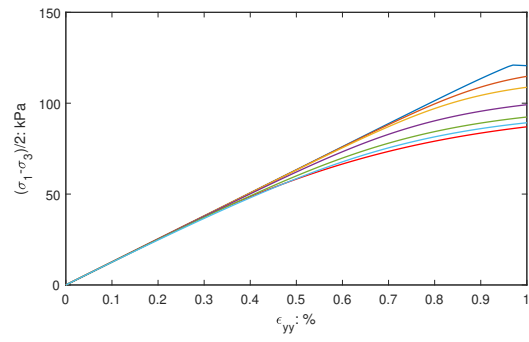


Figure E9: The undrained shear strength profile for clay layer 1 with increasing shear strain rate for different OCR values and initial confinement. The range of the empirical relation, equation 3.9, is added to the figures.

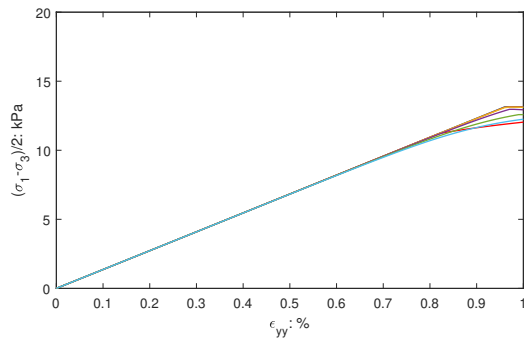
**B. Clay layer 2**



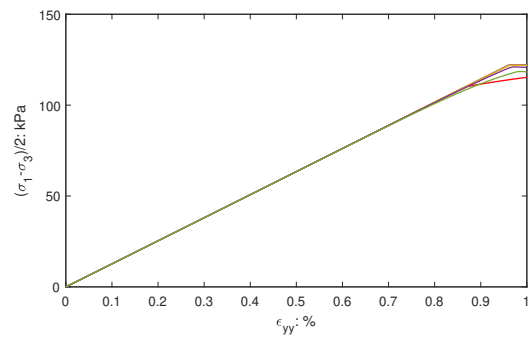
(a)  $p_c = 20 \text{ kN/m}^2$ , OCR = 1.0



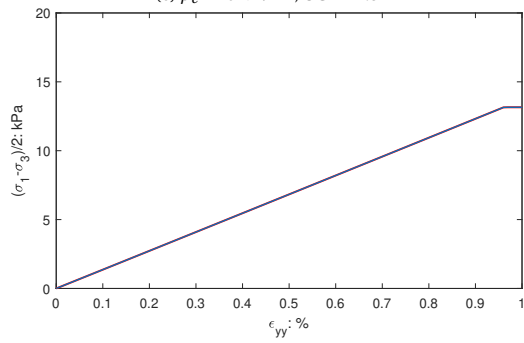
(b)  $p_c = 200 \text{ kN/m}^2$ , OCR = 1.0



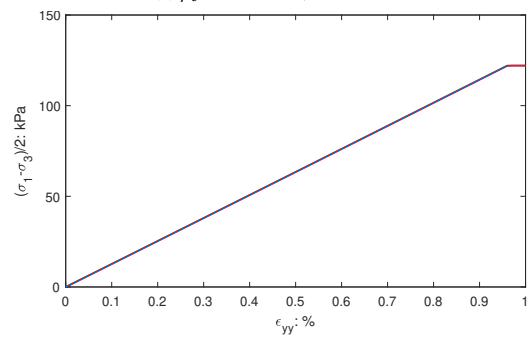
(c)  $p_c = 20 \text{ kN/m}^2$ , OCR = 1.5



(d)  $p_c = 200 \text{ kN/m}^2$ , OCR = 1.5

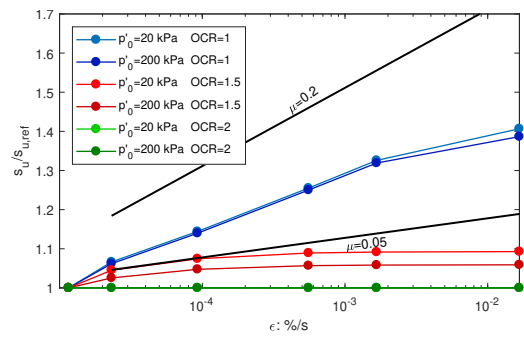


(e)  $p_c = 20 \text{ kN/m}^2$ , OCR = 2.0

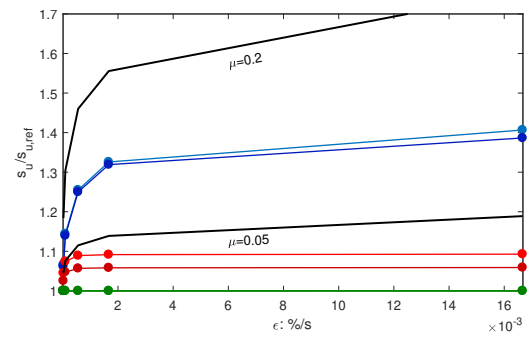


(f)  $p_c = 200 \text{ kN/m}^2$ , OCR = 2.0

Figure F10: Undrained shear strength for clay layer 2 for different strain rates, OCR and confinement. The value for  $\mu^*$  is set to 0.0028 ( $= \frac{\lambda^*}{20}$ ) and the CU triaxial test conditions are  $\epsilon_{yy,max} = 1\%$ ,  $t = \text{variable}$  and  $p_c = \text{variable}$ .



(a) Linear scale



(b) Semi-log scale

Figure F11: The undrained shear strength profile for clay layer 2 with increasing shear strain rate for different OCR values and initial confinement. The range of the empirical relation, equation 3.9, is added to the figures.

## Change of permeability

During consolidation the excess pore pressures dissipate and the effective soil stresses increase, settlements are seen and the soil volume shrinks. The permeability of the soil determines to a large extent the time required to reach a certain degree of consolidation. During consolidation the permeability changes as the soil settles and the permeability decreases. The change in permeability is accounted for by the parameter  $c_k$  in the SSC model, formulated as:

$$\log\left(\frac{k}{k_0}\right) = \frac{\Delta e}{c_k} \quad (\text{G.1})$$

$\Delta e$  is the change in void ratio,  $k$  is the permeability and  $k_0$  is the input value of the permeability. According to Brinkgreve et al. (2018a) the value of  $c_k$  is generally in the order of the compression index,  $C_c$ . The results for a consolidation calculation adopting different values for  $c_k$  are depicted in figure G.1. The effect of variation in the value for  $c_k$  on the settlements during consolidation is negligible. A small difference is seen only after 6 days and longer. The graph corresponding the model accounting for a changing permeability shows lower settlements after 6 days and longer. The effect of a change in permeability during consolidation is not taken into account as the jack-up vessel, considering the offshore wind industry, is operational for a maximum of 1 day at one location.

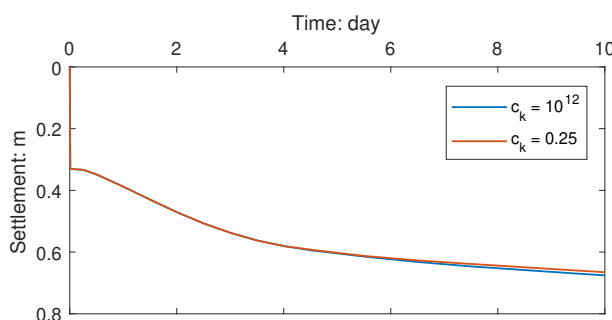


Figure G.1: Visualization of the effect of the change in permeability during consolidation.

## Alternative FE model

In an attempt to decrease the calculation time of the FE simulation of the preload procedure, each spudcan penetrating into the soil is replaced by fixed-end anchors. The fixed-end anchors serve as springs and a certain stiffness is assigned to each anchor to simulate the spudcan penetration during the different phases in the preload procedure. The spudcan penetration is simulated in PLAXIS 2D, compared to 3D these simulations allow for a sufficient decrease in computation costs (in terms of time and memory usage). This alternative method can only be executed under the condition that the spudcans do not interfere with each other.

As the fixed-end anchor is limited to a single, constant, stiffness the stiffness value is updated accordingly for each calculation phase. The stress dependent stiffness of the fixed-end anchor is determined by performing spudcan penetrations in 2D. As only one stiffness values can be assigned to a fixed-end anchor per calculation phase, the stress dependent stiffness is approached by a linear graph.

The alternative FE model does not allow for accurate consolidation calculations. The extent of the influence of consolidation during spudcan penetration is determined for a constant load for the alternative method. During the consolidation the spudcans proceed to penetrate at a different rate, the leg loads develop accordingly. Via the structure connecting the legs the loads are constantly redistributed, this is an essential mechanism influencing the consolidation phase and is not captured by the alternative FE model.

Figure H.2 depicts a schematisation of the alternative model, table H.1 lists the stress dependent stiffness for normalized spudcan penetration at 1.1 and 1.2 respectively.

Table H.1: Stiffness values for the fixed-end anchor for a normalized initial spudcan depth of 1.1 and 1.2.

Normalized spudcan depth	Normalized stiffness					
	0 - 0.6	0 - 0.7	0 - 0.8	0 - 0.9	0 - 0.1	Unloading
1.1	$10.0 \cdot 10^3$	$5.6 \cdot 10^3$	$3.5 \cdot 10^3$	$2.3 \cdot 10^3$	-	$7.15 \cdot 10^3$
1.2	$12.8 \cdot 10^3$	$8.4 \cdot 10^3$	$5.3 \cdot 10^3$	$3.3 \cdot 10^3$	$2.2 \cdot 10^3$	$7.8 \cdot 10^3$

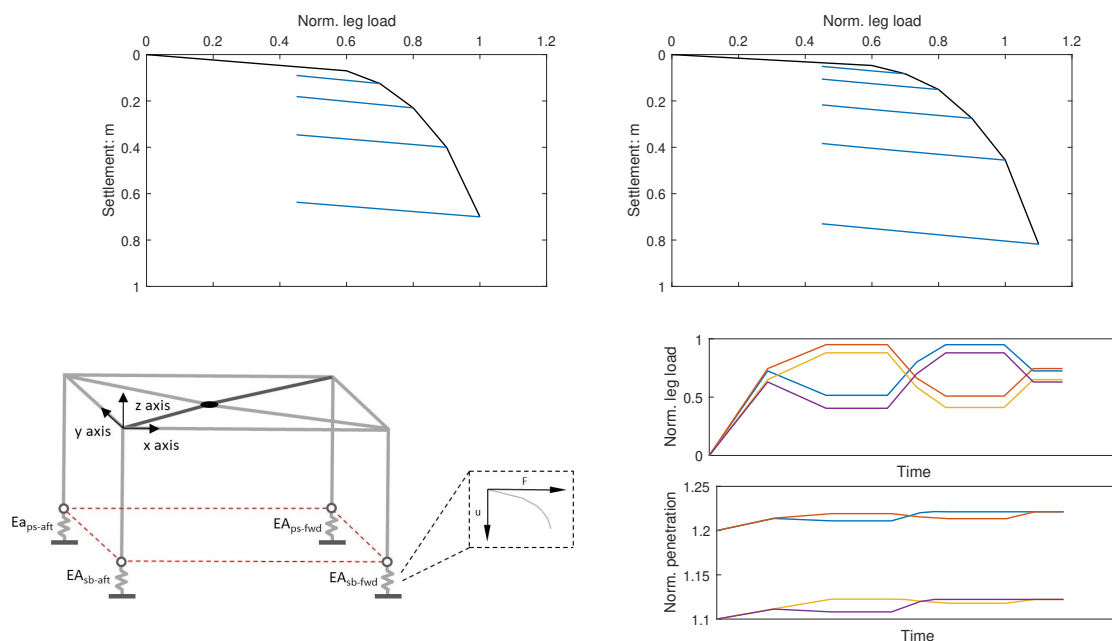


Figure H.2: Leg loads and spudcan penetrations for the preload procedure simulation conducted with the alternative FE model.

|

## Jacking data - Confidential

### J.1 Case results

The results for each case of the two type of simulations, the single spudcan penetration and the complete preload procedure, are presented in this section.

#### J.1.1 Single spudcan penetration

Figures J.1a - J.1b depict the spudcan penetration as a function of the leg load and time for the six cases of the simulation of the single spudcan penetration.

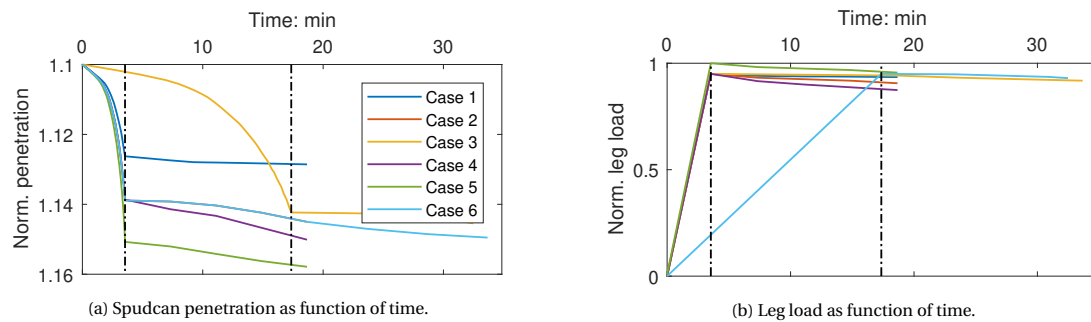


Figure J.1: Single spudcan penetration simulation results.

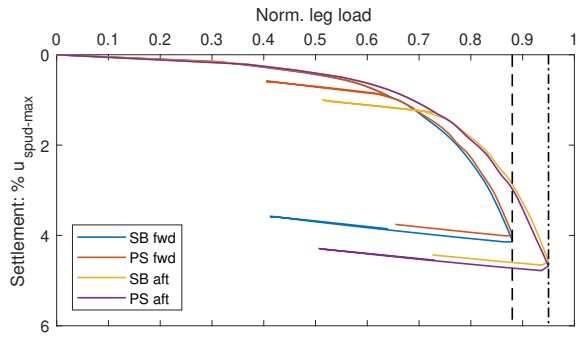
#### J.1.2 Preload procedure

This section presents the FE results of the preload procedure with the complete 3D FE model. The displacement of the ship corners and the extension of the node-to-node anchors the spudcan settlement as function of leg load are presented.

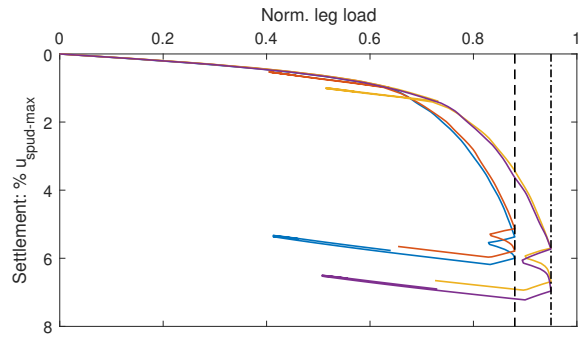
**Ship displacement and leg extension - Confidential**

**Spudcan settlement - leg load**

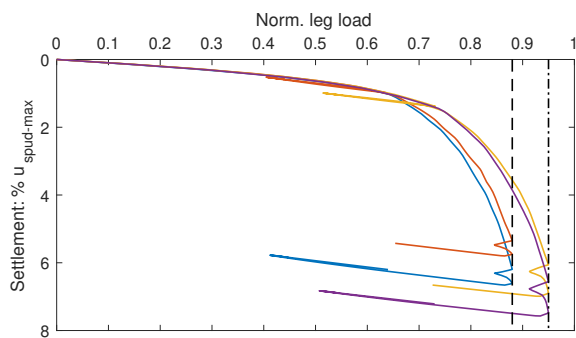
Figures J.2a - J.2e depict the spudcan settlement as a function of the leg load for the five cases of the simulation of the preload procedure.



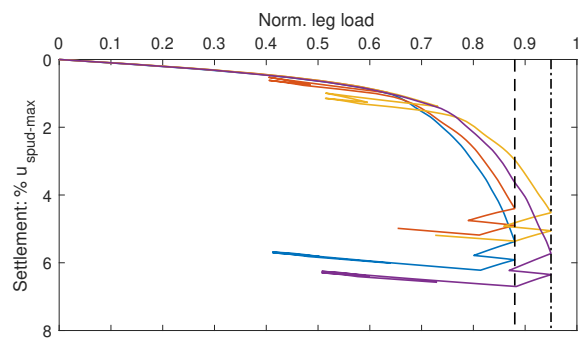
(a) Leg load as function of spudcan settlement for case 1.



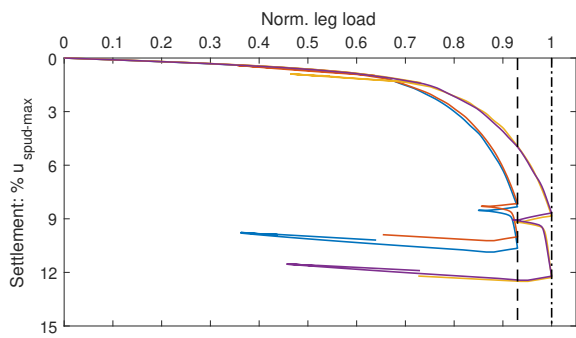
(b) Leg load as function of spudcan settlement for case 2.



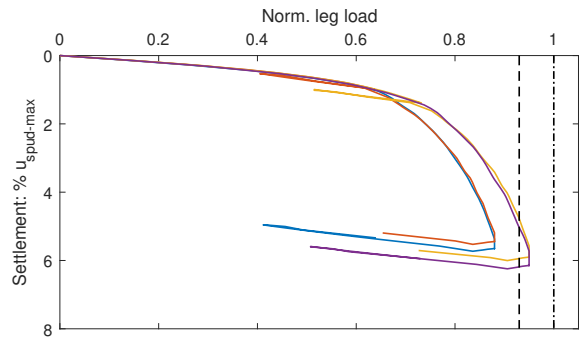
(c) Leg load as function of spudcan settlement for case 3.



(d) Leg load as function of spudcan settlement for case 4.



(e) Leg load as function of spudcan settlement for case 5.



(f) Leg load as function of spudcan settlement for case 6.

Figure J.2: Preload procedure simulation results.

## J.2 Vessel structure

The deformed vessel structure during the different stages of the preloading procedure is presented in the figures J.3a - J.3e. The red lines indicate the initial position of the beam configuration. The distance between the red lines and the beams of the structure indicates the relative displacement and deformation. The black beams at the bottom of each leg indicate the node-to-node anchors, which extend during the different calculation phases. During extension of the mechanism the spudcans are pushed into the soil.

The weight of the complete structure is considered as a point load and applied at the intersection point of the diagonal beams, which is positioned slightly aft of the middle of the structure.

Figure J.3e indicates the ship is slightly tilted aft at the end of the preloading procedure. This is a consequence of the choice for the initial spudcan depth.

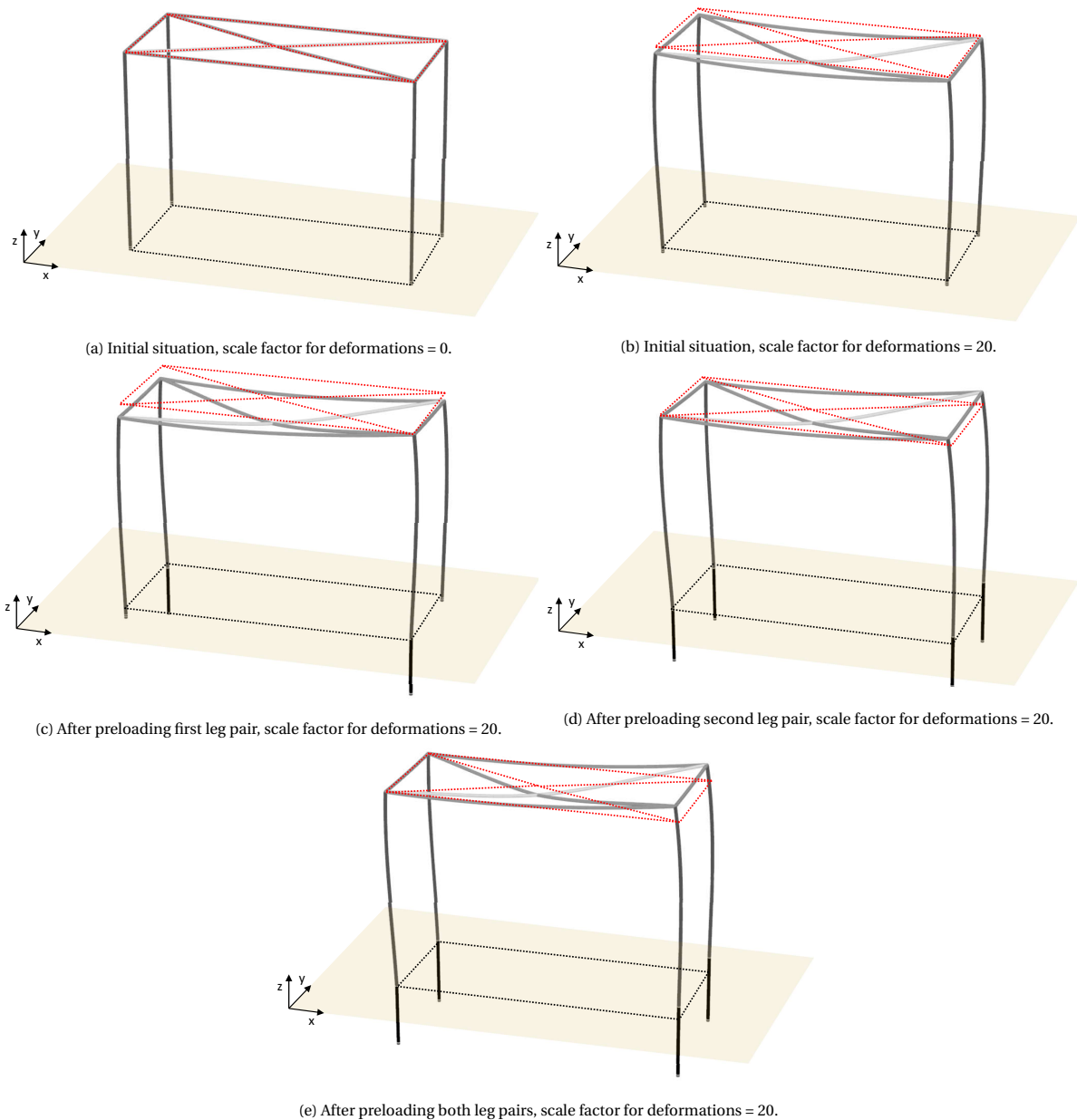


Figure J.3: Deformed vessel structure during different stages of the preloading procedure.

### J.3 Comparison jacking data

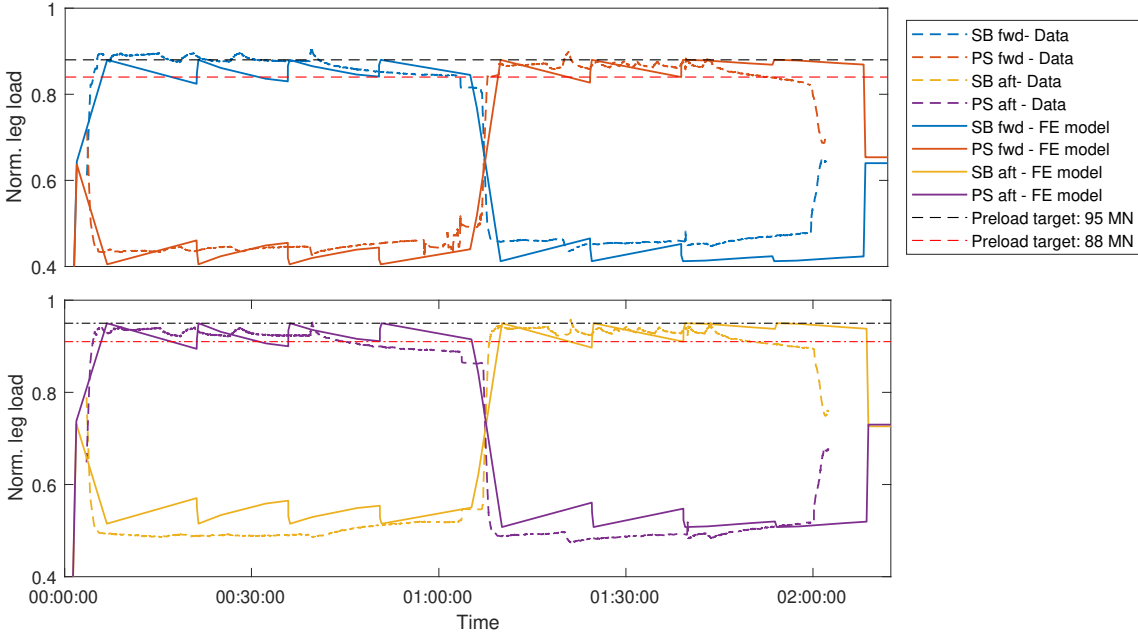


Figure J.4: Leg load as function of time, jacking data and FE model results plotted in one graph.

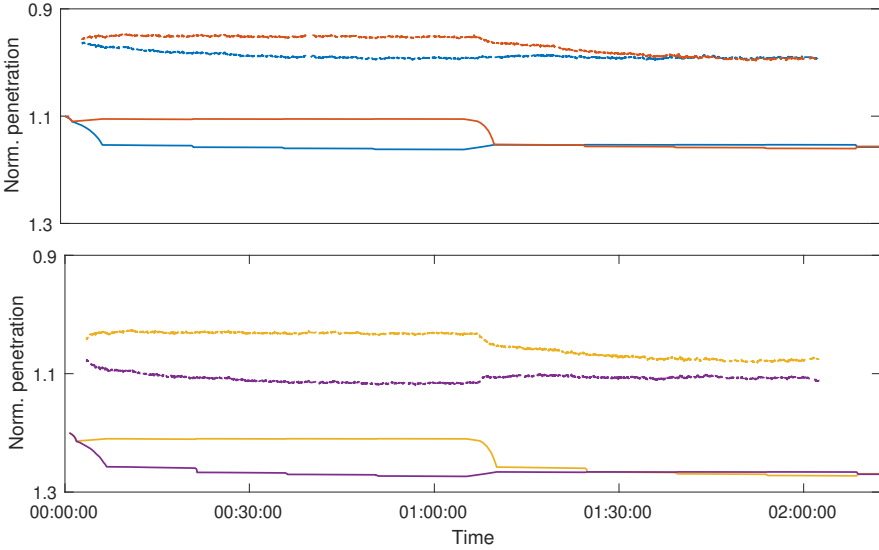


Figure J.5: Spudcan penetration as function of time, jacking data and FE model results plotted in one graph.

K

## Normalization rules - Confidential